Jül-4387

Institute of Neuroscience and Medicine
Nuclear chemistry (INM-5)

Investigations on the production of ^{52g}Mn and ^{147,149}Gd for authentic labelling of MR contrast agents

Martin Buchholz

JÜLICH
FORSCHUNGSZENTRUM

Investigations on the production of ^{52g}Mn and ^{147,149}Gd for authentic labelling of MR contrast agents

Martin Buchholz

Berichte des Forschungszentrums Jülich; 4387
ISSN 0944-2952
Institute of Neuroscience and Medicine
Nuclear chemistry (INM-5)
Jül-4387

D 38 (Diss., Köln, Univ., 2015)

Vollständig frei verfügbar über das Publikationsportal des Forschungszentrums Jülich (JuSER)
unter www.fz-juelich.de/zb/openaccess

Forschungszentrum Jülich GmbH
Zentralbibliothek, Verlag
52425 Jülich
Tel.: +49 2461 61-5220
Fax: +49 2461 61-6103
E-Mail: zb-publikation@fz-juelich.de
www.fz-juelich.de/zb

Die vorliegende Arbeit wurde in der Zeit von Januar 2012 bis Februar 2015 am Institut für Neurowissenschaften und Medizin, INM-5: Nuklearchemie, des Forschungszentrum Jülich, unter der Anleitung von Herrn Prof. Dr. H. H. Coenen durchgeführt.

Abstract

Addressing the quantitation problem of contrast enhancing MRI compounds based on gadolinium (III) and manganese (II), the production of suitable radionuclides as well as activation and the authentic radiolabelling of MR contrast agents were examined.

The existing cross section data of the $^{nat}Eu(d,x)^{147,149}Gd$ and $^{nat}Eu(p,x)^{147,149}Gd$ reactions were expanded up to 70.9 MeV and 44.8 MeV, respectively. The integral production rates of the $^{nat}Eu(d,x)^{147}Gd$ and $^{nat}Eu(p,x)^{147}Gd$ reactions were 177.3 ± 19.7 and 43.3 ± 4.4 MBq/μAh while the integral production rates of the $^{nat}Eu(d,x)^{149}Gd$ and $^{nat}Eu(p,x)^{149}Gd$ reactions amounted to 81.6 ± 8.5 and 61.8 ± 4.9 MBq/μAh, respectively. The formation of longer-lived radioisotopic impurities ($^{146,151,153}Gd$) was below 7 %, but the use of enriched Eu target material was found to be necessary for a radionuclidically pure production of either ^{147}Gd or ^{149}Gd. Since the production rates are higher than for the earlier proposed irradiation of highly enriched $^{144,147}Sm$ with α- or ^{3}He-particles, Eu is an interesting alternative for the production of $^{147,149}Gd$.

In addition to the measurement of nuclear data, a new radiochemical separation of the bulk target material Eu and n.c.a. $^{*}Gd$ based on an extraction of Eu into Na-Hg amalgam was successfully developed. In a proof of principle synthesis, the obtained $^{*}Gd$ was complexed with the ligand DOTA and an adequate stability of the complex confirmed over 6 d in Human Blood Serum (HBS). In a comparison by *in* and *ex vivo* MR and autoradiographic measurements of the commercial Gd-DOTA complex, DOTArem™, and the synthesised radioactive complex on tumour bearing rats a rather similar accumulation in the tumour tissue and surrounding striatum was found.

Furthermore, production yields of the proton induced nuclear reactions on ^{nat}Cr leading to ^{52g}Mn, ^{52m}Mn and ^{51}Cr were measured in the energy range from 8.2 to 16.9 MeV and saturation thick target yields calculated as 2.6 ± 0.3, 7.0 ± 0.6 and 1.5 ± 0.2 GBq/μA, respectively. A new chromatographic separation method was developed which yielded 99.5 % of pure ^{52g}Mn in 2 mL of 3M hydrochloric acid solution. Thereby, n.c.a. ^{52g}Mn can be provided more efficiently for the isotopic labelling of MR contrast agents. The radioactive nanoparticle precursor $Mn(acac)_2$ was synthesised with a radiochemical yield of 73.9 ± 5.0 %.

Additionally, activation studies with protons and neutrons were performed with commercially available water-dispersible Mn_3O_4 nanoparticles. The activated nanoparticles were characterised with DLS and TEM. No change between the initial and irradiated nanoparticles was found with neutron activation. A broader size distribution and the scattered appearance of bigger crystals were observed in the proton irradiated samples caused by partial melting and recrystallization of the samples during irradiation. Leaching experiments of the neutron activated particles in H_2O and PBS resulted in 0.033 ± 0.005 % of released Mn after a 15h incubation time indicating a high stability of the compound.

Kurzzusammenfassung

Zur Quantifizierung von Kontrastmitteln mittels PET oder SPECT wurden die Produktion sowie die nuklearchemischen Eigenschaften von Radionukliden für eine authentische Markierung von Gadolinium (III) und Mangan (II) basierten MRT-Kontrastmitteln untersucht.

Dazu wurden Wirkungsquerschnitte der $^{nat}Eu(d,x)^{147,149}Gd$ und $^{nat}Eu(p,x)^{147,149}Gd$ Kernreaktionen mit Projektilenergien bis zu 70,9 MeV bzw. 44,8 MeV gemessen. Die integralen Ausbeuten der $^{nat}Eu(d,x)^{147}Gd$ und $^{nat}Eu(p,x)^{147}Gd$ Kernreaktionen über den gemessenen Energiebereich wurden entsprechend zu 177,3 ± 19,7 MBq/μAh und 43,3 ± 4,4 MBq/μAh bestimmt. Für die Reaktionen $^{nat}Eu(d,x)^{149}Gd$ und $^{nat}Eu(p,x)^{149}Gd$ konnten integrale Ausbeuten von 81,6 ± 8,5 MBq/μAh bzw. 61,8 ± 4,9 MBq/μAh berechnet werden. Die Bildung der langlebigen Verunreinigungen $^{146,151,153}Gd$ lag dabei bei ca. 7 %, was die Nutzung von angereichertem Eu für eine radionuklidreine Herstellung von ^{147}Gd oder ^{149}Gd notwendig macht. Die deutlich höheren Ausbeuten im Vergleich zur Nutzung von $^{144,147}Sm$ als Targetmaterial sprechen dennoch für die Verwendung von Eu.

Ferner wurde eine Trennung von Eu und n.c.a. $^{*}Gd$ entwickelt, die auf der Extraktion des Targetmaterials Eu in ein Na-Hg Amalgam beruhte. Das so isolierte $^{*}Gd$ wurde mit dem Liganden DOTA komplexiert und die Stabilität in Humanserum (HBS) über 6 d nachgewiesen. Beim Vergleich des radioaktiven und kommerziellen Gd-DOTA-Komplexes bei *in* und *ex vivo* Messungen von tumortragenden Ratten mittels MRT bzw. Autoradiographie wurde eine Anreicherung im Tumorgewebe und dem umgebenden Striatum gefunden.

Zur Herstellung von ^{52g}Mn, ^{52m}Mn und dem Nebenprodukt ^{51}Cr wurden die Produktionsausbeuten der entsprechenden $^{nat}Cr(p,xn)$-Kernreaktionen in einem Energiebereich von 8,2 bis 16,9 MeV gemessen und die Ausbeuten im Sättigungsbereich zu jeweils 2,6 ± 0,3, 7,0 ± 0,6 und 1,53 ± 0,15 GBq/μA berechnet. Es wurde eine neue chromatographische Trennung von Cr und Mn entwickelt, welche zu einer Elution von 99,5 % ^{52g}Mn in 2,1 mL 3M HCl führte. Damit ist ^{52g}Mn nun für die Markierung von Magnetoradiopharmaka wesentlich einfacher verfügbar. Bei der Synthese des Nanopartikel-Vorläufers $Mn(acac)_2$ mit dem so isolierten ^{52g}Mn konnte eine radiochemische Ausbeute von 73,9 ± 5,0 % erreicht werden.

Weiterhin wurden kommerzielle Mn_3O_4 Nanopartikel mit Neutronen und Protonen aktiviert und mit DLS und TEM charakterisiert. Bei der Aktivierung mit Neutronen wurden keinerlei Änderungen beobachtet, während bei Protonen-aktivierten Nanopartikeln eine breitere Größenverteilung und vereinzelte größere Kristalle beobachtet wurden. Dies konnte durch teilweises Schmelzen und eine anschließende Rekristallisation während der Bestrahlung erklärt werden. Die Neutronenaktivierungsstudie an kommerziellen Mn_3O_4-Nanopartikeln ermöglichte zudem die Ermittlung des freien Mangans nach Inkubation in H_2O und PBS. Nach einer Inkubationszeit von 15 h wurden nur 0.033 ± 0.005 % des insgesamt eingesetzten Mn Inventars in Lösung vorgefunden, was eine hohe Stabilität in Lösung anzeigt.

Contents

List of figures

List of tables

Abbreviations

AES: Auger Electron Spectroscopy

ARG: Autoradiography

c.a.: carrier added

CE: Contrast Enhancement

CT: Computed Tomography

CY: Chemical Yield

DLS: Dynamic Light Scattering

ESI-MS: Electrospray-Ionisation Mass Spectrometry

EOB: End of Bombardment

EXC: Extraction Chromatography

FDA: Food and Drug Administration of the United States of America

FID: Free Inductive Decay

HBS: Human Blood Serum

HPLC: High Pressure / High Performance Liquid Chromatography

IEC: Ion Exchange Chromatography

JULIC: Juelich Isochronous Cyclotron

LLX: Liquid-Liquid-Extraction

MEMRI: Manganese Enhanced Magnetic Resonance Imaging

MRI: Magnetic Resonance Imaging

n.c.a.: no carrier added

NMR: Nuclear Magnetic Resonance

PBS: Phosphate Buffered Saline

PET: Positron Emission Tomography

PTB: Physikalisch-Technische Bundesanstalt

PVP: Polyvinylpyrrolidone

RCY: Radio Chemical Yield

SAED: Selected Area Electron Diffraction

SEM: Scanning Electron Microscope

SF: Separation Factor

SIMS: Secondary Ion Mass Spectroscopy

SPECT: Single Photon Emission Computed Tomography

TENDL: TALYS-based evaluated nuclear data library

TEM: Transmission Electron Microscope

TC: Thermochromatography

TRIGA: Training, Research, Isotopes, General Atomic

XRD: X-Ray Diffraction

XPS: X-ray Photoemission Spectroscopy

1. Introduction

1.1 Radioactivity and its use in life science

Radioactivity is defined as a property of unstable isotopes to undergo a stochastic and spontaneous nuclear transformation towards a more stable isotope under the emission of ionizing radiation such as α-particles, β-particles, γ-rays or Auger-electrons.[1] Unstable nuclei, also called radionuclides, can be classified as proton or neutron deficient, depending on an excess of neutrons or protons present in the nucleus.

Since the discovery of this radioactivity in 1896 by Henri Becquerel and the isolation of radium in 1898 by Marie Curie, many applications for radioactive isotopes were developed in a multitude of areas. Radionuclides are applied in five fields of life sciences: ecology, physiology and metabolism, diagnosis, therapy, and elemental analysis.[2] Besides the study of the interactions among organisms ecology comprises also the investigation of the environmental uptake of abiotic compounds such as trace elements or radionuclides by plants, animals and humans. In physiological and metabolic studies, the reactions and biochemical processes of elements and compounds in the living world are assessed. The identification and localisation of diseases with imaging methods is the content of diagnosis, while therapy is the treatment of the diseases found. Elemental analysis comprises the assessment of compounds and trace elements in the living world.

High amounts of radioactivity are needed for any therapeutic application, while for the analysis of chemical elements activation, mainly by neutrons, is of high importance. The radiotracer method, on the other hand, finds application in all fields of life sciences. The principle of this radiotracer method was defined, applied and thus founded by George de Hevesy and Friedrich Adolf Paneth as early as 1923[3]. These radiotracers are chemical compounds in which one or more atoms are replaced with a radioactive isotope. This enables the exploration of mechanisms by tracing the way of the radioisotope. The advantage over non-radioactive methods is the high measurement sensitivity enabling the determination of concentrations in the range of 10^{-12} mol. Therefore, the investigated system is not influenced by mass action of an excess of analytic material.

At first, only few radioisotopes were available, mainly produced by the isolation from the primordial decay chains such as ^{212}Pb which was used by de Hevesy and Paneth[3] in their research of lead uptake and distribution in plants. Since the development of the cyclotron in 1930 by Ernest O. Lawrence[4], radiochemistry entered a new era with a wide spectrum of new accessible radionuclides. In addition to the production facilities, the detection capabilities of radioactivity also evolved. Starting with simple photo plates and films, going to scintillation

or semiconductor detectors, today's tomographic methods like single photon emission computed tomography (SPECT) or positron emission tomography (PET) were developed.
Both methods utilise the radioactive decay of specific radionuclides for non-invasive imaging of their distribution within a body. In combination with radiotracers, which are selective for a specific biological process, they are the foundation of modern nuclear medicine. However, PET as well as SPECT depicts the distribution of radioactive tracers in the body with no information about their chemical form and only limited morphologic information. While the more pronounced problem of the chemical form has to be solved by complex bio-mathematical models and additional metabolism studies, the use of complimentary imaging methods like computed tomography (CT) or magnetic resonance imaging (MRI) can often be needed or advantageous to address the limited morphological information of PET and SPECT.
In this study, the production parameters and separation procedures of radioactive isotopes of gadolinium and manganese were investigated. Both elements are most promising for the development of bi-modal probe concepts based on the isotopic labelling of MRI contrast agents.

1.2 Magnetic resonance imaging (MRI)

MRI is a non-invasive medical imaging method which yields a high morphologic resolution without exposing the patient to potentially harmful ionising radiation.[5] Like nuclear magnetic resonance spectroscopy (NMR-spectroscopy), it is based on the observation of nuclear core spins in a magnetic field.[5-10] One of the first experiments was already conducted in 1973 showing the applicability of magnetic resonance for *in vivo* imaging.[11]
Starting from one and two dimensional NMR spectroscopy *in vivo,* three-dimensional imaging rapidly evolved in the last 40 years to a diagnostic standard tool in clinical routine and research to solve biochemical as well as medical questions.[7] Additionally, no damage to DNA or other functional cell components in patients by the magnetic field or the excitation radiofrequency pulses was noticed until now as long as the basic safety regulations were observed.[12-15] This is one of the big advantages over other *in vivo* imaging methods like computed tomography (CT) which needs intense use of X-rays and therefore induces high radiation dose rates. But the measurement times of MRI are longer[10], and the availability of clinical scanners is still lower than for CT. Beside the pure morphological MR imaging the possibility to measure body functions such as blood flow, tissue perfusion[16] etc. was developed in the last two decades using functional MRI (fMRI).[17] Some fMRI methods are only possible with suitable contrast agents[5] which lead to a positive or negative enhancement of the imaging contrast what will be explained in detail below.

The combination of multiple imaging methods to acquire complementary data in a shorter time period would be the next logical development step to broaden the utility of imaging techniques even further and enhance the diagnostic efficiency. Therefore, the basic principles of each imaging technique have to be understood.

1.2.1 Principle

The basic principle of both NMR and MRI is the property of random arranged nuclear spins of nuclear cores to align themselves parallel or anti parallel to the direction of an applied magnetic field.[5] The coupling between the magnetic field and the spins thereby induced, known as Zeeman interaction[18], results in an energy gap with the parallel aligned spins being lower in energy than anti parallel aligned spins. The energy gap between both states is directly correlated to the strength of the magnetic field as expressed by the Larmor equation 1[5]:

$$\omega_0 = \frac{B_0 \gamma}{2\pi}$$

with ω_0: Larmor frequency in MHz,

B_0: magnetic field strength in Tesla (T),

γ: gyromagnetic ratio in $s^{-1}\ T^{-1}$.

According to the Boltzmann equation[19], more spins are distributed in the lower than the higher energy level and therefore aligned parallel to the magnetic field. This leads to a net magnetization, M_0, of the material, also parallel to the magnetic field direction. If an alternating magnetic field, B_1, is applied perpendicularly to the static magnetic field B_0, the spins can switch their alignment and hence, the net magnetisation changes. However, only at the alternation frequency, known as resonance frequency, with the specific energy of the energy gap between both states, a transition between the two states is possible. The energy difference is proportional to the frequency ω_0 as described by equation 2[5]:

$$\Delta E = \frac{h\omega_0}{2\pi}$$

with h: Plank's constant, $6.626 \cdot 10^{-34}$ J s.

Applying the definition of ω_0 from equation 1 leads to:

$$\Delta E = \frac{h\gamma B_0}{4\pi^2}$$

Once the radiofrequency pulse (RF) is stopped, the spins turn back to their equilibrium state, this mechanism being known as relaxation. This relaxation has to be stimulated because the small energy difference of the excited and steady state allows no spontaneous relaxation. The rate of relaxation depends therefore on the strength of the spin-lattice interaction (longitudinal relaxation, T_1) and spin-spin interaction (transversal relaxation, T_2). The previously absorbed energy is re-emitted in this process with the frequency ω_0 and measured as a voltage using a detector coil. The recorded signal is better known as free induction decay (FID). The resulting amplitude of the emitted frequency ω_0 is correlated with the density of excited spins or nuclear cores present. Therefore, the number of spins and thus the amount of targeted atoms (e.g. ^{1}H, ^{23}Na, ^{31}P) can be measured in a sample non-invasively and non-destructively.

In addition to the information about the amount of atoms present, the knowledge of their spatial distribution is necessary for the generation of two- or three-dimensional images in MRI. Therefore, alternating magnetic fields are additionally applied in between the RF irradiation with the Larmor frequency[5] to generate a gradient in the static magnetic field. The Larmor frequency needed for excitation of spins is now slightly different throughout the measured sample due to the magnetic gradient. In depth explanation of the exact frequency pulse sequences needed for the spatial encoding, e. g. Single Spin Echo, Inversion Recovery or Spoiled Gradient Echo, and reconstruction of images is not within the scope of this work but can be found in the literature.[5] Briefly, defined small volumes (voxels) are obtained with these methods by the encoding of the three spatial dimensions. The voxels can be selectively excited and measured to be reconstructed into an image of the scanned spatial distribution of the spin density of a targeted atom. The targeted atom nuclei in MRI are usually the ^{1}H protons. The density of protons in different tissues is quit unique leading to the high spatial resolution of MRI in the tens of micrometre range.[20]

1.2.2 Contrast enhancement

Although the morphological contrast originating from the ^{1}H protons in MRI is often sufficient for diagnosis, in some cases more differentiation or contrast between different tissue types or areas is required. An increased contrast can be achieved by the injection of a contrast agent which alters the signal intensity of the ^{1}H protons in its vicinity. Contrast enhancement induced by an injected agent may be explained based upon the Bloch equation 4[21], which describes the nuclear magnetization for a two-energy-level system:

$$\frac{d\,\vec{M}}{dt} = \gamma \vec{M} \cdot \vec{H}_a - \vec{e}_x \frac{M_x}{T_2^*} - \vec{e}_y \frac{M_y}{T_2^*} - \vec{e}_z \frac{M_z - M_0}{T_1}$$

with $\vec{M}$: magnetisation of material,

$\vec{H}_a$: magnetic field,

$\vec{e}_{x/y/z}$: unit vector in x, y and z direction,

$M_{x/y/z}$: partial magnetization in x, y and z direction,

T_2^*: maximum transversal relaxation time,

T_1: longitudinal relaxation time.

T_1 (also called spin-lattice relaxation time) and T_2 (also called spin-spin relaxation time) are time constants that describe the relaxation of the excited nucleus, i.e. how the macroscopic magnetization returns to its equilibrium state. The displayed T_2^* in eq. 4 is a broader constant which includes static magnetic field effects in addition to T_2. When the above differential is derived under the conditions of a standard MRI sequence like Spin Echo, the corresponding signal intensity (I_{SE}) is given by equation 5[5]:

$$I_{SE} = N_H \cdot K' \cdot e^{-\frac{T_E}{T_2}} \cdot 1 - 2e^{-\frac{\left(T_R - \frac{T_E}{2}\right)}{T_1}} + e^{-\frac{T_R}{T_1}}$$

with N_H: number of hydrogen atoms per volume unit,

K': constant depending on extrinsic parameters,

T_E: echo time between excitation pulse and echo maximum in ms,

T_R: repetition time between successive RF excitation pulses in ms.

While N_H and K' are constants, T_E and T_R are experimental parameters that can be modified by the operator. As shown by equation 4, the signal intensity can be modulated by shortening the longitudinal and/or transversal relaxation times: This is precisely how a MR contrast agent acts. Depending on the relaxation time that is reduced to a greater extend, contrast agents are divided into T_1 or T_2 agents. T_1 contrast agents, for instance, are generally based upon paramagnetic ions like gadolinium, Gd(III). Due to its high magnetic moment as well as its slow electronic relaxation time, the Gd(III) ion is able to interact with the excited water protons in its vicinity, thus accelerating their spin-lattice relaxation and therefore the signal intensity (equation 4). As a consequence, T_1 agents generate a bright spot on an MR image and are called positive contrast agents.

T_2 relaxation agents, on the other hand, are mainly based upon iron oxide, which can show a super paramagnetic effect and induce a large magnetic susceptibility. This distorts the local magnetic field around the iron and leads to a faster dephasing of the nuclear spins in close proximity, therefore a shorter T_2 and hence a signal loss in T_2 weighted images. By this means, a dark spot is generated on the MR image obtained with such negative contrast agents. The weight of each individual term of equation 5 is directly correlated to the echo time (T_E) and repetition time (T_R) chosen by the operator. Therefore, T_1 or T_2 weighted images can be obtained depending on which effect has to be maximised.

1.2.3 Contrast agents

As mentioned above, compounds based on paramagnetic ions like gadolinium (III) or manganese (II)/(III) as well as super-paramagnetic iron oxide nanoparticles are in the main focus of current research or already in clinical routine use.[22] Since free gadolinium ions are highly toxic, their *in vivo* use is only possible if they are encapsulated in highly stable coordinated complexes. Two famous examples of clinical approved contrast agents for MRI are Gd-1,4,7,10-tetraazacyclododecane-1,4,7,10-tetraacetic acid (Gd-DOTA) [DOTArem®, Guerbet, France] and Gd-diethylenetriaminepentaacetatic acid (Gd-DTPA) [Magnevist® , Bayer Healthcare, Germany]. Both complexes possess very high thermodynamic stability constants (>10^{20}) as well as a high kinetic inertness which avoids transmetallation reactions with endogenous cations. But even with such high complexation rates, complications are possible, like the rare syndrome of nephrogenic systemic fibrosis (NSF) in patients with kidney insufficiency. NSF was only observed with gadodiamide[23, 24], a previously FDA approved gadolinium contrast agent. Despite these possible serious side effects, gadolinium based contrast agents are still the almost exclusively used agents so far.

The only FDA approved manganese(II) contrast agent is the manganese chelate N,N´-dipyridoxal ethylenediamine-N,N´-diacetate 5,5´bisphosphate (Mn-DPDP) [Teslascan®, Takeda Pharmaceutical, Japan]. It should be noted that manganese(II) ions are often used in animal studies due to their sensitivity to a number of biological processes[25] which enables functional imaging in Manganese Enhanced MRI (MEMRI)[26] (see chapter 1.5.1). Several superparamagnetic iron oxide (SPIO) contrast agents were also approved and used in clinics, but only GastroMARK® [AMAG Pharmaceuticals, United States] and Lumirem® [Guerbet, France], an oral gastrointestinal imaging agent, are still in production.

Unfortunately, most available contrast agents are highly unspecific. Extensive research is underway to develop new agents with explicit targeting moieties, also utilizing nanotechnology, to strengthen the contrast enhancing features even further.[27-33] Although a lot of research is going on in this field, and the scientific output is high, nearly none of the

newly developed contrast agents have been even taken to phase I clinical trials. A way to achieve this might be the use of PET and SPECT in combination with MRI and CT leading to multi-modal imaging.

1.3 Emission tomography

Positron-Emission Tomography (PET) and Single-Photon-Emission Computer Tomography (SPECT) are non-invasive medical imaging methods enabled by the radiotracer method described in chapter 1.1. They are used for *in vivo* research studies and diagnostics showing the distribution behaviour of radioactive molecules within a body.[2] The use of radiotracers in this field is still increasing due to the extremely low concentrations of radiotracers necessary which do not disturb the biological system in any kind.[34]

In PET, the annihilation of a positron of a β^+-emitting radionuclide, like ^{18}F (half-life: 109.8 min), is used to locate the place of the annihilation in a body. After its emission the positron travels a short distance ranging from 1 mm to up to several mm, depending on its energy and the interacting matter, until it is nearly at rest. The positron can now interact with an electron in the surrounding matter producing a highly unstable atom-like state: The positronium.[35] The spins of these combined positrons and electrons can be aligned parallel or anti-parallel termed as the ortho- or para -positronium. The ortho-positronium cannot be used in PET due to the emission of an uneven photon number in the annihilation process caused by the Lorentz invariance. Additionally, its life time is with 142 ns 10^3 times longer than that of the para-positronium and therewith the possibility of an annihilation negligible small.[36] The para-positronium annihilates after an average lifetime of 0.125 ns and emits two photons with energies of 511 keV each.[36] If the starting positron was completely thermalized, the photons are emitted in a 180° angle. Due to the weak interaction of γ-rays with matter, the emitted γ-rays will penetrate the whole body and can be measured externally with a suitable detector. The detectors consist usually of scintillation crystals coupled to photomultiplier tubes. These are generally arranged in the geometrical form of a ring around the body in current positron-emission tomographs (see Figure 1). Several other configurations were used earlier, but they show a significantly poorer coincident detection (<30%) which promoted the use of the full-ring configuration.[37] An event of decay is counted as coincident if both photons of the annihilation process hit the opposing γ-ray detectors within a time window of 6-12 ns[37]. Thus, if scattering and attenuation of the detected photons is neglected, each measured annihilation event must have occurred in a straight line between the two opposing detectors.

Due to the radial emission of radioactivity, the origin of the decay can be determined by superimposition of the straight decay lines produced by multiple decays in the same area. This basic principle of analytical image reconstruction is used in the filtered back-projection depicted in Figure 2.[38]

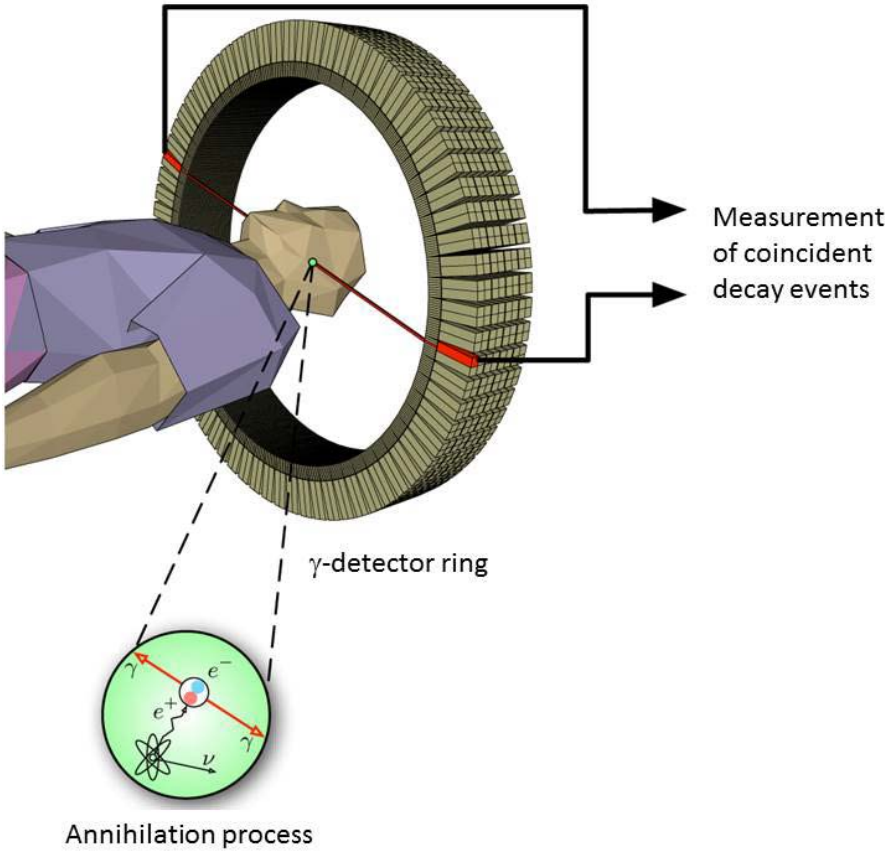

Figure 1: Annihilation process and γ-ray detector assembly of a PET, adapted from Maus.[39]

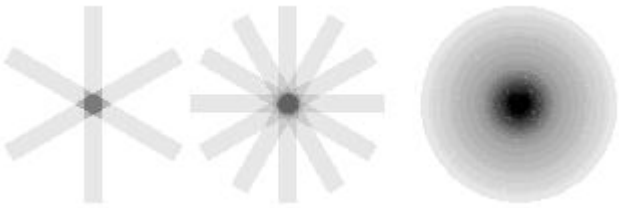

Figure 2: Example for reconstruction by superimposition of straight decay tubes between γ-detectors; adapted from Henkin et al.[38].

In a real two- or three-dimensional image, the scattering and attenuation cannot be neglected and have to be corrected to achieve a quantitative distribution image of the measured radionuclides. The correction can be done by independently measuring the scattering and attenuation with a body circling radioactive transmission source directly before or after the PET measurement, or by obtaining the attenuation and scattering map with CT. The result of

additional computation with this data is the two- or three-dimensional image of the quantitative distribution of the radionuclide with a resolution of approx. 5 mm with a clinical PET scanner.[40]

An additional interpretation of the obtained radionuclidic distribution is necessary for the determination of the kinetic behaviour of a compound. Therefore, a bio-mathematical model based on differential equations is required, describing the velocity constants of a radioactive compound changing between different spatial and/or biochemical compartments in the body, e.g. blood, intra- and extracellular space.[41] If one biochemical parameter, e.g. the abundance of the radionuclide in the blood, is measured over time and used as an input function, the differential equation can be solved and other unknown kinetic parameters can be calculated. This is limited to simpler models with two or three compartments because no distinct assignment of the calculated coefficients is possible with more complex models.

If the model conforms to the *in vivo* behaviour of a labelled compound, the arithmetical solution of these compartment models results in constants, depicting the *in vivo* local concentrations and kinetics of the labelled compound. With this method, a quantitative assessment of a specific biochemical function is possible with PET if a suitable labelled compound of known *in vivo* behaviour is available, matching a simple compartment model.

The principle of SPECT is analogous to PET, but differs mainly in the used radioisotopes and the detection of directly emitted γ-rays from them. In SPECT, radioisotopes with a high intensity γ-ray in the energy region between 100 and 300 keV are used, like ^{99m}Tc (half-life: 6 h). The radial emission of γ-rays originates from the place of the decayed radioisotopes, penetrates the body and is detected by a single or multiple NaI(Tl) scintillation detectors as depicted schematically in Figure 3.

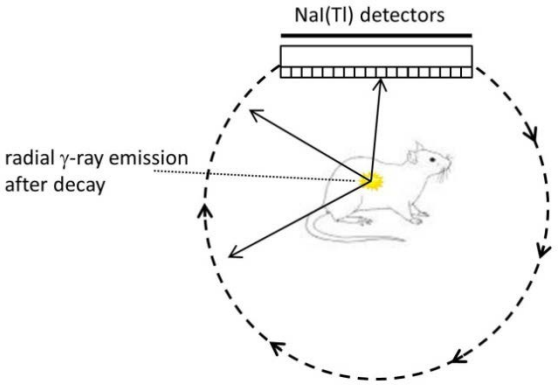

Figure 3: Schematic of the SPECT principle.

This results in a 2D image of the radionuclide distribution from the specific angle. The 3D image is acquired by orbiting the detectors around the body, recording multiple 2D images of

adjacent planes and reconstructing them into true 3D images analogue to the reconstruction methods used in PET as discussed above. However, in contrast to PET the scatter and attenuation corrections necessary for a quantitation of radiotracers in SPECT are even more demanding and prone to errors, leading to strongly varying absolute values. This is caused by the unknown depth dependency of γ-ray emitters in tissue Only extensive computational processing of the raw imaging data can solve this issue and produce quantitative values.[42] This method is still experimental and not yet applicable for clinical routine use.

Both imaging methods presented above have advantages as well as disadvantages. The main advantage of SPECT is strongly coupled with its most used single photon emitter ^{99m}Tc. It exhibits a convenient half-life of about 6 h and can easily be produced with a radioisotope generator. The generator can be used for several weeks 2-3 times a day. Additionally, the chemistry of ^{99m}Tc is so well known by now that a multitude of evaluated radiotracers are available by all-in-one synthesis kits at the place of use. For the production of a PET radiotracer, in contrast a large facility including a cyclotron, labs for radionuclide handling and highly qualified staff are necessary. Therefore, PET imaging can be realised in most cases only in close proximity to the radiotracer production facility because otherwise the necessary short lived radioisotopes would have decayed before reaching the imaging facility.
The advantage of PET over SPECT is the 100 times higher detection sensitivity which leads to a higher time resolution and therefore enables more sophisticated dynamic studies. Additionally, clinical PET scanners have a higher spatial resolution of approx. 5 mm in comparison to SPECT with approx. 10 mm.[40] The most important advantage of PET is its superiority concerning the quantitation of radioactivity *in vivo*. Although the quantitation possibility of SPECT has been proved by now[42], it is still limited and in its infancy and by no means ready for clinical application. By now the quantitation of clinically applied radiotracers such as 2-deoxy-2-[^{18}F]fluoro-D-glucose or *o*-(2-[^{18}F]fluorethyl*)*-L-tyrosine with PET are routine diagnostic procedures. In conclusion, PET, in comparison to SPECT, is more expensive and locally bound to a large scale facility for radiotracer production, but PET is the technically more advanced method with better sensitivity, better spatial resolution and superior quantitation capabilities. These advantages can be further increased by introduction of multi-modal imaging by combination of PET with morphological imaging modalities like CT or MRI.

1.4 Multi-modal imaging and smart contrast agents

Multi-modal imaging is the combination of two or more imaging methods to simultaneously measure complementary information. A new class of contrast agents utilizing the full potential of this multi-modal imaging is emerging and is called responsive or smart contrast agents.. Stand-alone, non-invasive imaging systems like MRI, PET, CT and SPECT have been in clinical routine use for decades now.[1, 2] In recent years more advanced systems were developed enabling the parallel measurement of diagnostically relevant information in a shorter time period. For example, PET/CT systems deliver higher morphological contrast in a shorter measurement time by use of the CT for the attenuation and scatter correction necessary for quantitation with PET making additional transmission source measurements redundant. After its introduction in 1998[43] and its commercial availability in 2001, the number of deployed systems rose exponentially to 500 worldwide within three years.[44] A similar approach was taken to combine PET and MRI systems pairing the high soft tissue contrast of MRI with the quantitative assessment of biochemical functions of PET. A first prototype for humans was developed in 2007[45] and a first commercial PET/MRI system has been available since 2011.[46]

The longer development time was due to the high magnetic field interfering with the state of the arts photomultiplier tubes.[47, 48] Only the introduction of avalanche photodiodes[49] enabled the production of a PET inlay working inside of a MRI machine like the *BrainPET* inside a 3T MRI of the Forschungszentrum Jülich produced by Siemens Healthcare.[50] However, the question, if the combination of PET and MRI is advantageous for every clinical use or medical research, has not been completely answered until now.[44] The clear advantages of PET/MRI are the lower irradiation dose induced on patients, higher soft tissue contrast and the possibility to realise responsive bi-modal imaging probes combining the high spatial resolution with the quantitation capabilities of PET.[51] The major disadvantage of PET/MRI are the longer measurement times and the associated necessary movement corrections in addition to the still problematic attenuation and scatter correction necessary for PET quantitation.[44]

The development of currently proposed responsive contrast agents[33] may tip the scales in favour of PET/MRI.[52] The concept of responsive or smart contrast agents is based upon chemical moieties which induce a varying contrast enhancement of the agents depending on a biochemical function or tissue state like redox condition, temperature or pH-value. In case of pH-sensitivity, the deprotonation of a contrast agent moiety leads to a partial blocking of water interaction with the complexed ion resulting in longer relaxivity times and hence a signal intensity loss in T1 or T2 weighted images. If the concentration of the contrast agent at the precise location of the signal loss is known, a correlation between relaxivity and pH can

be drawn and hence the pH can be determined *in vivo*. Another example is the redox state in tissue which is strictly regulated in healthy tissue, and changes can also be linked to several pathologies.[33] For redox responsive agents a redox couple like Mn^{2+}/Mn^{3+} is needed which changes relaxivities depending on its oxidation state. The most difficult, but also most valuable approach, would be a responsive contrast agent for enzyme activity. A water exchange inhibiting moiety which possesses an enzyme cleavable link is needed at the contrast agent to achieve this. The specific enzyme activity could be determined by successive measurements due to increase of relaxivity and, hence, contrast. Unfortunately, all those approaches are still in development and in need of suitable radionuclides to enable simultaneous PET imaging for quantitation.[53]

Another interesting approach is the utilization of clinically well-established SPECT. Since the development of new algorithms for image reconstruction and compensation techniques for photon attenuation and scattering corrections, the SPECT method is also viable for (quantitative) functional *in vivo* distribution studies.[42] The evaluation of newly developed MR contrast enhancing agents can therefore now also be conducted if a radionuclide suitable for SPECT is available.

1.5 Radionuclides of interest for PET/MRI and SPECT

In order to realise quantitation of multi-modal agents, several standard PET isotopes (^{18}F, ^{68}Ga, ^{125}I) can be considered for labelling purposes. Unfortunately, all of them are non-isotopic and change the original contrast agent. The outcome may be an altered *in vivo* behaviour due to a deviating chemical structure (^{18}F, ^{125}I) and/or lipophilicity (^{68}Ga), which would neglect the effort of providing a chemical analogue with an identical distribution in the body. Especially manganese has gained more attention in the last two decades due to its increasing use in MEMRI for novel studies to decipher several biological processes. Therefore, the focus of this work was on the production of PET or SPECT suitable isotopes of the previously described main T_1 contrast enhancing elements manganese and gadolinium.

1.5.1 Properties of radiomanganese

Beside the research for new manganese chelate based contrast agents, the natural mono-isotopic occurring ^{55}Mn ion is currently increasingly used in animal studies with MEMRI as mentioned above. The element is an essential trace element in the human and animal body, however, higher doses have neurotoxic effects and lead to symptoms similar to Parkinson disease.[54] Therefore, MEMRI operates normally at the lowest mass of contrast agent

possible [25, 55-57], but it is still not approved for application in humans. Until now the visualization of activity in the brain and the heart, the trace of neuronal specific connections in the brain and also the enhancement of the brain cytoarchitecture after systemic dose application can be achieved by MEMRI in animals.[25] Additionally, work is done bringing MEMRI closer to human application [58], which calls for reliably stable new contrast agents as well as reliable *in vivo* distribution data[59]. The utilization of radioisotopes of manganese is another evaluation tool to achieve those goals. The available radioisotopes with half-lives between 20 min and one year are summarised in Table 1. The cross sections of proton induced reactions on ^{nat}Cr leading to ^{51,52g,m}Mn are depicted in Figure 4.

Table 1: Properties of radiomanganese isotopes taken from ENSDF[60] and possible nuclear reaction channels with corresponding threshold energies[61] without consideration of the coulomb barrier.

Isotope	Half-life	β^+-abundance [%]	Max. β^+-energy [MeV]	γ-rays [keV] (intensity [%])	Nuclear reaction channel	Threshold energy [MeV]
^{51}Mn	46.2 min	97.08	2.186	749.1 (0.26)	^{52}Cr(p,2n) ^{53}Cr(p,3n) ^{54}Cr(p,4n)	16.3 24.4 34.3
^{52g}Mn	5.59 h	29.6	0.576	744.23 (90.0) 935.54 (94.5) 1434.07 (100)	^{52}Cr(p,n) ^{53}Cr(p,2n) ^{54}Cr(p,3n)	5.5 13.4 23.2
^{52m}Mn	21.1 min	96.5	2.633	377.75 (1.7) 1434.07 (98.3)	^{52}Cr(p,n) ^{53}Cr(p,2n) ^{54}Cr(p,3n)	5.9 13.8 23.5
^{54}Mn	312.3 d	0	-	834.85 (99.98)	^{54}Cr(p,n)	2.2
^{56}Mn	2.58 h	-	-	846.77 (98.9) 1810 (27.2)	^{55}Mn(n,γ)	0

Two main production routes are available for suitable radiomanganese isotopes: The irradiation of elemental chromium or compounds of it with charged particles leading to ^{51,52g,54}Mn, or the irradiation of natural manganese with neutrons for production of ^{56}Mn. Each radioisotope and production route has advantages and disadvantages. The positron emitting

isotopes ^{51,52g}Mn are available by cyclotron production[62-64] and enable *in vivo* quantitation with PET. The major downside is the need of excessive radiochemical work to separate the irradiated macroscopic mass of chromium from the produced radionuclides and the necessary radiosynthesis of the targeted compound afterwards.[65]

The radionuclides ^{54}Mn and ^{56}Mn are both not applicable in emission tomography. The long lived ^{54}Mn completely decays by electron capture which renders the isotope useless for PET. For extended laboratory or *ex vivo* animal studies with autoradiography (ARG), the isotope can be considered due to its high intensity γ-ray line. The β^--emitter ^{56}Mn, on the other hand, is directly produced by the neutron induced nuclear reaction on ^{nat}Mn[66] and can be used after the separation from ejected ions by the Szilard-Chalmers-effect. The amount of ejected ions is strongly dependent on the chemical bonding of the Mn atoms in the molecules or particles. No considerable radioactive by-products are produced with thermic neutrons due to the mono-isotopic abundance of ^{55}Mn and no more complex nuclear reaction channels are available besides the ^{55}Mn(n,γ)^{56}Mn reaction at these neutron energies. The disadvantage of the neutron produced ^{56}Mn is the low specific activity because of the direct irradiation of macroscopic masses of manganese, and that its application to imaging is limited to ARG. However, for preliminary and proof of principle *in vitro* and *ex vivo* experiments ^{56}Mn is useful.

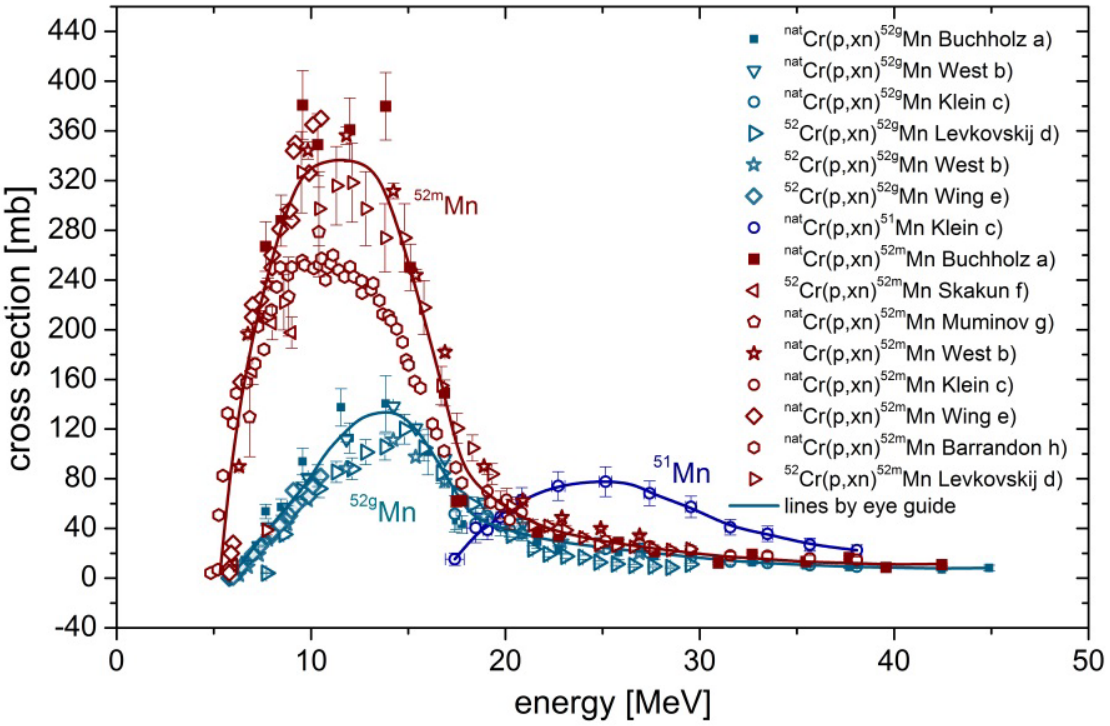

Figure 4: Cumulative cross sections of proton induced nuclear reactions on ^{nat}Cr leading to ^{51,52g,m}Mn adapted from a) Buchholz et al.[65] b) West et al.[64] c) Klein et al.[62] d) Levkovskij et al.[67] e) Wing et al.[63] f) Skakun et al.[68] g) Muminov et al.[69] h) Barrandon et al.[70].

The decay properties of the neutron deficient isotopes show high positron emitting probabilities for the shorter lived ^{51,52m}Mn making them promising for use in PET. Unfortunately, their maximal β^+-energy is 2.2 and 2.6 MeV, respectively, which decreases the resolution drastically, and further on, their half-lives of 46 and 21 min are not feasible for observation of longer biochemical processes with PET. The shorter half-lives also limit their application for development of target separation and radiosynthesis.

The most promising candidate for radiosynthetic development and initial PET studies is ^{52g}Mn due to its low maximal β^+-energy and even lower average β^+-energy of 245 keV, which is one of the lowest available. Even though, the lower positron-emission fraction of just 30 % and the high intensity γ-rays are problematic. The half-life of 5.6 d is also a limitation for repetition experiments in conjunction with the biological half-life of the respective compound, but allowing observation of slower biochemical processes otherwise. Comparing all available radionuclides of manganese different application areas become evident. While ^{52g}Mn seems to be the most suitable manganese radioisotope for the development of separation and radiosynthesis methods, it is also beneficial for first PET studies as shown by Topping et al.[71]. However, if target separation and the radiosynthesis are established, ^{51}Mn seems the optimal radionuclide of manganese for a later *in vivo* application in PET.

1.5.2 Properties of radiogadolinium

Although there are no radiogadolinium isotopes with high β^+-emission probabilities and suitable half-lives for PET, radiogadolinium isotopes are of high interest to investigate their potential for SPECT imaging. All of the relevant neutron deficient gadolinium isotopes and some of their respective properties are summarised in Table 2.

Table 2: Decay properties of gadolinium isotopes[60] with γ-rays suitable for SPECT (bold), complementary γ-rays for activity determination (italic), possible nuclear reaction channels and corresponding thresholds[61] without consideration of the coulomb barrier.

Isotope	Half-life	EC decay abundance [%]	γ-rays [keV] (intensity [%])	Nuclear reaction channel	Threshold energy [MeV]
^{146}Gd	48.27 d	100	**114.7 (44)** **115.5 (44)** **154 (46.6)**	^{151}Eu(p,6n) ^{151}Eu(d,7n) ^{153}Eu(p,8n) ^{153}Eu(d,9n)	40.0 42.5 54.9 57.5

Table 2 cont.

Isotope	Half-life	EC decay abundance [%]	γ-rays [keV] (intensity [%])	Reaction channel	Threshold energy [MeV]
^{147}Gd	38.06 h	99.74	**229.3 (57.7)** *370.0 (15.7)* *396.0 (31.4)*	^{151}Eu(p,5n) ^{151}Eu(d,6n) ^{153}Eu(p,7n) ^{153}Eu(d,8n)	32.6 35.0 47.5 50.1
^{149}Gd	9.28 d	99	**149.7 (48.2)** **298.6 (28.6)** *788.9 (7.3)*	^{151}Eu(p,3n) ^{151}Eu(d,4n) ^{153}Eu(p,5n) ^{153}Eu(d,6n)	16.6 18.9 31.5 34.0
^{151}Gd	124 d	99	**153.6 (6.2)** **174.7 (3.0)** *243.3 (5.6)*	^{151}Eu(p,n) ^{151}Eu(d,2n) ^{153}Eu(p,3n) ^{153}Eu(d,4n)	1.3 3.5 16.2 18.6
^{153}Gd	240.4 d	100	**97.4 (29.0)** **103.2 (21.1)**	^{153}Eu(p,n) ^{153}Eu(d,2n)	1.3 3.5

All of the listed radionuclides exhibit β^+ radiation emission probabilities below 1 % and therefore low background radiation for actual SPECT measurements. Further selection criteria for radioisotopes suitable with SPECT are high intensity γ-rays with energies in the efficiency maximum of NaI(Tl)-detectors at approximately 150 keV and suitable half-lives. These have to be long enough for precise measurement but short enough for timely excretion or decay to assure low radiation doses inflicted on animals or patients. In some cases half-lives allowing repetition experiments in a timely manner can be additionally favourable. Keeping this in mind, $^{146,151\text{ and }153}$Gd have optimal γ-ray energies with more or less high intensities, but their physical half-lives are too long for *in vivo* application with humans in SPECT. The half-live of ^{147}Gd of 38.06 h is suitable for *in vivo* studies. The high intensity γ-rays of this isotope have higher energy than ideal but are still useful for SPECT as shown before by Denzler[72].

The radionuclide ^{149}Gd shows a more suitable γ-ray for SPECT at 149.7 keV with a high intensity of 48.2 %. The longer half-life makes it perfect for chemical development work. However, not only PET but also SPECT measurements are in need of radioisotopes with high radionuclidic purity due to the low resolution of NaI(Tl) γ-ray detectors (approx. <50keV). In detail, γ-rays with similar energy would produce overlapping photopeak areas in the measured γ-ray spectra. In case of a smaller overlap, no significant integration of the photopeak area is possible, and in case of a complete overlap the necessary decay correction becomes problematic which both lead to a distorted radioactivity determination. This is especially problematic for the isotopic pair ^{149}Gd and ^{151}Gd due to similar γ-ray and threshold energies for the proton and deuteron induced reactions on europium. Another important factor is the accumulation of radioactive daughter nuclides of gadolinium, namely ^{147}Eu (half-life: 24.1 d) with two prominent γ-rays (121 keV, 22.9 %, 197 keV, 27 %) and ^{149}Eu (half-life: 93.1 d) with two minor intensity γ-rays (277 keV, 3.6 %, 327, 4.0 %)^{147,149}Eu.
Unfortunately, only few studies have examined the production[73-76] or separation[77-79] of ^{147,149}Gd until now, partly owed to the higher particle energies or uncommon projectiles needed for irradiation or partly owed to a necessary complex radiochemistry for separation.

1.6 Production of radionuclides

The production of radionuclides is a complex procedure based on several development steps.[1] At first, the decision has to be made which radionuclide could be suitable for the targeted application: A proton or a neutron deficient radioisotope (see chapter 1.5.1 and 1.5.2). Further on, reaction channels have to be considered leading to this chosen radioisotope. Connected to those reaction channels is the search for a suitable target material which has to endure the partly harsh conditions of irradiation without suffering material loss. Also, an evaluation of the irradiation parameters based on cross section measurements and achievable thick target yields has to be conducted. The irradiation parameters should deliver suitable radioisotopic yields, purity and be cost efficient. Here, only low or non-isotopically enriched target materials are favourable. Additionally, a facile separation procedure from the target material has to be developed for most neutron deficient isotopes. The separation procedure should yield radiochemically pure, no-carrier-added (n.c.a.) radionuclides in a small volume of a medium suitable for the subsequent task. Also, the separation should be done in the shortest time possible to reduce loss of radioactivity by decay and the radiation exposure of an operator to a minimum. For imaging, an especially high isotopic and chemical purity combined with a high specific radioactivity is advanteagous.

1.6.1 Irradiation facilities

As mentioned in chapter 1.5.1 the irradiation with neutrons or charged particles is mainly used for production of proton or neutron deficient radioactive isotopes. The major routes to produce neutrons for irradiation are the use of a nuclear reactor[2, 80], a neutron source[1] and secondary neutrons produced at a charged particle accelerator[81, 82].

In the present work the main focus was on neutron deficient radionuclides, so their production is discussed in more detail. The production route towards the neutron deficient radionuclides is generally based upon the acceleration of charged particles such as protons, deuterons, α-particles or heavier elements and the subsequent bombardment of a target with those. Three different concepts have been developed for the acceleration of charged particles: linear accelerators, cyclotrons and synchrotrons. The linear accelerator (linac) was the first machine developed for acceleration of electrons based on an idea of Leó Szilárd and developed by Rolf Widerøe[83] in 1928. Later on, the variety of accelerated particles was expanded to heavier charged particles like protons.

The principle of a linac is a succession of cylindrical hollowed electrodes with small gaps between them within a larger cylindrical vacuum chamber. When an ion is introduced into the vacuum chamber, it is accelerated to the opposing charged first electrode. The electrode switches its polarity while the charged particle is passing through accelerating the particle further by repulsion after it exits the electrode. By alternation of polarity between the subsequent electrodes, the charged particle is further accelerated within the gaps between electrodes. The drawback of this acceleration system is the large space needed to reach higher velocities and a limited fractionated particle flux. Hence, the cyclotron, a spiral-accelerator system, was developed by Ernest O. Lawrence[4] depicted in Figure 5.

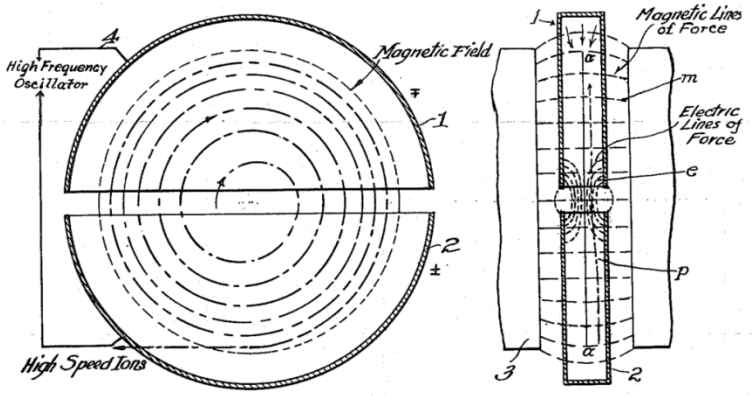

Figure 5: Original drawing of Ernest O. Lawrence from his patent in 1934 of the principle of a cyclotron.[4]

After injection, the charged particle is accelerated towards one of the polarised hollowed Dee electrodes, named for its D shape. The accelerated particle is forced upon a circular orbit by

the Lorentz force by strong permanent magnets above and below the double Dees. Due to an applied high frequency electronic field the electrodes change their polarity with each transition of the charged particle between them, thereby accelerating it. With increasing velocity, but a constant magnetic field, the angular velocity of the particle stays the same forming a spiral-shaped orbit because of the centripetal force enabling the parallel acceleration of multiple particles at once. Thereby, a higher flux compared to linac´s is possible.[2] But the velocity is still limited due to occurrence of relativistic effects when nearing light speed.

This can be corrected to some extent by focusing the beam with a azimuthal varying magnetic field at the outer rims of the cyclotron.[84, 85] Then it is possible to reach nearly 80 % of the speed of light (590 MeV protons) shown by the Ring cyclotron[86] located at the Paul Scherrer Institut in Switzerland.

The only option to reach higher velocities is the application of larger synchrotron rings. The acceleration occurs similar to a linac accelerator, but with the addition of bending magnets guiding the particle beam onto a circular orbit. By synchronising the strength of the bending magnets, the circular orbit can be maintained with increasing velocity of the particle. Extremely high kinetic energies can be reached of presently up to 7 TeV protons in the Large Hadron Collider of CERN[87]. The kinetic energy is mainly limited by the loss of energy through synchrotron radiation formed by deflection of the particles within the bending magnets. However, the extremely high energies of a synchrotron are mainly interesting for particle physics and no reliable production of radionuclides is possible due to the low flux and the extremely complex nuclear reactions at these high energies with low reproducibility.

Therefore, the optimal production route for short and longer lived pharmaceutical relevant radioisotopes is still the irradiation of a suitable target material at a level I to level III sized cyclotron. The optimal energy range for production of specific radionuclides, and therefore the needed cyclotron size is strongly depending on each nuclear reaction, their possible by-products and has to be experimentally determined for each single case. In case of the present work all neutron-deficient radioisotopes were produced at a small or medium sized cyclotron.

1.6.2 Production parameters

For a successful radioisotope production using charged particles the most important factor is the cross section of the nuclear reaction as shown in the activation equation 6[80]:

$$A_{eob} = \sigma \cdot \phi \cdot N \cdot H \cdot \left(1 - e^{-\lambda t_{irr}}\right) \cdot e^{-\lambda t_{cool}}$$

with *A*: half-life corrected activity at the end of bombardment (EOB),

σ: nuclear reaction cross section at the corresponding particle energy,

ϕ: particle flux density,

N: number of irradiated target atoms,

H: isotopic abundance of the targeted isotope,

λ: decay constant of the radionuclide,

t_{irr}: irradiation time,

t_{cool}: time from the end of bombardment to the measurement.

The particle flux density and the number of irradiated target atoms effects all produced radionuclides in the same way for proton and neutron irradiations, targeted radionuclides as well as by-products. The cross section of different nuclear reactions varies with the particle energy. Additionally, charged particles show a significantly higher energy transfer to matter than neutrons[2] as shown in Figure 6 due to their Coulomb interaction with the charges of shell electrons and atom nuclei.

Therefore, selection of a suitable energy range can explicitly favour the production of one specific radionuclide, making precise cross section determination even more important. Cross sections of nuclear reactions induced by charged particles are mainly determined by the stacked foil technique[88, 89]. A foil stack is exemplary depicted in Figure 6.

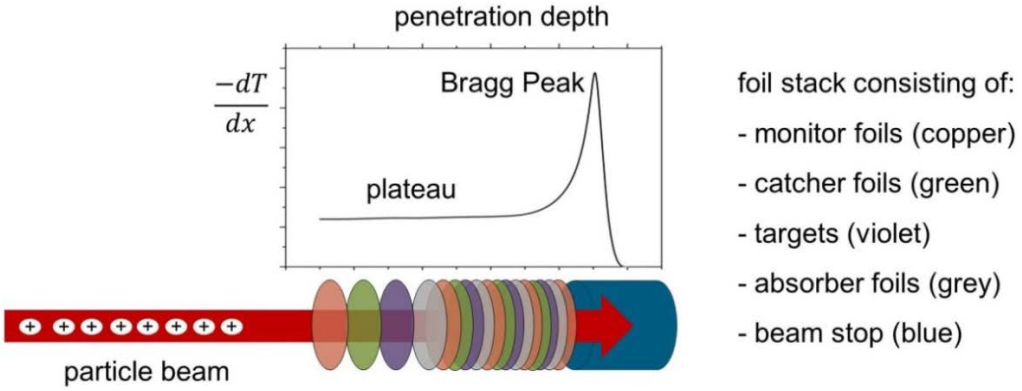

Figure 6: Stacked-foil technique and specific energy loss in matter for heavy ions.

By alternating the actual targets, foils for energy degradation (absorber), foils for beam flux and energy determination (monitor foils) and foils catching eventually ejected radionuclides (catcher foils) a large energy range can be measured in one irradiation. Due to the strong interactions between charged particles, matter and the strong dependence of cross sections on particle energy, very thin targets are mandatory to determine accurate cross sections. This way cross sections can be measured at a rather precise particle energy and not as mean values over a broad energy range which differ dramatically. Generally speaking, targets for cross section measurements should degrade particle energy as little as possible

with the produced radionuclides still measurable after a reasonable irradiation time. A more detailed description of the exact target materials used and irradiation parameters for cross section measurements is given in chapter 3.2.1. With this basic approach, the production survey of the nuclear physical data necessary to produce above mentioned isotopes is possible as depicted for ^{51,52g,m}Mn in Figure 4. For further application, separation of the produced radionuclides from the bulk target material and purification with feasible procedures may be mandatory.

1.7 Separation techniques

Several physical-chemical separation techniques are applicable for the isolation of radionuclides from bulk target materials. This includes for example Thermochromatography (TC), Liquid-Liquid Extraction (LLX), Ion-Exchange Chromatography (IEC), Extraction Chromatography (EXC), High Pressure Liquid Chromatography (HPLC), co-precipitation methods and electrochemical methods. Some are more suitable for the task to separate picomolar amounts of radioactive material from millimolar amounts of the bulk targets than others. In general, the optimal separation method depends strongly on the composition of the target, the chemical nature of the irradiated material and the produced radionuclide. Also, the conditions for further processing are necessary to consider. In this work two chromatographic separation methods were of special interest (see chapter 3.4.1 and 3.5.2) due to their favourable separation performance and possible translation to semi-automated systems.

1.7.1 Ion-exchange chromatography

In general, the separation achieved with chromatographic methods is based upon the different distribution behaviour of two or more substances between a mobile and a stationary phase.[90] The classification of different chromatographic methods depends on the aggregate state of both phases. Ion-exchange chromatography is part of the liquid chromatography separation methods with a liquid mobile and a solid stationary phase. The stationary phase in most modern ion-exchange chromatography is made of a mesoporous polymer resin with ion exchanging groups bound to the surface. Depending on the charge of these exchange groups, the resins are affine to anions or cations. The scaffold of the resins is typically a matrix of polystyrene cross linked by co-polymerisation with divinyl benzene. Cross linkage varies normally between two and twelve percent and increases sturdiness, but decreases the ion-exchange capacity of the resins. After the polymerisation process, the matrix is functionalised with the exchange groups differentiating the resins into four groups: strongly basic (quaternary amino groups), strongly acidic (sulfonic acid groups), weakly basic

(primary, secondary and/or ternary amino groups) and weakly acidic (carboxylic acid groups) resins. These functional groups exchange charged ions with the mobile phase at different rates based on parameters such as ion size, charge and complexation rates in the mobile phase.[91] The exchange rates for different ions can deviate strongly from each other leading to different retention times when traveling through the stationary phase. The equilibrium state can vary between complete to no retention enabling the separation of two or more ions on one column. The quality of a separation can be expressed by Nernst´s distribution coefficient (K_D) and the separation factor (SF) as[90]:

$$K_{Dx/y} = \frac{c_{sp}}{c_{mp}}$$

$$SF_{x/y} = \frac{K_{Dx}}{K_{Dy}}$$

with $K_{Dx/y}$: distribution coefficient of ion x and y,

c_{sp}: equilibrium concentration of ions in the stationary phase,

c_{mp}: equilibrium concentration of ions in the mobile phase,

$SF_{x/y}$: separation factor of substance x and y.

Determining the SF of ion pairs in a mixture on a specific resin with a set of eluents enables the development of a separation method. In an ideal case ($SF_{x/y}$ -> ∞), one of the substances in the mixture would be completely adsorbed on the column ($K_{Dx} = \infty$) while the other is mobile ($K_{Dy} = 0$). In this ideal case the eluent is changed after removing the mobile component and the other bound substance eluted. For most ion pairs these basic ion exchange resins are sufficient to achieve a satisfying separation. In some cases, however, the commercially available ion exchange resins only lead to an incomplete separation and other chromatographic methods are more advantageous.

1.7.2 Extraction chromatography

Extraction chromatography (EXC) can be described as a specialised subgroup of Liquid-Liquid-Extraction (LLX) for separation of metal ions.[92] In contrast to IEC organic complexing agents are used as hydrophobic stationary phase. Thus, it combines the selectivity of Liquid-Liquid extractants with the functionality of a column chromatography. Commonly used extractants are Di-(2-ethylhexyl)-orthophosphoric acid (HDEHP), Tri-n-butylphosphate (TBP), long-chained aliphatic amines and crown ethers. These extractants are adsorbed by physical means to an inert supporting matrix mainly composed of mesoporous silica or organic polymers with bead sizes of 50-100 μm. The resin preparation involves the solvation of the

extractant in a volatile solvent, impregnating the support matrix with the mixture and evaporating the solvent. The capacity is limited by the amount of extractant absorbable on the supporting matrix. In general, the capacity is lower than that of an ion-exchange resin limiting its application to separations where the bulk target material is not extracted onto the resin. Additionally, due to the nature of physical absorption of the extractant on the target matrix a breakthrough of extractant is possible if high pressure chromatography conditions or specific organic solvents are applied. The capacity in combination with the distribution coefficients as well as the physical and chemical stability of the resin are therefore the major selection criteria for a feasible separation in this case.[93]

Another difference of EXC to IEC is the chemical change of the extractants. While the functional groups of IEC undergo only minor chemical changes, extraction chromatography is governed by several complex chemical processes and exchange equilibria.[92] Hence, beside the most commonly used inorganic acids the utilization of complexing agents like oxalic acid in the mobile phase can be beneficial. Due to this complexity, more parameters need to be optimised for a separation procedure. The quality of separation is calculated identical to the ion-exchange approach by measurement of Nernst´s distribution coefficients and separation factors as described in equation 7 and 8.

1.8 Separation of the lanthanides europium and gadolinium

The separation methods of the lanthanide series are mainly based on two properties: The first is the lanthanide contraction which leads to a decreasing ion radius of their trivalent ions in course of the period and hence, a decreasing basicity. On that account the complexes of the lanthanides increase in stability with strong bases opposing to their own decreasing basicity. The second property is the differing stability of their oxidation states and their different redox potentials. While for europium the bivalent state is relatively stable, no bivalent state is known for gadolinium.

While there are several approaches for near quantitative separation of europium and gadolinium using this two properties, they take too much time, are not practicable for n.c.a masses or need extremely specialised laboratory equipment[94-106]. The different separation methods involved are liquid-liquid extraction, ion-exchange, high pressure liquid chromatography, extraction chromatography, chemo-, and electro-reductive methods.

Each method has its own advantages and problems. Liquid-liquid extraction, for example, yields good separation factors, but the used volumes tend to be relatively large which is highly impractical for n.c.a. material, later labelling and or injection. Ion-exchange only gives relatively low separation factors of up to 2.2[95] which is enough for a baseline separation of an europium and a gadolinium fraction, if both are present in nearly equal amounts. But

those separations take much time in addition to possible superimposition of europium and gadolinium fractions, in case of the ratio of 10^8 with one metal in n.c.a. amounts. The introduction of high pressure separation systems resolved the time problem, due to higher flow rates and also yields better separation factors.[105] However, preparative HPLC systems are highly technical demanding because of the need of acid resistance as well as sufficient loading capacities to separate the bulk target masses from n.c.a. radionuclides.

On the other hand, the new generation of extraction resins yields superior separation factors and allows smaller separation volumes at the cost of their loading capacity.[107] DGA normal extraction resin (Triskem), for example, shows a capacity of 12 mg Eu/mL resin. This is optimal for pre-concentrations at trace amounts or a fine separation, but not suitable for bulk targets up to 500 mg and more due to the combination of high back pressure and decomposition of the resin under HPLC conditions described by the supplier which leaves large columns not viable.

However, the selective reduction of europium to its bivalent or elemental state and a following separation seem to give good yields in a short time.[108] The difference of their redox potentials (see Table 3) is high enough for this selective reduction.

Table 3: Redox potentials of Eu- and Gd-oxidation states, taken from Herman et al.[109]

Element	$E_{III/II}$ [V]	$E_{III/0}$ [V]
Eu	-0.30	-2.00
Gd	(-2.85)	-2.27

The reduction can be done by electrochemical or chemical reductive means. While electrochemical methods are time consuming[106], selective chemical reductions can be achieved within minutes.[77, 78, 108] The exact procedures will be described in chapter 3.4.1 and discussed in chapter 4.2.

1.9 Nanotechnology

The word “nanotechnology” was first used by Norio Taniguchi at a presentation on an international conference in 1974[110] and later on made publicly aware by the book of Eric Drexler “Engines of Creation: The coming Era of Nanotechnology”[111]. Drexler was inspired by the presentation: “There is plenty of Room at the Bottom” by Richard Feynman in 1959[112] proposing the direct manipulation of individual atoms as a new and more powerful form of synthetic chemistry. Nanotechnology was thereby defined to be “the manipulation of matter on an atomic, molecular, and supramolecular scale”.[111] Later on, a more general definition

was established by the National Nanotechnology Initiative[113], defining Nanotechnology as the manipulation of matter with at least one dimension sized from 1 to 100 nm. These nanometer scale materials or structures exhibit new physical properties or physical phenomena similar to newly found features in quantum mechanics.

While a large amount of new nanoscale materials was produced, new tools for characterisation also emerged simultaneously, but not exclusively, for these materials. Among them are dynamic light scattering (DLS), scanning or transmission electron microscopy (SEM/TEM), x-ray diffraction (XRD) and x-ray photoelectron spectroscopy (XPS). Even with the newly established characterization methods, there may be still more unique and unknown properties of nanoscale materials not found until now.[114] This is especially problematic considering the widespread use of nanotechnology in today's society. In many industrial as well as cosmetic products nanotechnology is an indispensable implement nowadays. Examples are the antibacterial coatings of refrigerators with silver nanoparticles, the application of TiO_2 in white paint and many more. Additional cross-disciplinary work is still needed in the future to assess every aspect of these products to assure their safety. The present thesis also deals with nanoparticle based systems for possible contrast agents in MRI. Therefore, only corresponding information necessary for the synthesis and characterization of nanoparticles will be displayed in the following.

1.9.1 Synthesis methods

Several synthesis routes leading to well-defined sizes, shapes and chemical compositions of nanosized particles have been established, but not all of them are completely understood. They can be classified in various ways, for example into the "top-down" and "bottom-up" approach.[114] The "top-down" approach which is in general an extension of lithography includes the breakdown or shaping of larger aggregates into smaller pieces or structures. The break down can be realised for example mechanically with grinding mills and the precise shaping with focused ion beams, atomic force microscope tips or by atomic layer deposition. "Bottom-up" approaches include every synthesis route, i.e. solid-, liquid-, vapour- and hybrid-phase growth based methods, which starts building nanosized materials from atoms or molecules into colloidal dispersions. The advantages of the "top-down" methods is the industrial upscaling possibility while higher chemical purity as well as lesser defects and a higher short and long range crystal ordering can be achieved with "bottom-up" methods.

The basic challenges of both approaches are the same:

- Development of a reproducible synthesis method resulting in nanomaterials with desired chemical composition, crystallinity, morphology and size, hence, producing nanoscale materials with required physico-chemical properties.

- Overcoming the huge surface energy present due to the large surface to volume ratio of nanoparticles.
- Sufficient stability to prevent coarsening by agglomeration or so called “Ostwald ripening”[115]. The latter is defined as a steady transfer of matter from smaller to larger particles decreasing the overall free energy of the system by lowering the surface tension of the resulting larger particles.

Considering the actual production, the first synthetic step towards nanoscale particles can be achieved by either the kinetic approach or the thermodynamic equilibrium approach. The kinetic approach includes the use of a limited space or a amount of precursor available. A template-based deposition, aerosol pyrolysis or a microemulsion are examples for kinetically controlled nanoparticle synthesis. The basic principle of the thermodynamic equilibrium technique can be explained by the model of Victor La Mer[116] depicted in Figure 7.

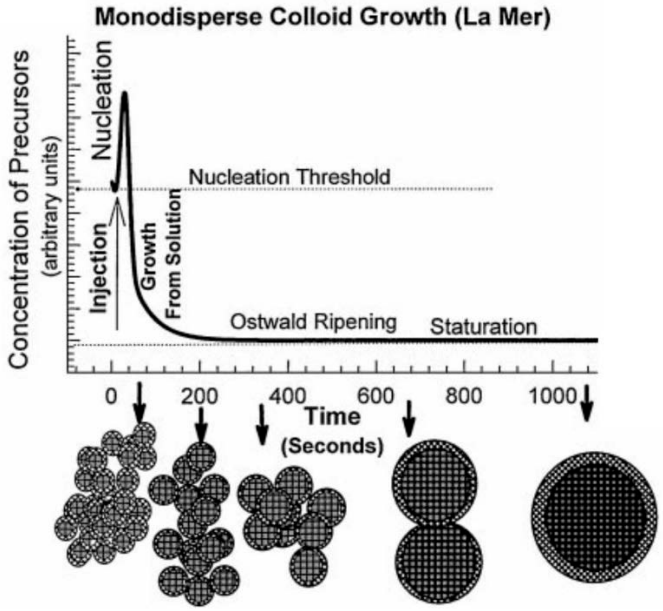

Figure 7: Simplified stages of nucleation and growth inside the La Mer diagram for an exemplary bottom-up nanoparticle synthesis; adapted from Murray et al.[117]

The basic steps of the thermodynamic equilibrium technique are the generation of a supersaturation in a solution by various means, the homogeneous nucleation and a subsequent particle growth.[114] The main driving force of the nucleation and growth process is the reduction of the Gibbs free energy (ΔG) towards an energetically lower system state by a phase transition. If the concentration of a substance is increased above the equilibrium concentration, the Gibbs free energy rises also. At this state, the formation of a new phase reduces the Gibbs free energy by removing the supersaturated compound from the solution into the second phase. But the creation of the new surface between the two phases requires a certain surface energy which counter balances the Gibbs free energy reduction. Hence, a

critical minimum size of a particle in a specific system can be deduced by the radius dependent Gibbs free energy. This radius is strongly correlated to the solvents and the level of supersaturation.

In a subsequent step, the growth to the final size distribution has to be controlled. It is governed by a) generation of growth species, b) diffusion of the growth species from bulk to the growth surface, c) adsorption of the growth species onto the growth surface and d) surface growth through irreversible incorporation of growth species onto the solid surface.[114]

The growth towards monodisperse nanoparticles can be influenced by several parameters like the overall mass and the controlled supply of growth species present in solution, the viscosity of the solvent as well as temperature and the application of a growth regulating diffusion barrier represented by a monolayer of surface capping agent.

To achieve well-defined shapes and sizes for nanoparticles of different compositions, several synthesis methods can be used each with its unique requirements caused by the many adjustments possible. A more in-depth discussion about the advantages and disadvantages of each technique is far beyond the scope of this work and can be found in literature.[114, 118] More relevant is the characterisation of said nanomaterials and the used methods therefore.

1.9.2 Characterisation of nanomaterials

For a full description of a specific nanomaterial, several characteristic properties can be assessed such as melting point, crystal structure, lattice constants, mechanical properties, optical properties, electrical conductivity, ferroelectricity, dielectricity and superpara-magnetism. The importance of each characteristic feature is depending on the field of application of the nanomaterial. The structural characterisation of nanomaterials is one of the most important assessments due to the high correlation between structure and already mentioned new physical phenomena. The structural characterisation includes the determination of the size distribution, the shape, the crystal structure and optionally a shell analysis if a surface functionalization has been done.

A suitable method for a fast determination of the size distribution of colloidal nanoparticle dispersions is the dynamic light scattering[119]. DLS is based upon the time and space correlation of the interference pattern induced by the scattering of a laser beam by small particles within a dispersion. The pattern originates from the spherical scattering of light on small particles and the interference of those spheres. The time correlation occurs due to the Brownian motion of the particles which is dependent on their inertia and of course on the viscosity of the solvent, the temperature and their size. If both other parameters are known, the size can be computed with an autocorrelation function[119]. Unfortunately, the resolution for the differentiation of more than one sized particle is rather low. Additionally, only the

hydrodynamic radius of a particle can be measured by DLS, i.e. the particle enveloped by a solvent shell would lead to a larger apparent particle size. Therefore, complementary techniques for the size and shape determination have to be used like scanning or transmission electron microscopy (SEM/TEM).

Normal optical microscopic techniques were limited by the wavelength of visible light for a long time. If the size of an object is considerably lower than the wavelength, it could not be depicted with the standard methods. Electron microscopy utilises the smaller wavelength of accelerated electrons for a superior resolution. In a scanning electron microscope, accelerated electrons range between 100 eV and 50 keV delivering a magnification of over 300000. If a sample is scanned with such a focused electron beam, the electrons penetrate the sample and undergo a number of interactions leading to the emission of photons and secondary electrons. The emitted electrons are collected and combined into an image of the probed sample. Additionally to the morphology of a probe, SEM also delivers information about the composition of the compounds characterised by the emission of X-rays and Auger electrons from the excited atoms and molecules enabling the energy-dispersive X-ray spectroscopy (EDX).

Another method to depict even smaller structures is TEM yielding point-to-point resolutions better than 0.2 nm.[114] In contrast to SEM, the electrons are accelerated further up to 100 keV leading to even smaller electron wavelength. Those electrons pass through most thin objects (<200 nm), due to their higher energies. A picture can be constructed from the inelastic scattering taking place at grain boundaries, defects, and density deviations leading to a spatial intensity loss of the electron beam. But the shortcoming of TEM is the limited depth resolution induced by the projection of a three-dimensional object onto a two-dimensional detector. On the other hand, the elastic scattering of electrons in a selected area produces an electron diffraction pattern which can be used for determination of the Bravais lattices of a single nanocrystal similar to XRD. This method is very time consuming due to problematic sample preparation and user interpretation of the lattice. Other diffraction methods are normally preferred for lattice determination like XRD or neutron diffraction.

Beside the physical properties like size, shape and crystal lattice, the surface is also of utmost importance considering the impact on nanoparticle behaviour and dispersion stability. The composition of the surface or shell of a nanomaterial can be assessed by XPS, the Auger electron spectroscopy and the secondary ion mass spectrometry while the stability of a liquid dispersion can be determined by measurement of the ζ-potential which represents the electronic repulsion of two adjacent particles.

However, whether all those analysis methods and the additionally available methods are necessary, is strongly depending on the field of application of the nanomaterial in question.

2. Aims of the thesis

A major problem of MRI is the quantitation of contrast enhancing compounds which are mainly based on the paramagnetic elements gadolinium and manganese. The results of this work shall aid to solve this quantitation issue of MRI by application of PET/SPECT suitable radionuclides. The scope of the present work is activation and authentic radiolabelling of MR contrast agents. The precise evaluation of the *in vivo* behaviour of new contrast agents (intake, distribution, accumulation, excretion) can be achieved non-invasively with one of the emission tomographic methods in humans. Additionally, the connected concept of multi-modal contrast agents opens up a new field of personalised medicine using the complete potential of PET/MRI hybrid scanners.

The first goal of this work is the identification of suitable radionuclides of gadolinium and manganese for PET or SPECT . This includes the discussion of β^+-emission probabilities, β^+-energies, half-lives and interfering γ-ray emission for the assessment if a radionuclide is suitable for PET. A similar discussion has to be done for the identification of radionuclides for SPECT. The most important parameter in case of SPECT is the high emission probability of γ-rays in the 100-300 keV range. Additionally, half-lives and interfering β^+-emissions have to be discussed.

The second goal is the production of the selected radionuclides. Nuclear reactions leading to those radionuclides have to be identified and assessed by cross section measurements, theoretical yield calculations and experimental yield measurements. Produced isotopic by-products have to be considered and, if possible, avoided by selection of an optimal energy range for isotopic pure production and eventually the use of enriched target materials. Other suitable nuclear reactions have to be compared in search of the most beneficial one.

The third goal is the separation of the produced radionuclide from the bulk of target material to enable the n.c.a. synthesis of a radiotracer. If no suitable separation is available from the literature, existing separations have to be adapted or new separations have to be developed to meet the current needs of the individual application.

The fourth goal is a proof of principle application of the produced radionuclides. In case of gadolinium, it is the authentic labelling of a commercial MRI agent. Due to the current, worldwide research on manganese based MR nanosized contrast agents, the authentic labelling of a nanoparticle precursor should also be investigated.

The fifth goal is the evaluation of an alternative tracing method of the nanosized contrast agents and their stability by activation experiments. Therefore, manganese nanoparticles have to be characterised after bombardment with neutrons and protons and their integrity and possible ion leaching have to be measured.

3. Experimental

3.1 Chemicals and analysis equipment

The chemicals used in this work, their properties and the respective suppliers are compiled in Table 4. If not mentioned otherwise materials were applied directly without further purification. The deionized water utilised in the experiments was HPLC-grade as a rule supplied by a purification plant (Purelab Classic, ELGA Labwater).

Table 4: List of chemicals, properties and supplier

Name	Formula	Properties	Supplier
acetic acid	$C_2H_4O_2$	purity >99.0 %	Sigma-Aldrich Co. LLC.
acetonitrile	C_2H_3N	purity 99.9 %	Honeywell Riedel-de Haën
acetyl acetone	$C_5H_8O_2$	purity >99 %	Sigma-Aldrich Co. LLC.
aluminium foil	Al	0.01 to 0.3 mm thickness; purity 99 %	Goodfellow GmbH
Amberlite CG-400-II	-	Cl^- form, 200 - 400 mesh	Fluka Chemie AG
Amberlite IR 120	-	H^+ form, 20 - 50 mesh	Merck KGaA
ammonium hydroxide solution	NH_4OH	25 wt%, pro analysis	Fluka Chemie AG
bis(2-ethylhexyl) phosphate (HDEHP)	$C_{16}H_{35}O_4P$	purity 97 %	Sigma-Aldrich Co. LLC.
butanol	$C_4H_{10}O$	purity 99.4 %	Sigma-Aldrich Co. LLC.
chromium plates	Cr	purity 99.9 %	Goodfellow GmbH
chromium(III) chloride hexahydrate	$CrCl_3 \cdot 6\ H_2O$	purity >98.0 %	Sigma-Aldrich Co. LLC.
copper foil	Cu	0.01 to 0.1 mm thickness; purity 99.9 %	Goodfellow GmbH
DGA normal	-	50-100 μm particle size	Triskem International

Table 4 cont.

Name	Formula	Properties	Supplier
1,4,7,10-tetraazacyclododecane-1,4,7,10-tetraacetic acid (DOTA)	$C_{16}H_{28}N_4O_8$	purity >97.0 %	Sigma-Aldrich Co. LLC.
ethanol	C_2H_6O	pro analysis	Sigma-Aldrich Co. LLC.
europium oxide	Eu_2O_3	purity 99.9 %	AlfaProducts
hydrochloric acid	HCl	>37 wt%, pro analysis	Sigma-Aldrich Co. LLC.
nickel foil	Ni	0.01 mm thickness; purity 99.95 %	Goodfellow GmbH
nitric acid	HNO_3	>69 wt%, pro analysis	Sigma-Aldrich Co. LLC.
manganese (II) acetate	$MnC_4H_6O_4$	purity 98 %	Sigma-Aldrich Co. LLC.
manganese (II) acetylacetonate	$MnC_{10}H_{14}O_4$	pro analysis	Sigma-Aldrich Co. LLC.
manganese (II) chloride tetrahydrate	$MnCl_2 \cdot 4\ H_2O$	purity >98 %	Sigma-Aldrich Co. LLC.
mercury	Hg	purity >99.99 %	Sigma-Aldrich Co. LLC.
methanol	CH_4O	pro analysis	Sigma-Aldrich Co. LLC.
oxalic acid	$C_2H_2O_4$	purity 98 %	Sigma-Aldrich Co. LLC.
phosphate buffered saline (PBS)	KH_2PO_4, NaCl, $Na_2HPO_4 \cdot 7\ H_2O$	pH 7.4	life technologies
polyvinylpyrrolidone (PVP)	$(C_6H_9NO)_x$	40.000 avg. molar weight	Sigma-Aldrich Co. LLC.
2-Propanol	C_3H_8O	purity 99.5 %	Merck KGaA

Table 4 cont.

Name	Formula	Properties	Supplier
sodium acetate	$NaC_2H_3O_2$	purity >99.0 %	Sigma-Aldrich Co. LLC.
sodium hydroxide	NaOH	pro analysis	Merck KGaA
sodium mercury amalgam	Na,Hg	20 wt% sodium content, purity >99.9 %	Sigma-Aldrich Co. LLC.
triethylene glycol	$C_6H_{14}O_4$	purity 99 %	Sigma-Aldrich Co. LLC.

The γ-ray measurements were conducted with five different ORTEC γ-ray spectrometers (AMETEK GmbH) which are listed in Table 5. They were efficiency and energy calibrated with the standard radiation point sources summarised in Table 6.

Table 5: List of characteristics of employed γ-ray spectrometers (AMETEK GmbH)

Detector model	GEM-18190-P	GEM-20190	GEM-20190	GEM 10P4-70
HV	459	459	660	659
MCA/ADC	919 E	919 E	919 E	919 Spectrum Master
amplifier	672	672	672	672
resolution (FWHM at 1.33 MeV, ^{60}Co)	1.70 keV	1.66 keV	1.68 keV	1.71 keV
relative efficiency at 1.33 MeV, ^{60}Co	19.1 %	24.5 %	30 %	10 %
peak-to-compton ratio, ^{60}Co	51 : 1	61 : 1	64 : 1	43 : 1

Table 6: List of standard radiation point sources employed

Nuclide	ID	Supplier
^{60}Co	LY369	Amersham
^{133}Ba	4081	Amersham
^{133}Ba	LY366	Amersham
^{137}Cs	430-78	Physikalisch-Technische Bundesanstalt (PTB)
^{152}Eu	371-83	PTB
^{152}Eu	412-76	PTB
^{152}Eu	440-88	PTB
^{226}Ra	404-84	PTB
^{226}Ra	DW539	Amersham
multi element: ^{241}Am, ^{57}Co, ^{60}Co, ^{109}Cr, ^{137}Cs	PK-151	PTB
multi element: ^{241}Am, ^{57}Co, ^{60}Co, ^{109}Cr, ^{137}Cs	PK-152	PTB
^{241}Am	430-78	PTB

Several techniques such as Dynamic-Light-Scattering (DLS) and Transmission Electron Microscopy (TEM) were utilised for a characterisation of synthesised and commercial nanoparticles. The DLS measurements were done with a Zetasizer Nano S (Malvern).
The instrument specifications for DLS measurements with a Zetasizer Nano S (Malvern) and TEM measurements with a LIBRA 120 (Zeiss) are listed in Table 7 and Table 8. Other special laboratory equipment used was a Biofuge Primo (Thermo Electron Fischer) centrifuge; a Discover (CEM) microwave oven; a DC scanner (Packard Instant Imager).

Table 7: Specifications of Zetasizer Nano S for DLS measurements

Parameter	Specification
Measurement range	0.3 nm – 10.0 µm (diameter).
Minimal sample volume	12 µl
Measurement error	+/-2 % for latex standards, traceable after NIST.
Light source	He-Ne-Laser, wave length: 633 nm, max. 4 mW.

Table 8: Specifications of the used LIBRA 120 for TEM measurements

Parameter	Specification
Electron Source	LiB_6-cristal
Acceleration Voltage	80 and 120 kV
Illumination System	Koehler illumination system
Objective Lenses	Truly symmetrical type
Resolution Point - Point	0.34 nm
Information Limit	<0.20 nm
STEM	<0.50 nm
Spectrometer	In-column OMEGA type
Dispersion	1.17 µm/eV @ 120 kV
Energy resolution	<1.5 eV
Imaging System	Magnification zoom for imaging, diffraction and spectroscopy with 5 imaging lenses and OMEGA spectrometer.
Magnification TEM STEM EELS	8 - 630,000x 50 - 1,000,000x 20 - 315x
System Control	WinTEM™ Graphical User Interface (GUI) with Windows®XP

3.2 Determination of nuclear reaction data for production of radio-gadolinium

As described in chapter 1.5.2 the two suitable candidates of gadolinium for SPECT imaging are ^{147}Gd and ^{149}Gd. Already available cross section data suggested higher production rates for deuteron and proton induced reactions on europium than those observed with the already established irradiation of enriched Sm isotopes with ^{3}He and ^{4}He by Denzler et al.[75]

The cross sections, integral yields and some thick target yields were experimentally and arithmetically determined to evaluate if the production is worthwhile using deuteron and proton induced reactions on europium.

3.2.1 Target preparation and stack assembly

In general, cross sections of nuclear reactions are highly dependent on the particle energy. The energy degradation of charged particles in matter is rather high in comparison with

uncharged particles. Therefore, the earlier mentioned stacked-foil technique[89] was utilised to obtain several cross sections of nuclear reactions at different particle energies from one irradiation. Such stacked-foil targets consisted of 50 – 300 μm thin Al foils for particle energy degradation, 10 – 20 μm thin Al, Cu and Ni foils serving as monitors for determination of particle energy and beam current, as well as several sediments of the actual target material Eu_2O_3. Alternating the thickness of the Al degraders in the stack assembly lead to slightly different effective projectile energies in the individual target samples during each irradiation. These results in interleaved particle energy sets of the different irradiations and produces a cross section data over a broad but fine meshed energy spectrum.

Due to this strong particle energy dependence, cross section determinations with charged particles are in need of thin cross section targets with a high homogeneity and well-defined elemental compositions to minimise the experimental uncertainty. This can be realised by using thin foils of the zero-valent oxidation state, i.e. the elemental metal, for many compounds. Unfortunately, elemental europium is one of the most reactive lanthanides. Already a contact with air at room temperature leads to oxidation which affects the area weight altogether with the energy degradation in the target noticeably. If heated to about 180 °C, elemental europium self-ignites in the presence of air forming Eu_2O_3. Thus, handling an elemental europium target would need to be done under strictly inert conditions, whereas use of trivalent europium as Eu_2O_3 does not require any special precautions. It occurs as fine, slightly hygroscopic white powder and can be used for preparation of sediment targets with high homogeneity and well-defined area weights.

The basic sedimentation technique used here was published by Rösch et al.[120] and was only adjusted in size to conform to the available target stations described below. Aluminium foils of 50 μm thickness and a diameter of 15 mm were used as sediment backings for a typical target for cross section measurements. This thickness was the optimal trade-off between a manageable stack assembly and additional interfering artefacts in the γ-spectrometric graphs from activation which is less in case of aluminium compared with other metals.

Before sedimentation took place, the aluminium backings were etched for 1 min in a bath of 6 M hydrochloric acid to increase adhesion of the sediments and cleaned thoroughly afterwards with pure water and 2-propanol. After weighing each foil three times, they were fixed in a Teflon sedimentation chamber with a volume of approx. 1.5 mL and an inner diameter of 13 mm. Europium oxide was then sedimented onto the aluminium foils from a finely dispersed ethanolic suspension. The thickness of sediments was carefully controlled by adjusting the concentration of europium oxide in the dispersion to achieve low energy degradation in the target, but still sufficient activities for measurement. The area mass density of a sediment was altered corresponding to its place in the stack from 0.0075 g/cm^2

at lowest particle energies to 0.015 g/cm^2 at the incident energy. After 2 to 4 h and nearly complete evaporation of ethanol the sediments were removed from the sedimentation chamber. The produced sediment discs were highly fragile and had to be handled with utmost care. If the evaporation time was too long, removal of discs from the sedimentation chamber was no longer possible as the sediments became too brittle and were destroyed in the process.

Afterwards, the sediment discs were kept in an oven at 100°C as long as possible to assure complete dryness. After at least 6 h of drying the sediments were weighed threefold and carefully covered with aluminium foils of 20 μm thickness and a diameter of 18 mm. Figure 8 shows different views of Eu_2O_3 sediments before and after wrapping. For storage, the sediments were kept in an oven at 100°C until the assembly of the stack took place.

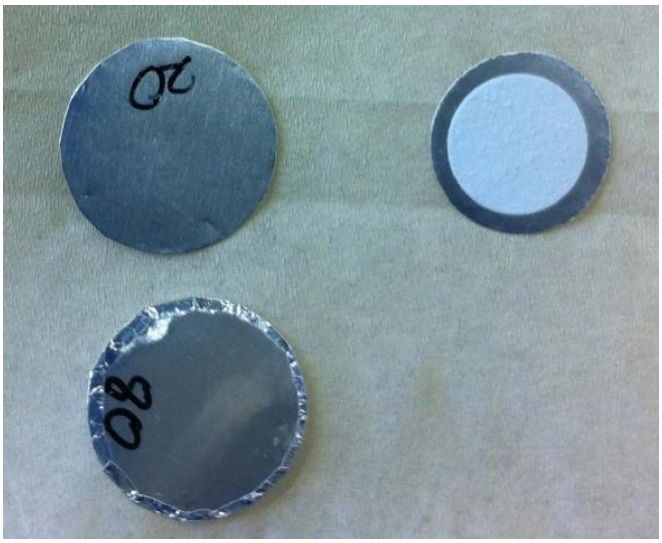

Figure 8: Uncovered (right) and covered (left) Eu_2O_3 sediment on 50 μm Al backing.

Thick target preparation

The sedimentation technique is limited by thickness. While very thin samples can be prepared with high quality, thick targets are very fragile and not fully homogeneous anymore. Considering this, thicker targets for measurement of the production rates and saturation yields were prepared differently. In this case europium oxide powder was pressed in a moulding (Supplier: ENERPAC) into pellets of varying thicknesses with a diameter of 10 mm. Application of 6.3 t/cm^2 (62.5 kN/cm^2) over 1-2 h was enough to produce pellets of sufficient stability and an area density of 1.01 g/cm^2 or 1.72 g/cm^2. The prepared pellets were dried in an oven for at least 6 h at 100°C before weighing. Afterwards they were completely wrapped in 10 μm thick copper foil on top of a 50 μm thick copper backing which was 13 mm in

diameter. Such prepared thick targets were stable enough to endure beam currents up to 0.5 μA without weight loss or visible physical change.

3.2.2 Irradiation facilities and irradiations

Two different target stations of the cyclotron JULIC were used for irradiations. The deuteron bombardments were all done at the internal target system while the proton bombardments took place at the new external target system depicted in Figure 9.

The schematics of the stacked-foil target support systems are shown in the lower right and upper left corner of Figure 10. In the internal target system, the deuteron beam was extracted with a stripper foil, guided through an aperture and directly let onto the target. The deuteron incident energy was 75.0 ± 0.4 MeV and the nominal beam current was 200 nA which was maintained for 4 h.

The prime advantage of the external target is the additional focusing of the particle beam with a quadrupole magnet in combination with a 4 sector aperture for the individual beam modulation in close proximity of the target. The simpler target handling, the improved cooling system, including a helium-gas cooled injector foil as well as a larger cooling area compared to the internal target system is furthermore more suitable for irradiating fragile targets or for irradiations with higher beam currents of up to 3 μA.

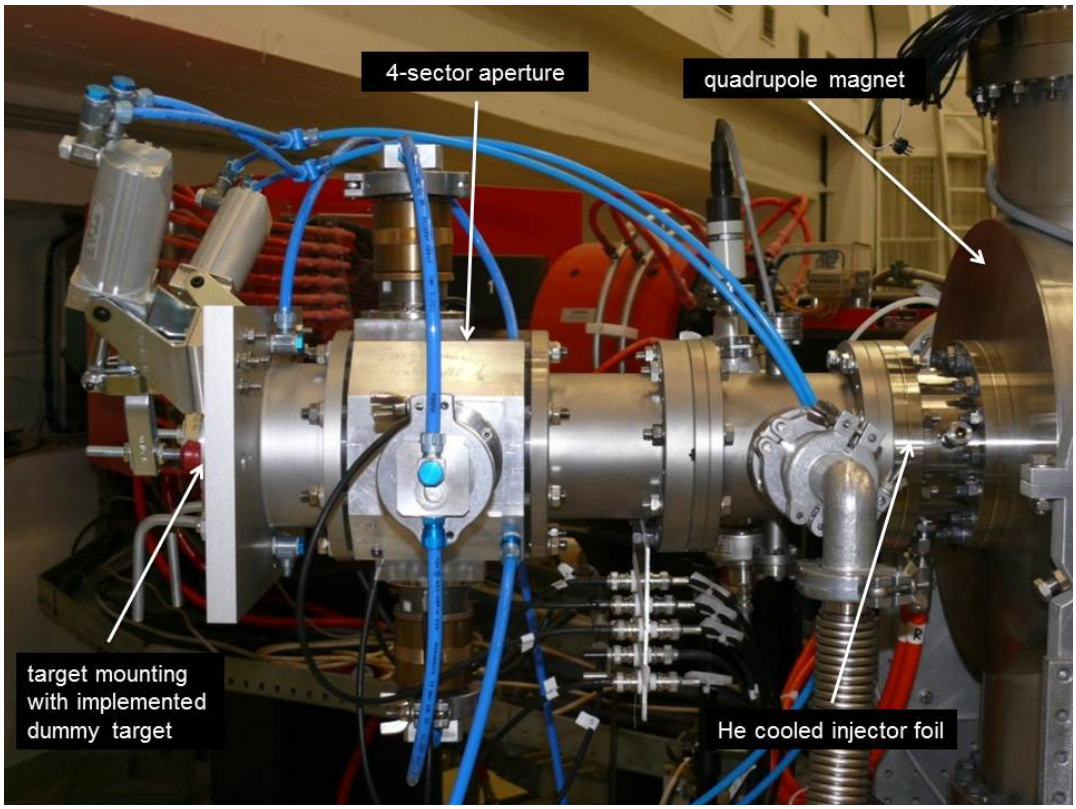

Figure 9: Picture of the external target system of cyclotron JULIC with 4 sector aperture, cooling and vacuum system.

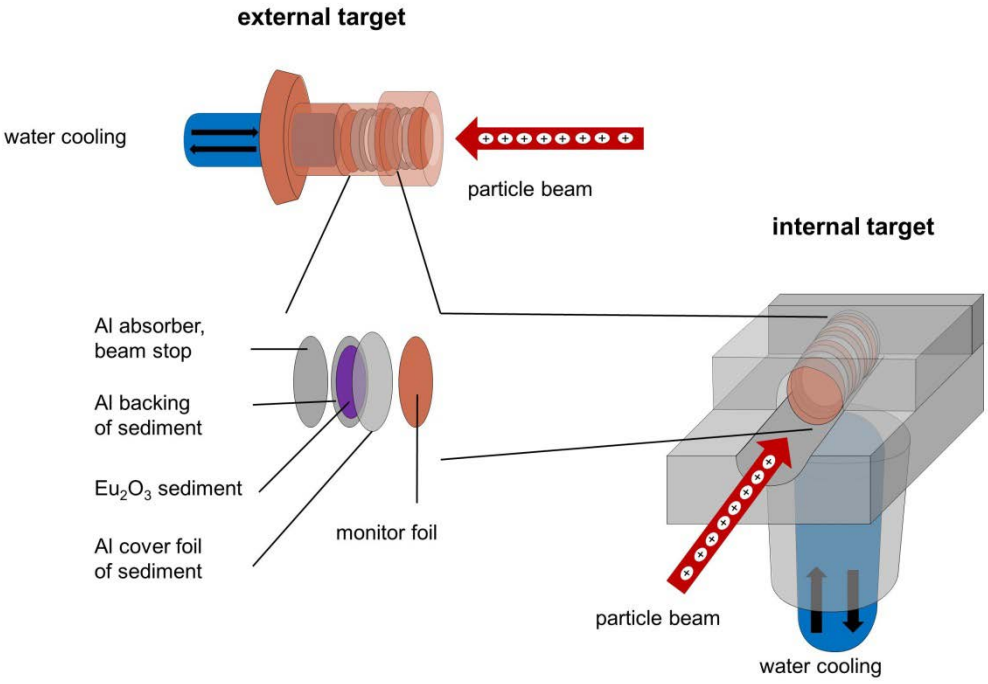

Figure 10: Scheme of the internal and external target system of the JULIC cyclotron as well as standard stack composition.

A further important point for introduction of the new target system was the problematic modulation of the proton beam which could not be sufficiently focused in the internal target system (see chapter 3.2.3). Therefore, proton cross section experiments were carried out at the external target system with proton incident energies of 45.1 ± 0.3 MeV and a nominal beam current of 200 nA over 2 h.

3.2.3 Beam profile, beam current and particle energy analysis

For the reliability of the experiments, and hence, reliability of the determined nuclear reaction data, several parameters had to be analyzed carefully for each irradiation. These were the final beam position, the beam spreading throughout the target, the particle energy degradation, and the beam current or particle flux density.

The final beam position and eventual spreading of the beam in the target were checked by measuring the first and last monitor foils with a DC scanner (Packard Instant Imager) after the irradiations. Due to the lack of a graphical overlay with a real time picture, the foils were placed on a target matrix consisting of two circles, whose physical dimensions (diameter: 16 and 20 mm) were marked with 4 dots of ^{22}Na each. The scanner revealed the activation profile of the monitor foils with the necessary spatial orientation from the target matrix (see Figure 11). Therewith the dimensions and the position of the beam spot could be assessed by investigating the activation profile of the monitor foils relative to the ^{22}Na spots.

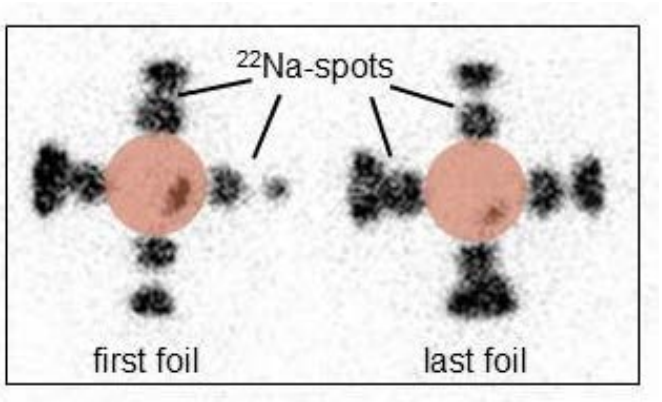

Figure 11: Beam position in a proton test irradiation at the internal target with a circular area of 15 mm in diameter to illustrate the monitor foil position and dimension.

While the nominal beam current can be easily determined by a faraday cup, the effective beam current on the target foils can be quite different due to beam absorption or spreading. Therefore, the actual beam current as well as the particle energy was experimentally determined from the already mentioned Al, Ni and Cu monitor foils in front of every Eu_2O_3 sediment target.

The general principle behind the use of those monitor foils is based on the evaluated nuclear monitor reactions, namely $^{nat}Al(d,x)^{22,24}Na$, $^{nat}Ni(p,x)^{57}Ni$, $^{nat}Cu(p,x)^{62,63,65}Zn$, and their well-defined excitation functions which are summarised and published in IAEA-TECDOC-1211[121]. If both the effective particle energies of the monitor foils within the target stack and the cross section of the respective monitor reactions are known, only a simple mathematical conversion of the above mentioned activation equation 6 is needed to calculate the beam flux or current:

$$\phi = \frac{A}{\sigma \cdot N \cdot (1 - e^{-\lambda t_{irr}}) \cdot e^{-\lambda t_{cool}}}$$

with: ϕ: particle flux density,

A: half-life corrected activity of the produced monitor nuclide at EOB,

σ: cross section of the monitor nuclide at the corresponding particle energy,

N: number of irradiated, inactive monitor atoms,

λ: decay constant of the produced monitor nuclide,

t_{irr}: irradiation time,

t_{cool}: time from the end of bombardment to the γ-ray measurement.

The calculation of the particle energy degradation which is needed for measurement of the beam current and for determination of the reaction cross section was realised with the Excel-routine STACK which is based on arithmetical calculations from Bethe and Bloch[122] with a

numerical adjustment from Williamson[123]. Additionally, the particle energy was experimentally determined by using the cross section ratio of two independent nuclear reactions. The theoretical calculated particle energies were used for planning of the cross section interleave between different irradiations beforehand and corrected with the experimentally determined particle energies afterwards. An example of the calculated energy degradation for the proton irradiation by STACK is shown in Table 9.

Table 9: STACK calculation of the proton irradiation of Eu_2O_3 sediment targets.

Projectile data		
Name	Proton number	Molar nass
	opr	upr
H	1	1.0079

Incident energy		
startener	precision	
45	100	

Legend
copper monitor foil
Eu_2O_3 sediment target
nickel monitor foil
aluminium absorber

	Target-Daten									
No.:	Target	Protons target	Mass	Weight	Diameter	Area density	Average energy	Incident energy	Exit energy	Energy absorption
			[g/mol]	[g]	[mm]	[g/cm^2]	[MeV]	[MeV]	[MeV]	[MeV]
1	Cu	29	63.546	0.041	15.0	2.319E-02	44.90	45.00	44.80	0.20
2	Eu	63	151.96	0.01367	13.0	1.030E-02	44.66	44.80	44.53	0.26
3	Al	13	26.982	0.04527	15.0	2.562E-02	44.40	44.53	44.26	0.27
4	Ni	28	58.7	0.03907	15.0	2.211E-02	44.16	44.26	44.05	0.21
5	Eu	63	151.96	0.01570	13.0	1.183E-02	43.91	44.05	43.77	0.28
6	Al	13	26.982	0.04553	15.0	2.576E-02	43.63	43.77	43.50	0.28
7	Al	13	26.982	0.04536	15.0	2.567E-02	43.36	43.50	43.22	0.28
8	Cu	29	63.546	0.0411	15.0	2.324E-02	43.11	43.22	43.01	0.21
9	Eu	63	151.96	0.01362	13.0	1.026E-02	42.87	43.01	42.74	0.27
10	Al	13	26.982	0.04565	15.0	2.583E-02	42.59	42.74	42.45	0.28
11	Al	13	26.982	0.04555	15.0	2.578E-02	42.31	42.45	42.17	0.28
12	Ni	28	58.7	0.03853	15.0	2.180E-02	42.06	42.17	41.96	0.21
13	Eu	63	151.96	0.01439	13.0	1.084E-02	41.81	41.96	41.67	0.28
14	Al	13	26.982	0.04554	15.0	2.577E-02	41.53	41.67	41.38	0.29
15	Cu	29	63.546	0.041	15.0	2.318E-02	41.28	41.38	41.17	0.22
16	Eu	63	151.96	0.01480	13.0	1.115E-02	41.02	41.17	40.88	0.29
17	Al	13	26.982	0.04553	15.0	2.576E-02	40.73	40.88	40.59	0.29
18	Al	13	26.982	0.04555	15.0	2.578E-02	40.44	40.59	40.29	0.29
19	Ni	28	58.7	0.03898	15.0	2.206E-02	40.18	40.29	40.07	0.22
20	Eu	63	151.96	0.01371	13.0	1.033E-02	39.93	40.07	39.78	0.29
21	Al	13	26.982	0.11962	15.0	6.769E-02	39.39	39.78	38.99	0.79
22	Al	13	26.982	0.11973	15.0	6.775E-02	38.59	38.99	38.19	0.80
23	Al	13	26.982	0.04543	15.0	2.571E-02	38.04	38.19	37.88	0.31
24	Cu	29	63.546	0.041	15.0	2.319E-02	37.77	37.88	37.65	0.23
25	Eu	63	151.96	0.01509	13.0	1.137E-02	37.50	37.65	37.34	0.31
26	Al	13	26.982	0.11990	15.0	6.785E-02	36.92	37.34	36.51	0.83
27	Al	13	26.982	0.11975	15.0	6.776E-02	36.09	36.51	35.66	0.85
28	Al	13	26.982	0.04538	15.0	2.568E-02	35.50	35.66	35.34	0.32
29	Ni	28	58.7	0.03902	15.0	2.208E-02	35.22	35.34	35.09	0.25
30	Eu	63	151.96	0.01554	13.0	1.171E-02	34.93	35.09	34.76	0.33
31	Al	13	26.982	0.11992	15.0	6.786E-02	34.32	34.76	33.88	0.88
32	Al	13	26.982	0.11964	15.0	6.770E-02	33.43	33.88	32.99	0.90
33	Cu	29	63.546	0.041	15.0	2.320E-02	32.86	32.99	32.73	0.26
34	Eu	63	151.96	0.01398	13.0	1.053E-02	32.56	32.73	32.39	0.34
35	Al	13	26.982	0.11990	15.0	6.785E-02	31.92	32.39	31.46	0.93
36	Al	13	26.982	0.11990	15.0	6.785E-02	30.98	31.46	30.51	0.95
37	Ni	28	58.7	0.04004	15.0	2.266E-02	30.37	30.51	30.23	0.28
38	Eu	63	151.96	0.01650	13.0	1.243E-02	30.05	30.23	29.88	0.34
39	Al	13	26.982	0.11990	15.0	6.785E-02	29.39	29.88	28.89	0.99
40	Al	13	26.982	0.04549	15.0	2.574E-02	28.70	28.89	28.51	0.38
41	Al	13	26.982	0.04544	15.0	2.571E-02	28.31	28.51	28.12	0.39
42	Cu	29	63.546	0.0425	15.0	2.403E-02	27.97	28.12	27.82	0.30
43	Eu	63	151.96	0.01596	13.0	1.202E-02	27.64	27.82	27.46	0.36
44	Al	13	26.982	0.11990	15.0	6.785E-02	26.93	27.46	26.39	1.06
45	Al	13	26.982	0.04542	15.0	2.570E-02	26.19	26.39	25.98	0.41
46	Al	13	26.982	0.04545	15.0	2.572E-02	25.77	25.98	25.57	0.42
47	Ni	28	58.7	0.03894	15.0	2.203E-02	25.41	25.57	25.25	0.31
48	Eu	63	151.96	0.01362	13.0	1.026E-02	25.07	25.25	24.88	0.37
49	Al	13	26.982	0.11990	15.0	6.785E-02	24.31	24.88	23.73	1.15
50	Al	13	26.982	0.04543	15.0	2.571E-02	23.51	23.73	23.28	0.45
51	Cu	29	63.546	0.041	15.0	2.321E-02	23.11	23.28	22.95	0.34
52	Eu	63	151.96	0.01265	13.0	9.532E-03	22.75	22.95	22.56	0.39

The disadvantage of the STACK software is its inability to calculate the energy degradation of chemical compounds like europium oxide directly. The routine is only designed to iterate the degradation in elemental materials, hence, for calculation in a compound the composing elements have to be handled separately. It was possible to simulate a homogenous compound by adding up the degradation of nearly infinitesimal thin layers of the alternating elements (see Table 10).

Table 10: STACK calculation of Eu_2O_3 sediments for layer simulation.

Projectile data		
Name	Proton number	Molar nass
	opr	upr
H	1	1.0079

Incident energy		No. of foils
startenergy	precision	
44.87	100	

	Target-Daten										
No.:	Target	protons target	Mass	Weight	Diameter	Description	Area density	average energy	incident energy	Exit energy	Energy absorption
		otrg	[g/mol] utrg	[g] weight	[mm] dfolie		[g/cm^2] flweight	[MeV]	[MeV] energy_in	[MeV] energy_out	[MeV]
1	Al	13	26.98154	0.00726	18.0	cover foil	2.853E-03	44.86	44.87	44.84	0.03
1	Eu	63	151.96	0.00137	13.0	sim layer 1	1.030E-03	44.84	44.84	44.83	0.01
2	O	8	15.9994	0.00022	13.0		1.626E-04	44.83	44.83	44.83	0.00
4	Eu	63	151.96	0.00137	13.0	sim layer 2	1.030E-03	44.83	44.83	44.82	0.01
5	O	8	15.9994	0.00022	13.0		1.626E-04	44.82	44.82	44.82	0.00
6	Eu	63	151.96	0.00137	13.0	sim layer 3	1.030E-03	44.82	44.82	44.82	0.01
8	O	8	15.9994	0.00022	13.0		1.626E-04	44.81	44.82	44.81	0.00
9	Eu	63	151.96	0.00137	13.0	sim layer 4	1.030E-03	44.81	44.81	44.81	0.01
10	O	8	15.9994	0.00022	13.0		1.626E-04	44.81	44.81	44.80	0.00
11	Eu	63	151.96	0.00137	13.0	sim layer 5	1.030E-03	44.80	44.80	44.80	0.01
12	O	8	15.9994	0.00022	13.0		1.626E-04	44.80	44.80	44.80	0.00
13	Eu	63	151.96	0.00137	13.0	sim layer 6	1.030E-03	44.79	44.80	44.79	0.01
14	O	8	15.9994	0.00022	13.0		1.626E-04	44.79	44.79	44.79	0.00
15	Eu	63	151.96	0.00137	13.0	sim layer 7	1.030E-03	44.78	44.79	44.78	0.01
16	O	8	15.9994	0.00022	13.0		1.626E-04	44.78	44.78	44.78	0.00
17	Eu	63	151.96	0.00137	13.0	sim layer 8	1.030E-03	44.77	44.78	44.77	0.01
18	O	8	15.9994	0.00022	13.0		1.626E-04	44.77	44.77	44.77	0.00
19	Eu	63	151.96	0.00137	13.0	sim layer 9	1.030E-03	44.76	44.77	44.76	0.01
20	O	8	15.9994	0.00022	13.0		1.626E-04	44.76	44.76	44.76	0.00
21	Eu	63	151.96	0.00137	13.0	sim layer 10	1.030E-03	44.76	44.76	44.75	0.01
22	O	8	15.9994	0.00022	13.0		1.626E-04	44.75	44.75	44.75	0.00
23	Al	13	26.98154	0.02353	15.0	backing	1.332E-02	44.68	44.75	44.61	0.14
										sum	0.09

The mass of the corresponding layers was calculated by formula 10:

$$m_{Eu/O} = \frac{m_{sediment} \cdot M_{part}}{l \cdot M_{Eu_2O_3}}$$

with $m_{Eu/O}$: mass of corresponding element in one simulated layer,

$m_{sediment}$: mass of the complete sediment,

M_{part}: molar weight part of Eu / O in Eu_2O_3,

l: number of layers,

$M_{Eu_2O_3}$: molar mass of Eu_2O_3.

Two nuclear reactions induced in the same monitor foil are needed for the experimental determination of the particle energy.[124] The particle energy was therefore determined independently of the beam current and particle flux density by calculating the cross section ratios of the $^{nat}Al(d,x)^{22,24}Na$ reactions and the $^{nat}Cu(p,x)^{62,63}Zn$ reactions known from literature[121]. In Figure 12 these calculated ratios are plotted against the corresponding particle energy for the deuteron and proton induced reactions.

A unique particle energy to cross section ratio assignment was achieved by dividing the energy range into subsets and fitting each subset with precise functions using the software TableCurve 2D. The fitted functions were used to determine the particle energy in each monitor foil as the calculated cross section ratio is equivalent to the experimentally measured activity ratio at the end of bombardment (EOB).

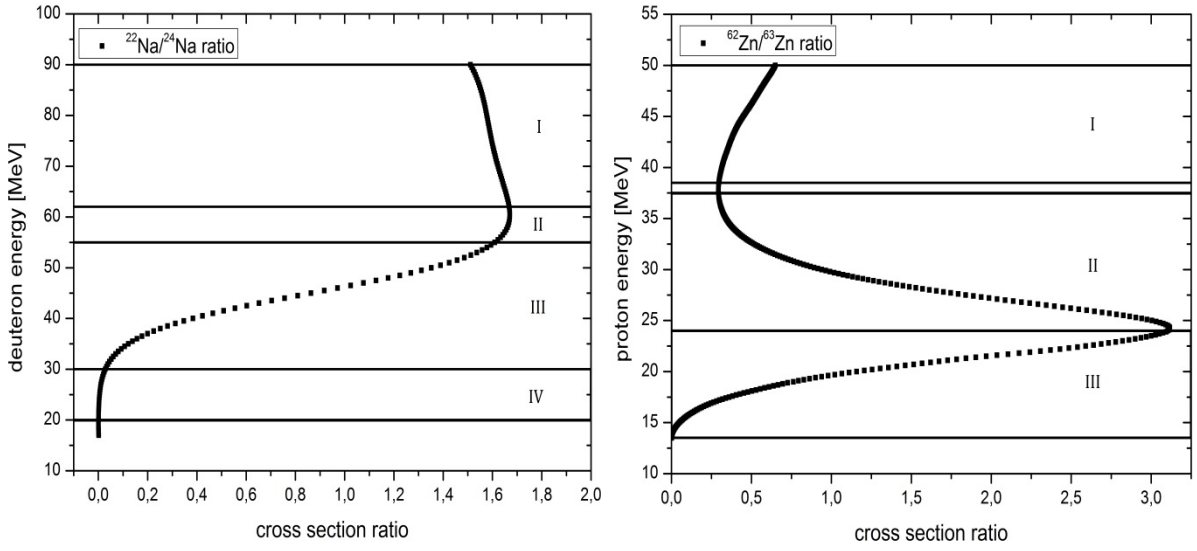

Figure 12: Cross section ratio of deuteron induced $^{27}Al(d,x)^{22,24}Na$ (left) and proton induced $^{nat}Cu(p,xn)^{62,63}Zn$ (right) nuclear reactions derived from the recommended data of the data collection IAEA-TECDOC-1211[121].

The incident energy as well as the degradation throughout the stacks derived from the STACK software was checked and eventually corrected this way. The monitor foils were measured twice with γ-ray spectrometers: One short measurement directly after irradiation and one extended measurement for long-lived monitor nuclides, i.e. ^{22}Na and ^{65}Zn. Activities were calculated using γ-ray intensities given by IAEA-TECDOC-1211[121], even if they deviated from most recently published γ-ray data[60] (see Table 11). This was done to maintain the internal integrity between the recommended and our measured data. Unfortunately, no other recommended cross section data of monitor reactions suitable for the experimental particle energy determination will be available in literature until the next revised version of IAEA-TECDOC-1211 is published.

Table 11: Half-lives, γ-ray energies and intensities of used monitor radionuclides from the electronic version of IAEA-TECDOC[121] and ENSDF[60].

Isotope	Half-life	γ-ray [keV] (intensity [%]) IAEA-TECDOC	γ-ray [keV] (intensity [%]) ENSDF
^{22}Na	2.602 a	1274.5 (99.94)	1274.6 (99.94)
^{24}Na	14.650 h	1368.6 (100)	1368.6 (99.99)
^{57}Ni	35.60 h	127.2 (12.9)	127.2 (16.67)
		1377.6 (77.9)	1377.6 (81.7)
^{62}Zn	9.193 h	548.4 (15.2)	548.4 (15.34)
		596.7 (25.7)	596.6 (26.0)
^{63}Zn	38.47 min	669.8 (8.4)	669.6 (8.2)
		962.2 (6.6)	962.0 (6.48)
^{65}Zn	244.26 d	1115.5 (50.75)	1115.5 (50.04)

3.2.4 Cross section measurements and calculations

Due to high dose rates after irradiation of the target stacks some cool down time of at least 1 h was allowed after EOB for the decay of short-lived activation by-products, such as ^{13}N and ^{15}O, produced by ^{nat}O(p,x) or ^{nat}O(d,x) reactions, before first measurements took place. Non-destructive measurements of all targets were done after separating the monitor foils and sediments. Samples were measured several times with different time intervals after the EOB using γ-ray spectrometers for a quantitative registration of the radioactivity. Thereby, measurements of both shorter- (^{147,149}Gd) and longer-lived (^{146,151,153}Gd) radioisotopes were appropriately performed over the investigated energy range. Every investigated radionuclide possesses at least two separate γ-ray energies (see Table 2) which were both used for identification and determination of absolute radioactivity at EOB. The decay rates were individually calculated from the photo peak areas for each γ-ray by equation 11[125]:

$$A_{uncorr} = \frac{C}{t_{life} \cdot \varepsilon \cdot ep}$$

with A_{uncorr}: decay rate of a radionuclide specific γ-ray without half-life correction in decays/s,

C: counting events in a photo peak of a γ-ray integrated by a Gaussian bell curve with baseline correction,

t_{life}: active measurement time of the γ-ray detector corrected for dead time in sec,

ε: efficiency of the detector at given distance and geometry,

ep: emission probability of the specific γ-ray.

This decay rate had to be corrected for the decay occurring during the time of measurement (eq. 12)[125] as well as the time elapsed since EOB (eq. 13)[125]:

$$A_{begin\ measurement} = \frac{A_{uncorr} \cdot \lambda \cdot t_{real}}{(1 - e^{-\lambda \cdot t_{real}})}$$

$$A_{corr\ EOB} = A_{begin\ measurement} \cdot e^{\lambda \cdot t_{real}}$$

with $A_{begin\ measurement}$: corrected activity at the starting time of the measurement,

t_{real}: real time elapsed during measurement,

λ: decay constant of corresponding radionuclide,

$A_{corr\ EOB}$: corrected activity at the end of bombardment.

This resulted in the absolute activity A_{corr} of the produced radionuclides at the EOB. Cross sections were subsequently calculated with these absolute activities and the experimentally determined beam current using the converted activation equation 14[80]:

$$\sigma = \frac{A_{corr\ EOB} \cdot M}{\phi \cdot ad \cdot N_A} \cdot 10^{28}$$

with: σ: cross section of the monitor nuclide at the given particle energy in barn,

$A_{corr\ EOB}$: absolute activity of the corresponding radionuclide at EOB in Bq,

M: molar mass of the target nuclei in gram/mol,

ϕ: particle flux density in particles/cm^2,

ad: area density of the target g/cm^2,

N_A: Avogadro's constant.

3.2.5 Integral and experimental thick target yield measurements and calculations

The radionuclide production yields from proton induced reactions on elemental Eu were determined experimentally as well as calculated by the integral yield approach. For the latter, increments of 1 MeV projectile energy degradation were chosen for the compilation. The respective area densities needed for this energy degradation of 1 MeV were calculated up to the incident particle energy with STACK. Additionally, excitation functions were derived from the measured cross sections by iterating curve trend with the program TableCurve 2D (see Figure 13).

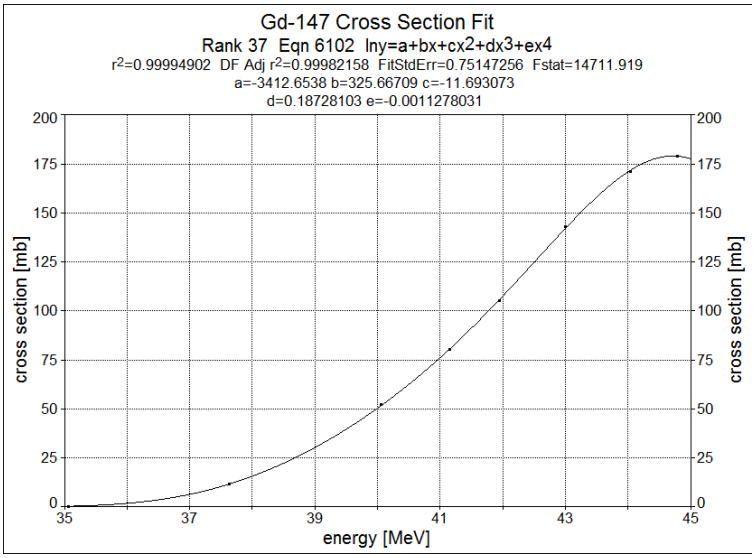

Figure 13: Iterated curve progression by the program TableCurve 2D for the determination of the excitation function of $^{nat}Eu(p,xn)^{147}Gd$.

Based on the derived cross section values for each energy increment and the corresponding area density, the radioactivity produced in the chosen 1 MeV intervals was calculated using the activation equation. The integral production rates per hour ($IntY_{prod}$) and the integral saturation yields ($IntY_{sat}$) described in equation 15 were calculated by integrating the produced activity over all intervals.

$$IntY_{prod/sat} = \sum_{E=min}^{E=max} \frac{\frac{m_E}{M} \cdot N_A \cdot \sigma_E \cdot \left(1 - e^{-\lambda t_{prod/sat}}\right)}{1\mu A}$$

with *E = max*: maximal available projectile energy of measured cross sections,
E = thrs: minimal available projectile energy of measured cross sections,
m_e: *mass of corresponding increment,*
$t_{prod/sat}$: 1 h / 10 times half-life of the corresponding nuclide in sec.

The experimental thick target yields were determined by irradiating targets of Eu_2O_3-pellets with a diameter of 10 mm and area densities of 1.01 or 1.72 g/cm^2. The area densities were chosen to include the complete production of ^{147}Gd in the higher and to cover the first maximum of the ^{149}Gd excitation function in the lower energy range.

A non-destructive measurement of the irradiated Eu_2O_3-pellet was not possible because of the large amount of produced radioactivity in the pellets. Therefore, irradiated pellets were completely dissolved in 3 - 4 mL 6 M hydrochloric acid overnight. Afterwards two 100 µl aliquots were prepared in 1.5 mL Eppendorf vials to assure near point-source geometry for γ-ray spectroscopy. The γ-ray measurements were conducted as described above. The whole procedure is illustrated in Figure 14.

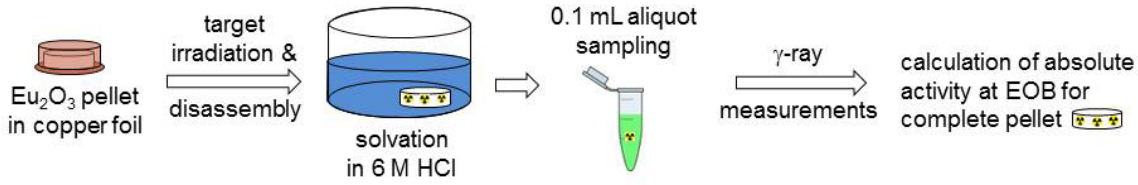

Figure 14: Partial measurement technique for highly radioactive Eu_2O_3 targets.

The incident and exit energy in the target as well as the respective beam current were confirmed via the monitor reactions $^{nat}Cu(p,x)^{62,63}Zn$ as described in chapter 3.2.3. Thereafter, the production rates per hour (TTY_{prod}) and the saturation yields (TTY_{sat}) were arithmetically obtained by equation 16:

$$TTY_{prod/sat} = \frac{A_{corr\ EOB} \cdot \left(1 - e^{-\lambda \cdot t_{prod/sat}}\right)}{I \cdot \left(1 - e^{-\lambda \cdot t_{irr}}\right)}$$

with $A_{corr\ EOB}$: corrected activity at EOB in Bq,

λ: decay constant of the corresponding nuclide in 1/sec,

$t_{prod/sat}$: 1 h / 10 times half-life of the corresponding nuclide in sec,

I: charged particle induced current in μA,

t_{irr}: irradiation time in sec.

3.3 Separation of n.c.a $^{147/149}$Gd from bulk ^{nat}Eu with a Na-Hg amalgam extraction

A macroscopic separation method for the removal of the bulk europium target material was tested and optimised. The separation of samarium and n.c.a europium from gadolinium was previously developed by Malan and Munzel[108] and later on successfully used by Denzler et al.[78]. An adaptation of the procedure of Malan and Munzel was used to separate europium from gadolinium by Lebedev et al.[77]. For a nearly quantitative removal of europium from n.c.a. radiogadolinium the separation had to be adapted and optimised. Therefore systematic studies were conducted and new optimised separation parameters determined.

The separation apparatus of Denzler et al. was adapted with slight modifications and is shown in Figure 15. The separations were assessed with a self-synthesised ^{149}Gd stock-solution to which inactive Europium was added in order to achieve target-like conditions. For the preparation of the ^{149}Gd solution Eu_2O_3-pellets with area densities of 0.83 g/cm^2 and a diameter of 13 mm were irradiated at the cyclotron JULIC for 2 - 3 h with a nominal beam current of 1 μA. The targets were dissolved overnight in 4 mL 6 M hydrochloric acid. An inactive Eu^{3+} solution (25 wt%) was prepared by dissolving Eu_2O_3 powder in 6 M hydrochloric acid within 5 min. The solution for aqueous separation was prepared by mixing appropriate

amounts of the $^{149}Gd/^{147}Eu$ solution and of the europium stock-solution (20 wt% Eu_2O_3), heating it to dryness and re-dissolving the white, solid residue in 25 mL of a 1 M saline solution buffered with 0.4 M sodium acetate. Afterwards the pH of the solution was adjusted to 2 – 3 using 0.5-0.8 mL concentrated hydrochloric acid.

Sodium mercury amalgam with 20 wt% of sodium was obtained from Sigma-Aldrich Co. The solid amalgam was diluted with elemental mercury in a small glove box under inert atmosphere yielding a liquid amalgam with 0.4 wt% sodium content. The diluted amalgam was stable for some weeks, when it was covered by dry ethanol under inert atmosphere in a tightly sealed glass bottle. The saline solution was added into the separation funnel first and the amalgam added directly afterwards.

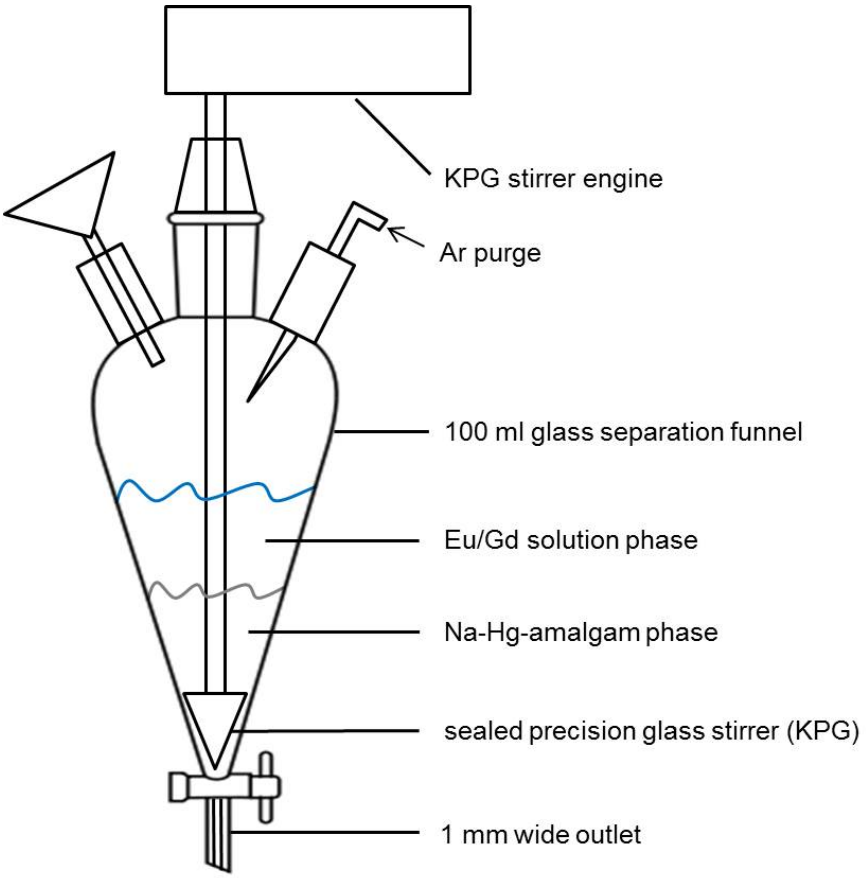

Figure 15: Extraction apparatus, adapted from Denzler et al.[78].

Three main separation parameters were systematically studied: The influence of europium mass, the sodium mercury amalgam mass, and the influence of the separation time. The europium mass was stepwise increased from 50 to 500 mg. The amount of amalgam was also stepwise increased from 5 to 10 mL with 500 mg europium present at the beginning of the separations. The time dependence of extraction was determined over 30 min with 500 mg europium and 10 mL amalgam.

In the assessment of the influence of europium and amalgam mass on the extraction, the residual ^{149}Gd and ^{147}Eu in solution were analysed by γ-spectrometric measurements of 1 mL aliquots before and after the separation. In order to measure the progress of the separation after different time intervals an on-line sampling of 0.5 mL aliquots with subsequent γ-spectrometric measurement was done over the course of the separation. ICP-MS analysis was utilised complementary to the γ-spectrometry for low europium concentrations.
The separations can be compared by calculation of the distribution coefficients as described in eq. 7 with the stationary phase corresponding to the amalgam phase and the mobile phase corresponding to the aqueous solution.

3.4 Preparation of $^{147/149}$Gd-DOTA and biodistribution measurements *in* and *ex vivo* on rats

As a proof of principle the applicability of $^{147/149}$Gd for authentic labelling of MRI contrast agents was tested with the already existing and FDA approved 1,4,7,10-tetraazacyclododecane-1,4,7,10-tetraacetic acid (DOTA) ligand as complexing agent. For this labelling $^{147/149}$Gd was separated from the irradiated bulk of target material Eu_2O_3, the complex was synthesised, the complex stability was measured under varying conditions, and the labelled compound injected into a tumour bearing rat.

3.4.1 Separation of $^{147/149}$Gd from Eu_2O_3

A 500 mg pellet of natural europium oxide was prepared as described above and irradiated at the cyclotron JULIC for 3 h with a beam current of 2 μA. The pellet was dissolved in 4 mL 6 M hydrochloric acid and evaporated to dryness. The newly determined optimal experimental parameters of the sodium-mercury amalgam separation described in detail in chapters 3.3 and 4.2 were used for the preparation of n.c.a. $^{147/149}$Gd with trace amounts of Eu. Therefore, the white residue was dissolved in 25 mL of a 1 M NaCl solution buffered with 0.4 M NaOAc. The solution was adjusted to a pH of 2, purged with Ar in an ultrasonic bath for 15 min and added to the separation funnel which was already flooded with Ar. After an additional 5 min Ar purge of the solution, 10 mL Na-Hg amalgam was weighed and added rapidly into the funnel. The binary mixture was intensely stirred for 20 min while a steady stream of Ar was bubbled through the solution.
From the resulting solution sodium acetate and sodium chloride (ca. 0.7 g) were removed with the extraction resin DGA normal. A column was prepared by packing 0.4 g previously soaked and sonicated DGA normal resin under 3 bar pressure into a column with a diameter of 0.5 cm. The separation solution was acidified with 65 % nitric acid to a 1 M nitric acid

concentration. The residual traces of europium and radioactive gadolinium were quantitatively bound on the DGA normal resin in 1 M nitric acid and eluted with approx. 25 mL of 0.1 M hydrochloric acid with a flow speed of 2 mL/min. The resulting fractions were evaporated to dryness, and the residues were dissolved in 2 mL of H_2O. The europium content was determined by ICP-MS.

3.4.2 $^{147/149}$Gd-DOTA complex synthesis and stability tests

Two approaches for the formation of the DOTA complex with Sc or Gd known from literature were tested for the n.c.a and c.a. synthesis of $^{147/149/nat}$Gd-DOTA.[126, 127].

In the first method, 100 μL of the stock-solution was added to 0.5 mL of a 0.1 M sodium acetate puffer solution with 30 mg DOTA ligand dissolved. The pH of the solution was adjusted with 1 M sodium hydroxide solution to 5.0 and the solution stirred at 40°C for 24 h. Then the solution was analysed with a radio thin layer chromatographic (TLC) system adapted from Huclier-Markai et al.[127]. The mobile phase consisted of a 2:1:1 volume mixture of NH_4OH(25 %):MeOH:H_2O and the stationary phase of silica gel with a manganese activated zinc oxide as fluorescence indicator. After an exposure time of 30 – 45 min the thin layer plate was measured in an Instant imager. Free ionic Gd^{3+} showed a retention factor of R_f = 0 and Gd-DOTA of R_f = 1.

In the second method, 100 μL of the stock-solution was added to 0.5 mL of a 1 M sodium acetate puffer solution with 5 mg dissolved DOTA ligand. The carrier added synthesis was tested with the same method by addition of 0.19 mg (0.1 eq) inactive Gd^{3+} carrier to the starting solution. Both mixtures were heated to 90°C for 20 min. After 5 min and 20 min radio-TLC was performed as described above.

The stability tests were conducted with the n.c.a as well as the c.a. Gd-DOTA complex. For this, 10 μL of the Gd-DOTA complex solution was added to 0.5 mL of a PBS puffer system. The solution was stirred for 24 h at 40°C and then analysed by radio TLC. The procedure was repeated with 0.5 mL human blood serum (HBS) by addition of 10 μL c.a. or n.c.a. Gd-DOTA solution and shaking for 56 h and also 144 h at 37°C in a ThermoMixer (Eppendorf). The analysis method had to be slightly adapted for HBS. The protein content of the HBS had to be denaturated with 1 mL of acetonitrile. The suspension was centrifuged to separate the clear liquid which was then used for radio TLC with the parameters described above.

3.4.3 *In* and *ex vivo* imaging of the $^{147/149}$Gd-DOTA complex

The previously described complex was injected into F98 glioma bearing male Wistar rats by colleagues at the Institute of Neuroscience and Medicine, INM-4: Medical Imaging Physics,

but are mentioned here for complete description of all experiments done. For comparison the rats were first injected with inactive DOTArem™ and measured in a 3T MRI camera and afterwards injected with the radioactive ^{nat}Eu/^{147,149}Gd cocktail. The tumour was measured by autoradiographic methods. The experiments were done once with an n.c.a. and once with a c.a. preparation of ^{147,149}Gd-DOTA.

The n.c.a experiment was conducted 8 days and the c.a. experiment 2 weeks post implantation of the glioma. In both experiments 0.3 mmol/kg of the commercial contrast agent was injected intravenously and T_2-weighted SPC Inversion Recovery (similar to clinical "FLAIR – Fluid Attenuated Inversion Recovery"[128]) measurements as well as T_1-weighted Magnetization Prepared Rapid Gradient Echo (MP-RAGE)[128] before and after the application of contrast agent were done.

The *ex vivo* imaging was done with the ^{147,149}Gd-DOTA complex synthesised at 90°C in 0.5 mL of a 0.1 M sodium acetate puffer solution. After the synthesis the pH of the solution was adjusted to 7 with 1 M sodium hydroxide solution. In the experiment without carrier approx. 30 MBq of n.c.a. ^{149}Gd-DOTA in 1 mL solution was injected into the rat intravenously. In the carrier added experiment, approx. 40 MBq of a 1:1 mixture of $^{147/149}$Gd-DOTA in 0.6 mL solution was mixed with 0.2 mL commercial available DOTArem™ to simulate carrier added conditions similar to the previous contrast enhanced MRI measurement. The mixture was also injected intravenously into a tumour bearing rat. For the *ex vivo* measurements the rat was sacrificed 10 min later and dissected. The rat's brain was cut into 30 μm thick cryosections and the radioactivity measured by a cellulose acetate covered film (FUJI BAS-IP MS) for ca. 15 h. A histological staining with the DNA fluorescent stain 4',6-diamidino-2-phenylindole (DAPI) of the adjacent sections was concluded for comparison.

3.5 Production of n.c.a. manganese-52g

In a previous study[129] the proton induced reactions on natural chromium leading to radiomanganese and its separation from the bulk of target material were examined. For a better assessment of the production capabilities the thick target and integral yields had to be determined. Also, the isolation of the radionuclide had to be optimised because of the necessary complete removal of chloride ions.

3.5.1 Integral and experimental thick target yields of radiomanganese

For measurements of thick target yields and the development of an isolation of ^{52g}Mn from the target material ^{nat}Cr, circular targets (thickness: 1 mm, diameter: 13 mm) were wire eroded from cast disks of ^{nat}Cr (Goodfellow Ltd., purity 99.9 %).

Stacks of one cast chromium plate, copper monitor foils (10 μm thickness) and a copper beam stop for adequate thermal conductivity were irradiated at the Baby Cyclotron BC1710 to measure experimental production rates and to determine saturated thick target yields. The irradiations were done with a beam current of 1 μA for 1 minute.

The thick target yield over the proton energy range of 16.9 MeV to 8.2 MeV was experimentally determined to cover the full excitation function maximum of the nuclear reactions $^{nat}Cr(p,x)^{52g,m}Mn$ (see Figure 4). The targets were repeatedly measured non-destructively with a γ-ray spectrometer, beginning approx. 60 min (three half-lives of ^{52m}Mn) after EOB. The production rates for a one hour irradiation as well as the saturation thick target yields were calculated by equation 16. The theoretical integral yields were calculated with the previously measured excitation functions[65] using the same approach described above in chapter 3.2.5. The results of calculations were compared with the experimental values.

3.5.2 Development of a radiochemical separation of ^{52g}Mn and Cr

^{52g}Mn was produced for development of a radiochemical separation method by irradiation of cast chromium disks with protons in the energy range of 16.9 → 8.2 MeV.

First, a separation procedure of ^{54}Mn and ^{nat}Cr found in literature[130] was tested for its applicability. The Cr target was therefore dissolved in conc. HCl, the solution evaporated to dryness and the residue dissolved in 5 mL 5 % oxalic acid. This solution was again evaporated to dryness and the residue re-dissolved in 50 mL of 5 % oxalic acid. This solution was loaded onto an Amberlite IR-120 column 1 cm in diameter and 2 cm long which was prewashed with ten column volumes of 5 % oxalic acid. The column was washed with 5 % oxalic acid for Cr elution. HPLC-grade pure water was passed through the column and afterwards the residual radioactivity eluted with 1M HCl. Stepwise several parameters of the separation were optimised which are discussed in chapter 4.4.2.

The optimisation experiments of the known separation yielded no good results and the development of a new separation procedure was conducted by a two-step approach. At first a screening of distribution coefficients regarding an anion (Amberlite CG400™) and a cation exchange resin (DOWEX 50WX8™) with different eluents was performed searching a separation system. Secondly, eluents with promising distribution coefficients were used in chromatographic separations, and their capability evaluated to isolate ^{52g}Mn.

For measurement of the distribution coefficients, the resins were dried in an oven overnight and 50-100 mg of it was weighted into a 2 mL Eppendorf reaction vial. The resins were conditioned with 1.5 mL of the eluents by joggling the mixture with a vortex shaker (Vortex-Genie 2, Scientific Industries) for at least 24 h. 50 μL of a radioactive mixture consisting of

^{52g}Mn, ^{51}Cr and non-radioactive chromium were then injected into the resin-eluent mixtures. Additionally, reference samples were prepared by diluting 50 μL of the same radioactive mixture with the respective eluent. Both were equilibrated for 1 h by joggling in a vortex shaker. After the liquid-solid separation a 500 μL aliquot was taken from the liquid phase of the mixtures and the reference samples for γ-spectrometric determination of the radionuclides present in the liquid phase. The reference samples were used for measurement of the absolute radioactivity of the injected radionuclides. The advantage of this reference based method is the reduction of deviations induced by the volume contraction of binary solvent mixtures and by differing γ-spectrometric geometries, both leading to smaller or larger values of radioactivity. Finally, the K_D value of each system was calculated with the distribution coefficient equation 7 adapted to:

$$K_D = \left(\frac{A_0 - A_{eq}}{A_{eq}}\right) \cdot \frac{V_{aliquot}}{m_{resin}}$$

with A_0: complete activity in liquid phase before equilibrium,
A_{eq}: activity in liquid phase in equilibrium,
$V_{aliquot}$: volume of measured aliquot in mL,
m_{resin}: mass of resin in g.

Promising solvent combinations with separation factors >100 were tested for chromatographic separations. The resins were soaked in the starting eluent for at least 24 h. Columns were prepared with varying diameters (0.5 to 2 cm) and varying length (3 to 10 cm). A portion of the “bulk” chromium-radiomanganese stock-solution was evaporated to dryness and dissolved in ethanol, methanol or a methanol/acetic acid mixture. Additional inactive chromium chloride hexahydrate was added to achieve target like conditions with an inventory of approx. 480 mg elemental chromium. The radioactive cocktail was introduced slowly onto the top of the column and a constant pressure and/or temperature of 55°C was applied depending on the experimental set-up. The eluent was collected manually in 3-10 min fractions depending on the flow rate, reduced to dryness and measured by γ-ray spectrometry for radioactivity.

3.6 Isotopic labelling of manganese nanoparticles

3.6.1 Synthesis of MnO nanoparticles

Radioactive precursor synthesis for isotopic labelling of MnO-nanoparticles

The precursor $^{52g/55}Mn(acac)_2$ was produced batch-wise for each single nanoparticle synthesis. The synthesis was adapted from literature[131] for significant smaller amounts. The reaction is shown in equation 18:

$$MnCl_2 \cdot 4\,H_2O + 2\,C_5H_8O_2 \rightarrow \downarrow Mn(C_5H_8O_2)_2 \cdot 2\,H_2O + Na^+ + Cl^-$$

In a typical precursor synthesis, the $^{52g}Mn^{2+}$ eluent fraction from the radiochemical separation was transferred into a 15 mL glass centrifuge tube, reduced to dryness and 0.4 g (2.0 mmol) $MnCl_2 \cdot 4\,H_2O$ were added. The solid was dissolved in 2 mL HPLC-grade H_2O and the solution degassed for 15 min under a steady argon stream in an ultrasonic bath. The centrifuge tube was sealed and wrapped in aluminium foil for light exclusion. 0.39 g (3.9 mmol) acetyl acetone in 4 mL 1 M NaOH was also degassed under inert atmosphere in an ultrasonic bath for 15 minutes and then slowly injected into the sealed centrifuge tube with a syringe. The directly formed intensively yellow precipitate was separated from the mother solution by centrifugation at 6000 rpm for 3 min and the resulting powder washed two times with HPLC-grade water. The compound was completely submerged in a sand bath and heated at 110°C for 1 h under a steady argon stream in order to remove water of crystallisation. The resulting light tan powder was weighed with the centrifuge tube, and the radioactivity was measured by γ-ray spectrometry. Afterwards it was used without further purification. In the development procedure of the synthesis the inactive precursor was additionally analysed by electrospray ionisation mass spectrometry (ESI-MS).

Inactive microwave assisted MnO-nanoparticle synthesis

Several published synthesis routes for MnO-nanoparticles were tested[132-135] and adapted for microwave use in order to achieve sufficiently short preparation times.

One adapted synthesis route yielded a reproducible nanosized dispersion, stable in 2-propanol for at least 72 h. The synthesis was conducted with 0.0828 g (0.33 mmol) of previously synthesised $Mn(acac)_2$. A mixture of $Mn(acac)_2$, 0.24 g polyvinyl pyridine (PVP) with an avg. molar weight of 40000 g/mol and 5 mL triethylene glycol were degased under a steady Ar stream in an ultrasonic bath for 15 min. The closed vial was then rapidly heated in a microwave oven at 280°C for 5 min and the temperature monitored by an external infrared sensor. The reaction mixture was cooled externally with an air jet to 250°C and then kept at that temperature for 1 h in a microwave oven. The resulting opaque, dark green solution was

precipitated with acetone under Ar atmosphere and centrifuged for 20 min at 8500 rpm. The precipitate was re-dispersed and washed with 2-propanol and precipitated again with acetone and centrifuged for removal of precursor, triethylene glycol and PVP. The washed compound was dispersed in 2-propanol and the clear, brown-black dispersion analysed with DLS and TEM as described in chapter 3.6.3.

3.6.2 Activation studies with water dispersible Mn_3O_4-nanoparticles

For activation studies of nanoparticles, water-soluble Mn_3O_4 particles with a mean crystal size of 25 nm were purchased from Nanograde, a company specialised in the production of nanosized composites. Different direct activation methods were tested and the properties of the nanoparticles before and after irradiations compared. ^{56}Mn and ^{13}N were produced by means of neutron and proton activation of ^{55}Mn and ^{16}O, respectively, and ion leaching of neutron irradiated particles was assessed.

Activation of Mn_3O_4-nanoparticles with charged particles

At the available irradiation facilities no liquid target system was accessible throughout the course of this study. Instead, solid targets of Mn_3O_4 nanoparticle were prepared by slowly evaporated 0.75 mL of an aqueous 2 wt% nanoparticle solution in a sedimentation chamber onto a 50 μm thick Al backing, 13 mm in diameter. The sediments were 10 mm in diameter and carefully covered by a 10 μm thick Al foil which was 16 mm in diameter. The targets were irradiated at the BC1710 cyclotron of the INM-5 with proton energies of 8.2 MeV to exclude proton induced reactions on manganese leading to long living impurities such as ^{54}Fe (half-life: 2.7 a) or ^{54}Mn (half-life: 314 d). Ten minutes after EOB the target was disassembled, the cover foil removed, and the material partly dispersed in 2 mL of distilled water with an ultrasonic bath. The brown dispersion was measured in a Capintec Radioisotope Calibrator CRC-10BC (Capintec) every 5 minutes until complete decay. The measured, logarithmized activity was plotted against the elapsed time since EOB and the half-life determined by fitting a linear function to the data. After complete decay the nanoparticles were analysed with TEM and DLS to check for morphologic or crystallographic deviations induced by charged particle bombardment.

Activation of Mn_3O_4-nanoparticles with neutrons

Two 1.5 mL probes of aqueous 2 wt% Mn_3O_4 nanoparticle solution in 2 mL Eppendorf vials were irradiated at the TRIGA research reactor of the Johannes Gutenberg University Mainz. Together with an additional 1 mL probe of an aqueous 1 wt% solution of manganese (II) acetate they were irradiated for 15 min in the rotary specimen rack with thermic neutrons and

a flux density of $0.7 \cdot 10^{12}$ neutrons per cm^2 and s. The produced ^{56}Mn (half-life: 2.579 h) was measured by γ-ray spectroscopy with no distance to the γ-ray spectrometer. The γ-ray spectrometer was energy and efficiency calibrated with standard point sources (^{133}Ba, ^{137}Cs, ^{152}Eu , ^{241}Am) and a correction factor had to be implemented for the differing measurement geometry of the liquid leaching probes. The $Mn(ac)_2$ probe served as geometric calibration standard by measuring a 20 µl aliquot in the tip of an Eppendorf vial for point-like geometry. The aliquot was diluted to 500 µl and measured again to provide the correction factor for later measurements. The $Mn(ac)_2$ probe was additionally used as calibration standard for the measurement of the manganese content in the irradiated nanoparticles.

Stability and leaching experiments with activated Mn_3O_4-nanoparticles

Four parallel leaching test-series were conducted with the irradiated Mn_3O_4 nanoparticles. Two series with HPLC grade water and two with a medical standard phosphate buffered saline (PBS) at pH 7.4. For each series, 0.5 mL irradiated Mn_3O_4 nanoparticle solution was introduced in a 15 mL glass centrifuge tube and the particles precipitated with 5 mL 2-propanol and 5 mL n-hexane. The 2-propanol was mandatory to achieve solubility between water and n-hexane and, hence, the precipitation. After precipitating the nanoparticles were separated from the solution by centrifugation at 8500 rpm for 10 min. A 0.5 ml aliquot was taken from the top of the solution and the residual supernatant discarded. It was measured by γ-ray spectroscopy for activity quantification. This first aliquot was not used for calculation of released inactive manganese due to high content of the neutron recoil nuclide ^{56}Mn due to the Szilard-Chalmers-Effect.

The solid Mn_3O_4 residue was dispersed in 1 mL HPLC grade water or PBS by means of 3 min treatment in an ultrasonic bath. The resulting dispersion was moved for 2 h with 200 motions per min by a shaker (IKA Labortechnik). Afterwards the particles were again separated from the solution by precipitation, centrifugation, and a 0.5 ml aliquot was taken from the top solution. After discarding the supernatant the procedure was repeated several times until the leached activity was below the detection limits of the used γ-ray spectrometers.

3.6.3 Characterisation of nanoparticles

The size distribution of commercial and synthesised nanoparticles were analysed using TEM and DLS, while the results of the SAED were used in a direct comparison to check for crystallographic changes.

The TEM and DLS measurements complemented each other because TEM only produces images of the naked nanoparticle core and DLS measures size distributions including coating

and/or a solvent shell, but without differentiation between bigger particles or agglomerates. Machine specifications of the different methods for analysis are given in chapter 3.1.

Samples for TEM and SAED were prepared by dilution of the samples and dipping a 3.05 mm diameter 200 mesh copper grid bearing a 10 -15 nm carbon film (PLANO GmbH) for 10-15 seconds into the solution. After removing supernatant liquid from the top of the tweezers with filter paper, the copper grids were placed in a petri dish and dried inside an oven at 50°C for 5 minutes. In each TEM measurement at least three different grid cells were scanned to reveal a more general image of the contained nanoparticles in the sample.

The size of nanoparticles in the resulting images were assessed with a graphic program (ImageJ), collected for all corresponding images and then arithmetically averaged. The size uncertainty was assumed to be the standard deviation.

For DLS measurements the samples were also diluted and macroscopic dust particles removed by a 0.22 μm syringe filter (MILLEX-GP®, MILLIPORE Ireland Ltd.) if no aggregates were apparent. The diluted solution was injected in a disposable polystyrene cuvette (Kartell) and measured by a Zetasizer Nano S (Malvern Instruments) with a standard measurement procedure.

4. Results and Discussion

The development of bi-modal probes and the linked authentic labelling of MR contrast agents include a multitude of research tasks. These concern the field of nuclear physics, nuclear chemistry or organic chemistry. This work, however, concentrated only on the basic questions of the production of the suitable radionuclides ^{52g}Mn and ^{147,149}Gd to build a foundation for future more detailed studies on actually labelled compounds. Different radionuclide production routes as well as separation procedures are discussed in the following chapters and evaluated in prospect for a later application. Also, some proof of principle tests were done to demonstrate the applicability of the developed radionuclides. Additionally, some work was done considering the new field of nanoparticles. However, before these tests can be performed the radionuclides have to be produced.

4.1 Production of radiogadolinium

The cross sections of proton and deuteron induced nuclear reactions for the production of the isotopes ^{146,147,149,151,153}Gd were measured with deuteron energies of up to 70.9 MeV (see Table 12) and proton energies of up to 44.8 MeV (see Table 13). If no radioactivity was detected and no cross section could be determined, the respective spaces are left blank in these tables.

Cross sections for the ^{nat}Eu(d,xn)^{146}Gd and ^{nat}Eu(p,xn)^{147}Gd reactions were determined for the first time. For other measured radioisotopes three data sets up to 50 MeV can be found in literature[74, 76, 136]. The data of West et al.[74] were arithmetically converted to the natural abundance of the corresponding target isotope ^{151}Eu: 47.8 % or ^{153}Eu: 52.2 % [137] in order to allow a comparison.

Table 12: Experimentally determined cross sections of deuteron induced reactions on ^{nat}Eu. Uncertainties are given according to chapters 4.1.6 and 4.1.7.

Energy	**Cross section [mb]**				
[MeV]	**^{146}Gd**	**^{147}Gd**	**^{149}Gd**	**^{151}Gd**	**^{153}Gd**
70.9 ± 0.4	77.7 ± 5.8	169.5 ± 17.8	176.6 ± 16.1	72.1 ± 5.6	8.2 ± 0.6
68.4 ± 0.4	92.0 ± 6.9	152.5 ± 16.5	186.9 ± 19.2	74.9 ± 14.6	13.5 ± 4.9
65.2 ± 0.5	56.8 ± 4.3	159.3 ± 23.0	199.6 ± 21.9	76.7 ± 8.3	9.1 ± 0.9
62.2 ± 0.5	55.2 ± 4.0	160.6 ± 14.2	242.3 ± 24.4	82.9 ± 7.9	23.4 ± 3.2
56.3 ± 0.5	19.8 ± 1.2	190.1 ± 19.0	327.4 ± 32.0	103.2 ± 9.8	16.7 ± 1.8
52.0 ± 0.6	1.6 ± 0.1	128.7 ± 12.5	278.2 ± 30.2	100.9 ± 10.0	14.0 ± 1.1
51.8 ± 0.5	4.5 ± 0.4	141.7 ± 16.0	281.5 ± 30.8	95.5 ± 8.2	13.0 ± 2.2
50.0 ± 0.6	-	92.0 ± 10.7	262.3 ± 28.9	124.3 ± 10.1	16.3 ± 1.3

Table 12 cont.

Energy [MeV]	Cross section [mb]	Energy [MeV]	Cross section [mb]	Energy [MeV]	Cross section [mb]
46.2 ± 0.6	-	41.0 ± 4.6	207.6 ± 27.3	137.5 ± 12.2	17.0 ± 1.3
43.6 ± 0.7	-	13.6 ± 1.3	211.5 ± 15.3	175.9 ± 17.9	22.0 ± 1.5
39.1 ± 0.7	-	0.6 ± 0.1	230.8 ± 24.9	229.4 ± 19.0	21.9 ± 1.7
37.9 ± 0.8	-	-	311.6 ± 23.3	307.5 ± 29.9	26.2 ± 1.8
32.6 ± 0.8	-	-	327.1 ± 34.2	358.5 ± 31.5	39.6 ± 3.7
26.6 ± 1.2	-	-	202.3 ± 19.1	265.9 ± 19.9	43.4 ± 3.8
23.3 ± 0.9	-	-	96.7 ± 12.7	156.6 ± 13.8	53.2 ± 4.0
22.6 ± 1.5	-	-	67.7 ± 6.2	130.5 ± 9.9	59.7 ± 4.3

Table 13: Experimentally determined cross sections of proton induced reactions on ^{nat}Eu. Uncertainties are given according to chapters 4.1.6 and 4.1.7.

Energy	Cross section [mb]			
[MeV]	^{147}Gd	^{149}Gd	^{151}Gd	^{153}Gd
44.8 ± 0.4	179.2 ± 25.6	332.3 ± 36.0	66.4 ± 5.8	6.4 ± 0.5
44.0 ± 0.4	171.3 ± 13.5	330.9 ± 21.8	74.2 ± 4.6	6.9 ± 0.4
43.0 ± 0.4	143.1 ± 15.5	310.4 ± 26.7	76.5 ± 5.3	8.4 ± 0.6
41.9 ± 0.4	105.3 ± 9.5	246.9 ± 15.1	73.8 ± 4.4	7.7 ± 0.5
41.2 ± 0.4	80.6 ± 10.8	228.5 ± 20.0	75.9 ± 4.9	7.8 ± 0.5
40.1 ± 0.5	52.3 ± 4.6	188.7 ± 12.2	77.5 ± 4.6	7.5 ± 0.4
37.6 ± 0.5	11.6 ± 1.0	139.0 ± 9.8	99.5 ± 5.8	7.9 ± 0.4
35.1 ± 0.5	0.39 ± 0.03	156.8 ± 9.5	138.0 ± 8.2	8.3 ± 0.5
32.7 ± 0.6	-	241.3 ± 21.0	212.3 ± 11.8	9.0 ± 0.5
30.2 ± 0.6	-	364.4 ± 23.7	319.1 ± 17.7	9.7 ± 0.5
27.8 ± 0.6	-	425.6 ± 32.2	407.3 ± 22.6	10.5 ± 0.6
25.3 ± 0.7	-	432.3 ± 26.4	429.7 ± 23.9	11.8 ± 0.6
23.0 ± 0.7	-	342.0 ± 30.4	342.7 ± 19.1	12.5 ± 0.7
20.4 ± 0.8	-	215.9 ± 14.4	223.1 ± 12.4	16.3 ± 0.9
18.0 ± 0.8	-	23.8 ± 1.4	40.9 ± 2.3	16.6 ± 0.9
15.5 ± 0.9	-	-	22.3 ± 1.2	25.4 ± 1.4

Modelled cross section data from the TENDL-2013 library [138, 139] which is based on the computer code TALYS[140] were used for comparison with the experimental data and are

shown in Figures 18 - 25. But for this comparison, it has to be kept in mind that the data available in TENDL-2013 is modelled only with standard parameters for the nuclear models implemented in TALYS resulting in a qualitative description of excitation functions at best. The computer code TALYS takes into account nuclear models for the optical model, level densities, direct reactions, compound reactions, pre-equilibrium reactions, fission reactions, and a large nuclear structure database. Until now, not all these mechanisms involved in nuclear reactions are completely understood and cannot perfectly be modelled. Therefore, experimental data is necessary to further develop these model calculations towards reality.

For comparison of the experimental and modelled data the calculated values had to be adjusted for the natural elemental composition. The cross section values from TENDL-2013 were multiplied by the natural abundance of the respective isotope. If multiple nuclear reaction channels result in the same radionuclide, the resulting partial cross sections were summed up leading to the cumulative cross sections of the respective radionuclide.

Additionally, the experimentally observed reaction thresholds were compared with their respective theoretical threshold energies (see Table 2). A reaction threshold shift of the experimental data towards higher energies in comparison to the theoretical values was observed in almost all reactions.

4.1.1 Beam profile, beam current and particle energy analysis

For the deuteron irradiations at the internal target station of the cyclotron JULIC, the beam was found to be sufficiently focused and only a minor spread was observed. This was in contrast to the test irradiation with protons at the same target system. It was not possible to focus the beam onto the centre of the foil stack (see Figure 11 left) and the beam position deviated between the first and the last foil. This potentially leads to systematic uncertainties and would demand for additional monitoring of the beam throughout the whole target, making the internal target system less useful for cross section measurements. The new external target system showed sufficient beam focusing capabilities with no visible shift between the first and the last monitor foil in the stack (see Figure 16).

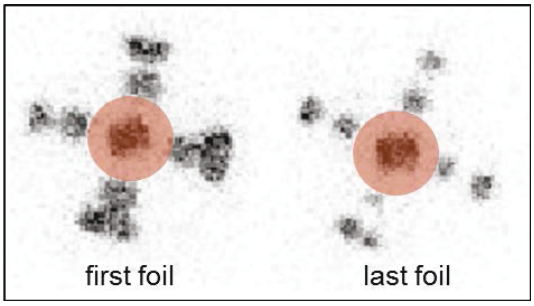

Figure 16: Beam position in the proton irradiations at the external target; illustrated by monitor foils 15 mm in diameter and spatial ^{22}Na orientation marks.

The published excitation functions of the recommended proton monitor reactions are not suitable for the determination of the experimental particle energy in the investigated energy range. The cross section ratios of the recommended deuteron monitor reactions are either poorly distinguishable above 50 MeV (see Figure 17), or the cross sections are too low to generate sufficient activity for adequate counting statistics.

Therefore, measurement of the beam energy was done by determining it for the more reliable lower energy region of the target and then extrapolating it up to the incident energy using STACK. This revealed a deviation between the incident energy in different irradiations which resulted in the incident energy uncertainty of deuteron irradiations as discussed below in chapter 4.1.6.

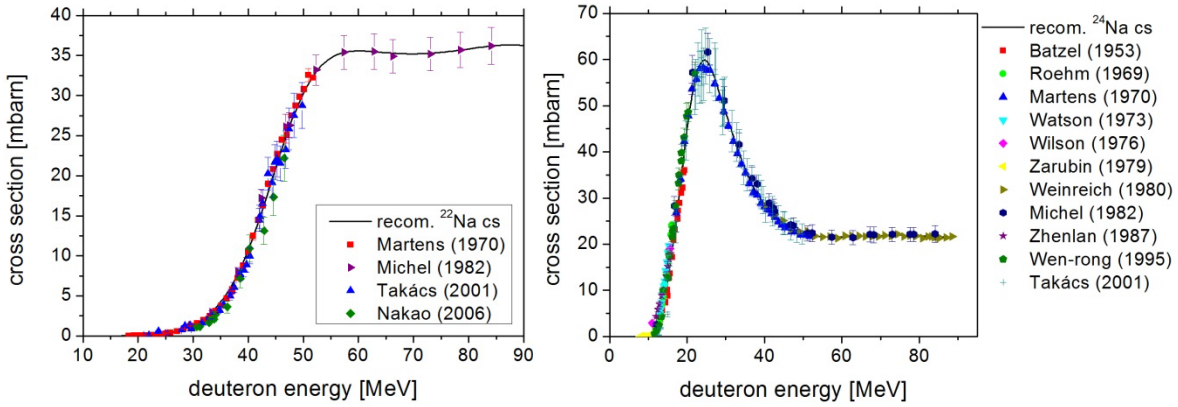

Figure 17: Recommended cross sections of the deuteron induced nuclear reaction $^{27}Al(d,x)^{22}Na$, $^{27}Al(d,x)^{22}Na$ and individual literature data taken from IAEA-TECDOC-1211.[121]

4.1.2 Cross section of main product ^{147}Gd

For both proton and deuteron induced reactions leading to the formation of ^{147}Gd, the experimental thresholds (see Tables 12 and 13) are higher than their theoretical values (see Table 2). They are, however, still in good agreement with previously published deuteron cross section measurements by Takács et al.[76], even if they are partly higher in value.

The experimental cross section data of the reactions with deuterons is depicted in Figure 18 showing a first maximum at about 57 MeV which is due to the $^{151}Eu(d,6n)$-nuclear reaction.

A second increase above 70 MeV indicates another maximum at higher particle energies which corresponds to the $^{153}Eu(d,8n)$-reaction channel. However, the expected second maximum seems to be located at even higher deuteron energies than available in this work (see Figure 18). The theoretical values given by the TENDL-2013 library seem to be shifted to lower particle energies by an offset of approx. 5 MeV. The cross sections of proton induced reactions leading to the formation of ^{147}Gd are given in Figure 19.

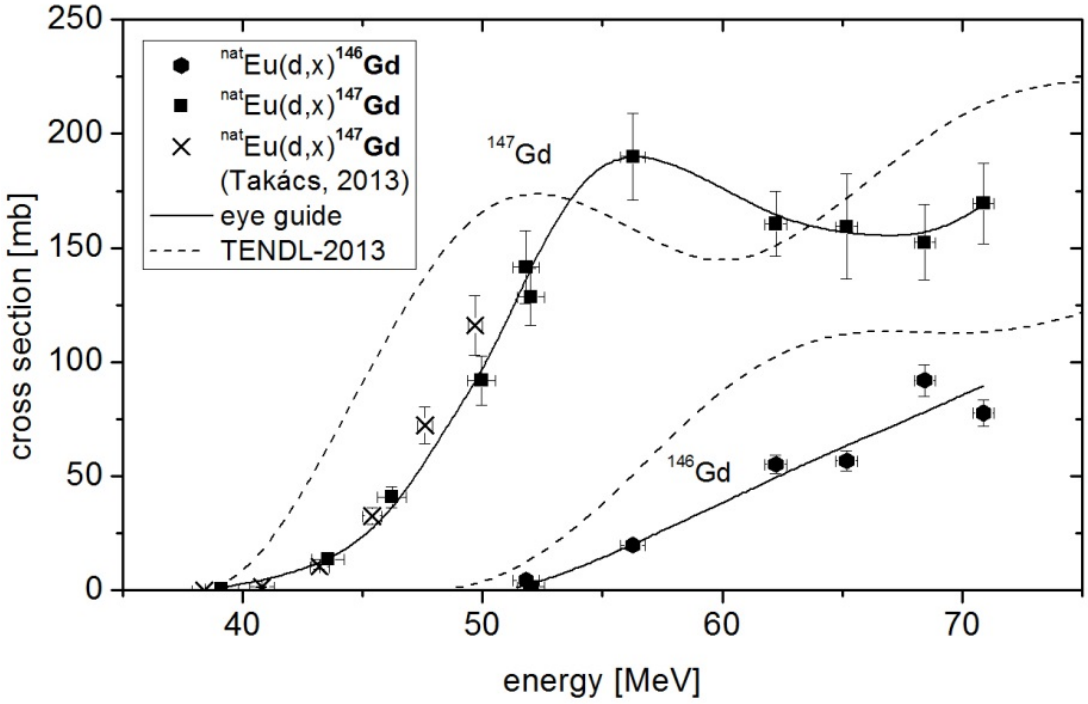

Figure 18: Cross sections of ^{146,147}Gd formation by deuteron induced reactions on ^{nat}Eu and theoretical cross section data from TENDL-2013[138, 139]. Eye guides drawn through own data points.

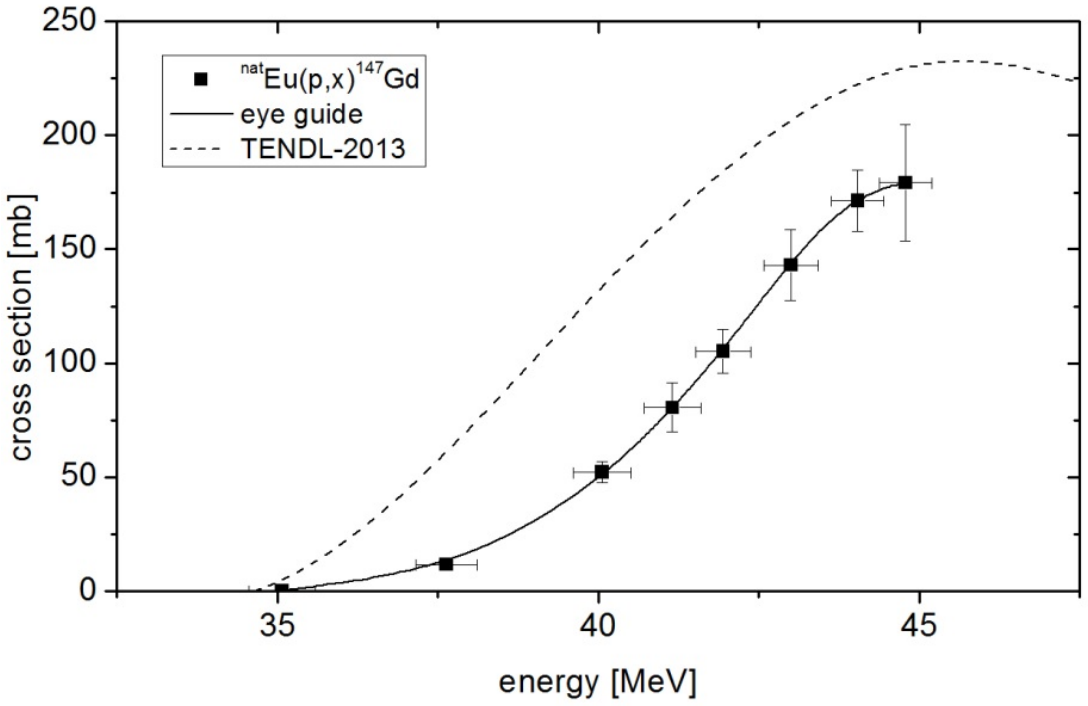

Figure 19: Cross sections of ^{147}Gd formation by proton induced reactions on ^{nat}Eu and theoretical cross section data from TENDL-2013[138, 139].

Again, the theoretical calculation shows a slightly shifted excitation function to lower particle energies by approx. 2.5 MeV. Due to comparable cross sections, but with lower reaction thresholds, proton induced reactions seem to be superior for the production of ^{147}Gd.

The radionuclide production yield is not the only relevant parameter regarding the medical application of Gd radioisotopes. For absolute quantitation in SPECT a high isotopic purity is even more important[141]. Problematic impurities to be considered with the application of ^{147}Gd are ^{149}Gd and ^{151}Gd. This is due to interfering γ–rays of ^{147}Gd: 229.3 keV (57.7 %), ^{149}Gd: 272.3 keV (3.2 %) and ^{151}Gd: 243.3 keV (5.6 %). The impact of those impurities is discussed in detail together with a comparison of production rates in chapter 4.1.5.

4.1.3 Cross section of main product ^{149}Gd

Both, the excitation functions of the deuteron and proton induced reactions leading to ^{149}Gd show two maxima (see Figures 20 and 21) which corresponds well to the reaction channels ^{151}Eu(d,4n), ^{153}Eu(d,6n), ^{151}Eu(p,3n) and ^{153}Eu(p,5n).

After converting the data of West et al.[74] to the natural abundance of the respective europium isotopes, there was a very good agreement of the shape of the excitation functions with the other literature data[76] and the measurements done in this work.

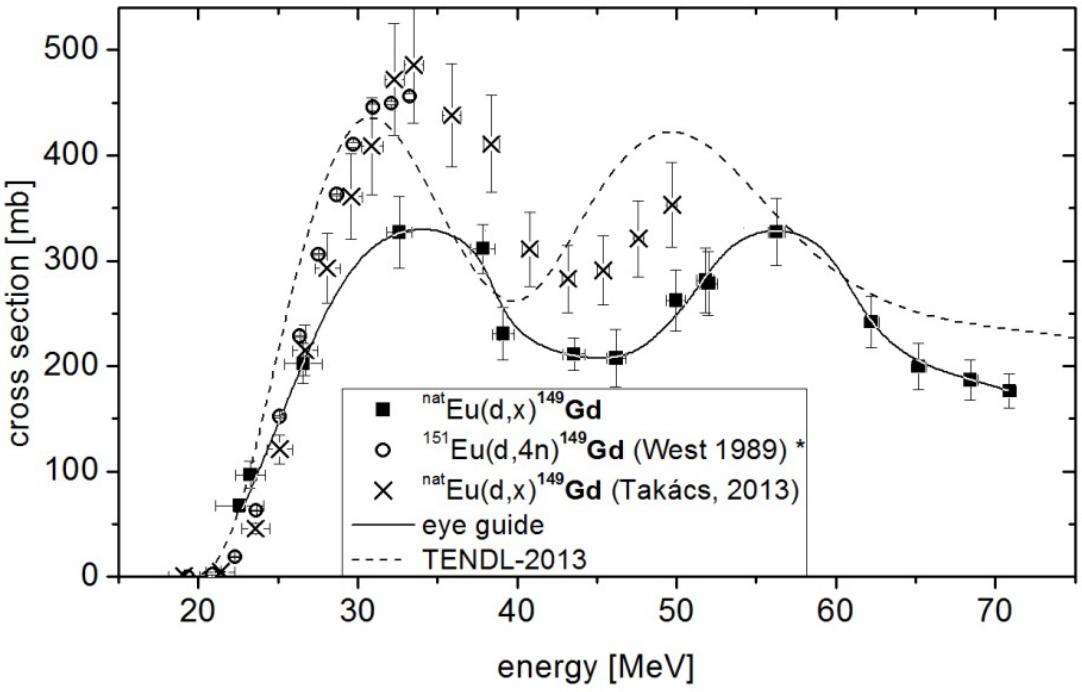

Figure 20: Cross sections of ^{149}Gd formation by deuteron induced reactions on ^{nat}Eu and theoretical cross section data from TENDL-2013[138, 139].
* Data adapted to natural abundance.

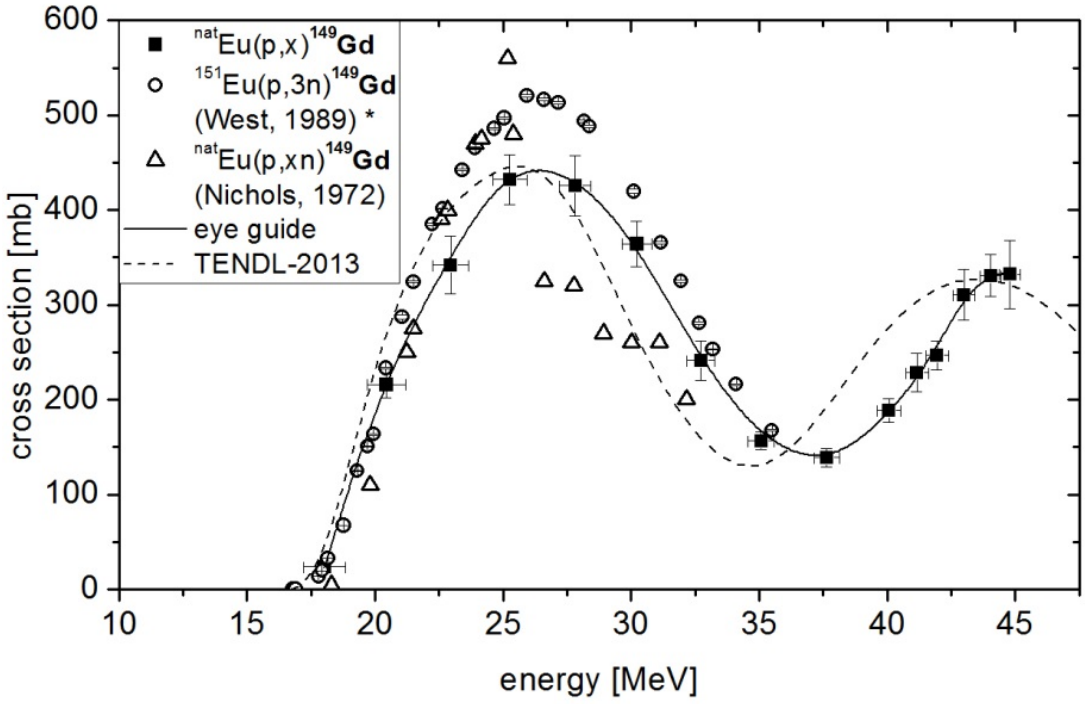

Figure 21: Cross sections of ^{149}Gd formation by proton induced reactions on ^{nat}Eu and theoretical cross section data from TENDL-2013[138, 139].
* Data adapted to natural abundance.

However, a clear deviation in magnitude at the maxima of the curves is apparent. In the region of the maximum of deuteron induced reactions at approx. 35 MeV the measured cross section values are up to 30 % lower and in case of proton induced reactions at 26 MeV up to 20 % lower in comparison with the literature[74, 76].

Other proton cross section data[136] deviate not only in magnitude (up to 30 % higher/lower) but also in the shape of the excitation function. This deviation cannot be explained by outdated half-life values or γ-ray intensities as their differences were found to be negligible. Also no significant error in the described measurement technique was found in retrospective. The data published by West et al.[74] and Takács et al.[76] agree more with the data measured in this work.

The theoretical cross section values from the TENDL-2013 library for nuclear reactions leading to the formation of ^{149}Gd show a similar trend as discussed for ^{147}Gd above. In this case, not the whole theoretical excitation function is shifted to lower particle energies. The experimental data in the lower deuteron energy region up to 25 MeV and in the lower proton energy up to 22.5 MeV are well described by the theoretical calculations. On the other hand, the theoretical maxima appear to be too narrow in comparison with the experimental data causing a shift of the excitation function in the higher energy region towards lower values.

This is clearly an effect of the already implemented older literature data[136] in the TALYS code parameters. In the higher energy region where no data is available the code differs again from reality.

4.1.4 Cross section of isotopic impurities ^{146,151,153}Gd

As depicted in Figure 18, production of ^{146}Gd was only observed for deuteron energies above 52 MeV. The formation of ^{146}Gd near its reaction threshold is apparently too small and cannot be distinguished from the background of the γ-ray detectors used. The same seems to be true for the proton irradiations because in the energy range of 45 to 15 MeV no ^{146}Gd could be observed at all. In addition to higher cross section values, the cross sections calculated with the TALYS computer code taken from the TENDL-2013 database also indicate a small maximum at approx. 65 MeV deuteron energy which could not be confirmed experimentally. Further investigations would be necessary to explain the reason of this.

Concerning ^{151}Gd, only the cross section maxima of the ^{153}Eu(d,4n)^{151}Gd (see Figure 22) and ^{153}Eu(p,3n)^{151}Gd (see Figure 23) reactions are recognizable at approx. 34 MeV and 25 MeV, respectively. The slope of the experimental curve points to the theoretical thresholds of their corresponding reactions (^{153}Eu(d,4n): 18.6 MeV; ^{153}Eu(p,3n): 16.2 MeV). More than a rough extrapolation is not possible here. This is due to overlap with reactions of lower threshold energies (^{151}Eu(d,2n), ^{151}Eu(p,n)).

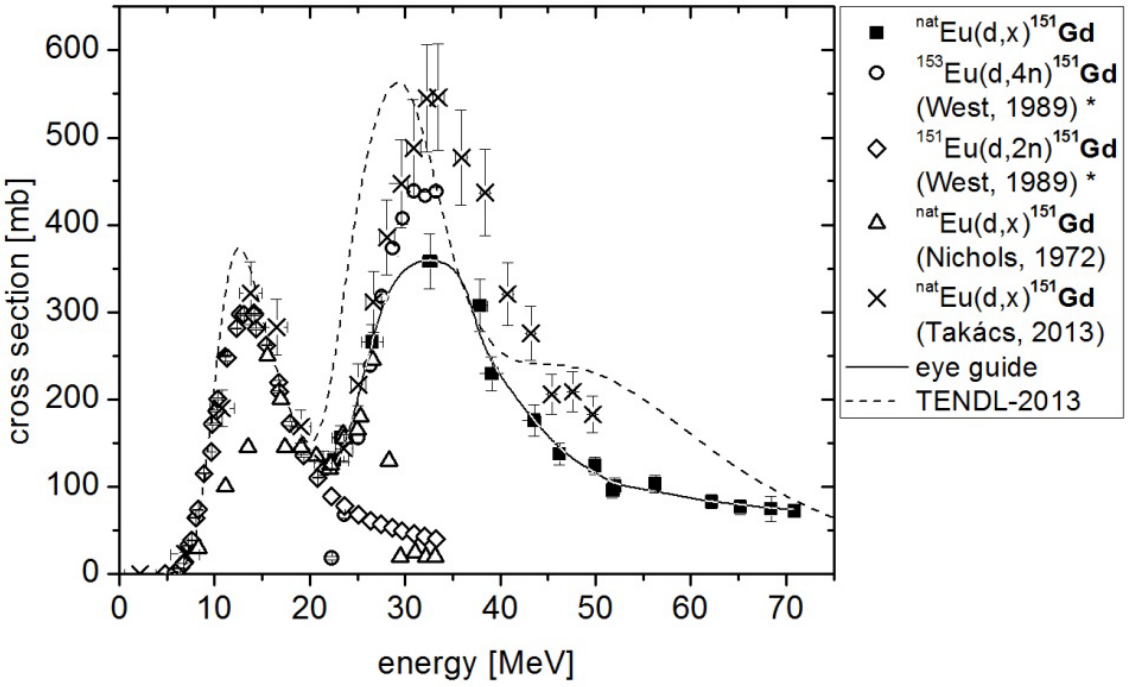

Figure 22: Cross sections of ^{151}Gd formation by deuteron induced reactions on ^{nat}Eu and theoretical cross section data from TENDL-2013[138, 139].
* Data adapted to natural abundance.

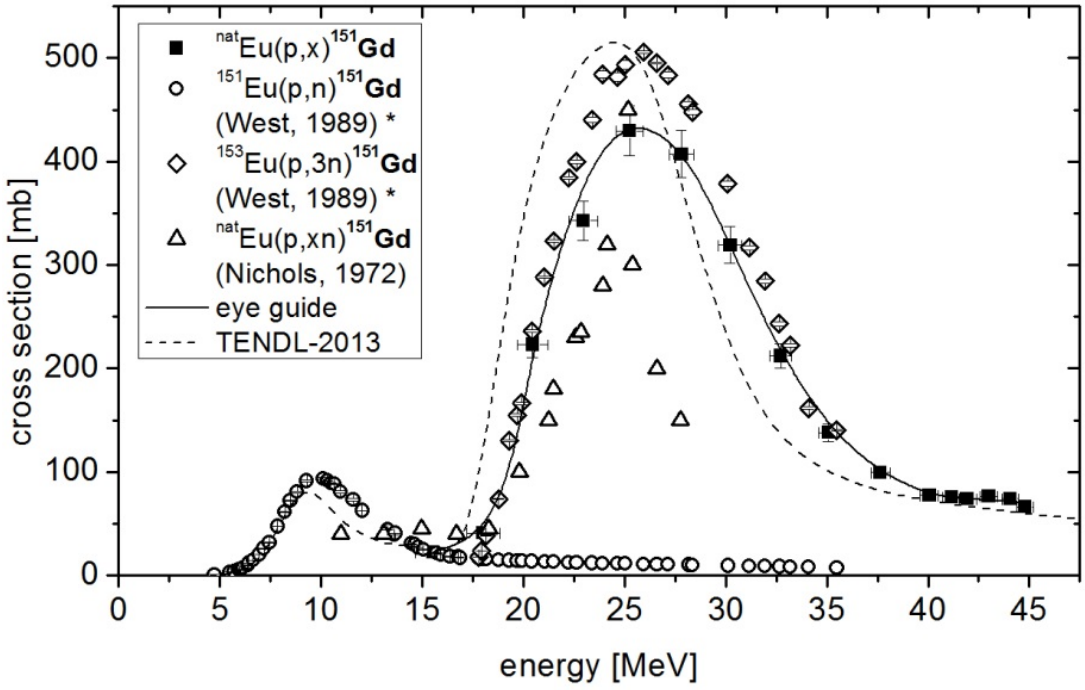

Figure 23: Cross sections of ^{151}Gd formation by proton induced reactions on ^{nat}Eu and theoretical cross section data from TENDL-2013[138, 139].
* Data adapted to natural abundance.

The shape of the excitation function, including the transition from the end of the first maximum to the beginning of the second one (see Figure 22), agrees well with previous data[74, 76]. However, the magnitudes of West's data[74] differ in the peak area by up to 18 % for deuteron and up to 15 % for proton induced reactions. An even higher value for the cross section maximum for deuteron induced reactions was measured recently by Takács et al.[76] which is up to 40 % higher.

Regarding the data of West et al.[74], it is interesting to notice that contrary to the EXFOR classification, no highly enriched ^{151}Eu or ^{153}Eu target material was used. Instead, the cross sections were extrapolated to 100 % enrichment from irradiation of natural europium. While this is acceptable in some cases, a problem arises in the overlapping area (33 → 18 MeV) of lower and higher reaction orders of ^{151,153}Eu. A clear assignment of ^{151}Gd activity originating from one or the other reaction is simply not possible above 20 MeV.

Therefore, the cross section data had been deduced by adjusting a normalised polynomial fit from the first order ^{153}Eu(p,n)^{153}Gd and ^{153}Eu(d,2n)^{153}Gd reactions to the cross section data of the second order ^{151}Eu(p,n)^{151}Gd and ^{151}Eu(d,2n)^{151}Gd reactions below 17 MeV proton and 22 MeV deuteron particle energy, respectively, in order to yield the cross sections in the overlapping energy region. Cross section data for the higher order reactions ^{153}Eu(p,3n)^{151}Gd

and ^{153}Eu(d,4n)^{151}Gd was then obtained by subtraction of those deduced data from the experimentally measured data. It is questionable, if this approach is reliable because excitation functions[142] show only similar, but never exactly equal shapes of the curve tail. Thus, only the data for ^{nat}Eu is shown here. Therefore, the cross section data of West et al. for the production of ^{151}Gd should be neglected in future evaluations. Regarding the results of TENDL-2013, the same trend as already discussed in the previous chapter is also found for deuteron and proton induced reactions, namely a good match to the experimental data in the lower energy region and larger deviations in the higher energy region.

The deuteron cross section data for the formation of ^{153}Gd measured in this work (see Figure 24) increasingly deviate by up to 42 % from previous measurements[74, 76] with decreasing particle energy, but they agree with the publication of Nichols[136] in the small overlapping area (27 → 23 MeV). The theoretical data below 30 MeV agree well with previous measurements of Takács et al.[76] and West et al.[74] and above 30 MeV with the data measured here.

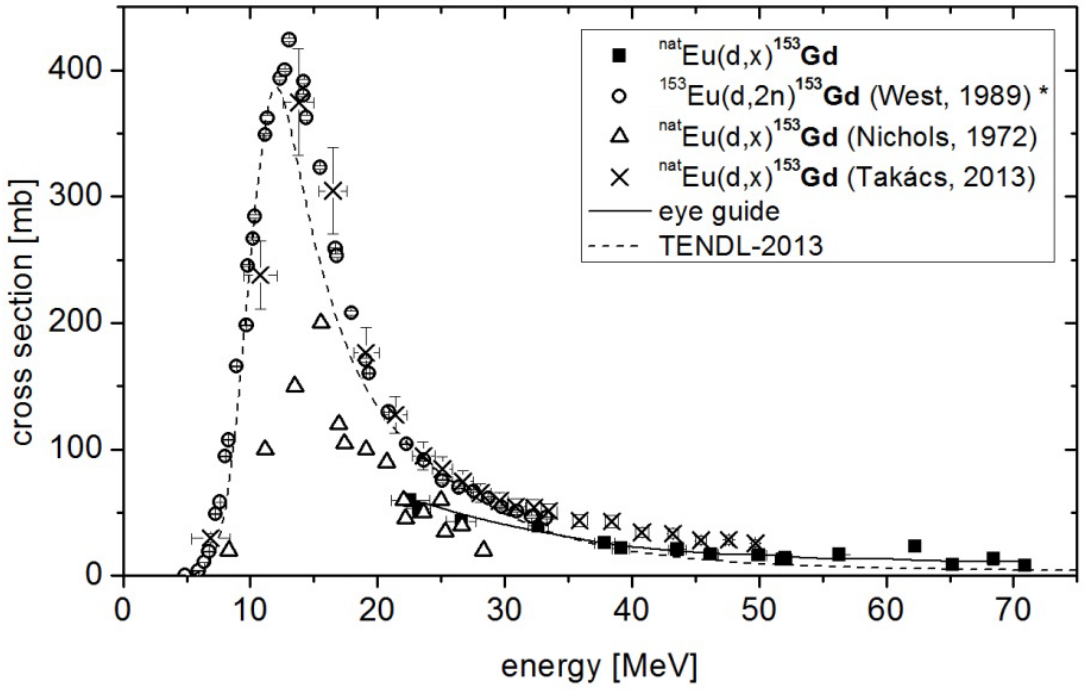

Figure 24: Cross sections of ^{153}Gd formation by deuteron induced reactions on ^{nat}Eu and theoretical cross section data from TENDL-2013[138, 139].
* Data adapted to natural abundance.

The proton induced reaction cross sections measured in this work (Figure 25) are identical with the available data[74] within the uncertainties. The theoretical values from TENDL-2013, on the other hand, differ strongly from the experimental results above 10 MeV and show a

maximum lower in energy as well as in height. In general, the overall trend of a complete or partial energy shift between the theoretical excitation functions from the TENDL-2013 library and experimentally available data persists throughout all measured reactions. This clearly demonstrates the need for experimental nuclear data to further improve the empirical adjustment of reaction parameter in the nuclear models as mentioned in the beginning of chapter 4.1.

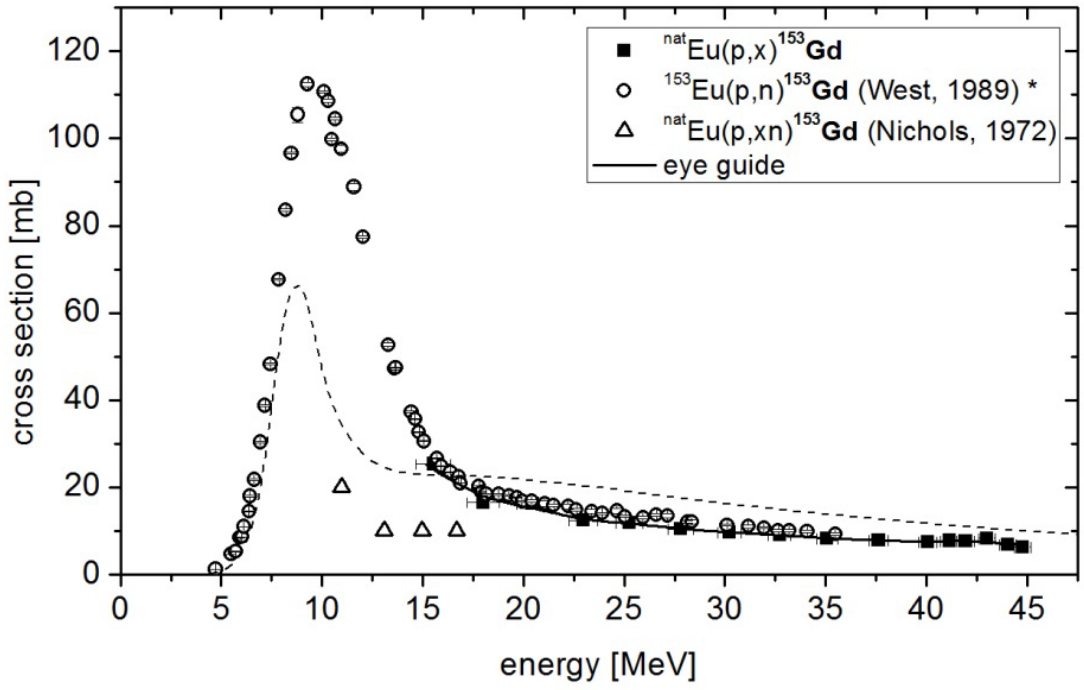

Figure 25: Cross sections of ^{153}Gd formation by proton induced reactions on ^{nat}Eu and theoretical cross section data from TENDL-2013[138, 139].
* Data adapted to natural abundance.

4.1.5 Experimental thick target and calculated integral yields

The integral production rates and saturation yields of the radionuclides ^{147,149}Gd and isotopic impurities were determined for proton and deuteron bombardment using the measured cross sections shown above (see Tables 12 and 13) and are summarised in Table 14.

The shapes of the integral curves for deuteron and proton induced reactions (see Figures 26 and 27) are very similar, but the deuteron integral curves shift to higher energies by an amount of about 7.5 MeV. This corresponds to the higher energy thresholds for deuteron induced reactions.

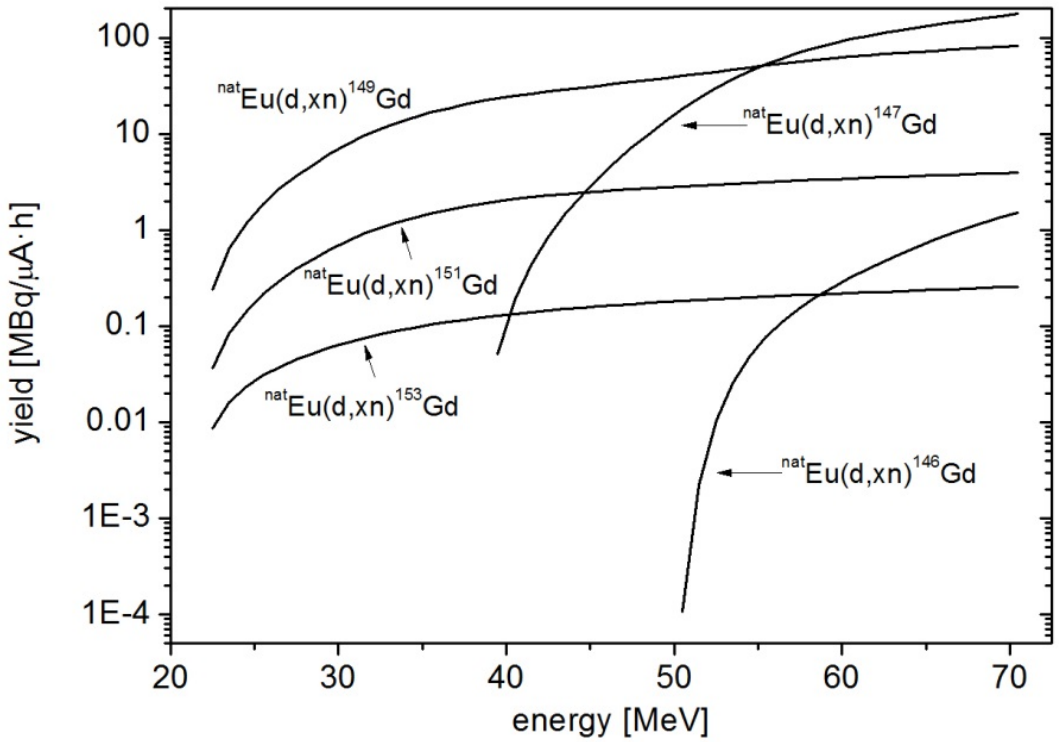

Figure 26: Calculated integral yields of ^{146,147,149,151,153}Gd based on the experimentally determined excitation functions (eye guides) of deuteron induced reactions on natural europium.

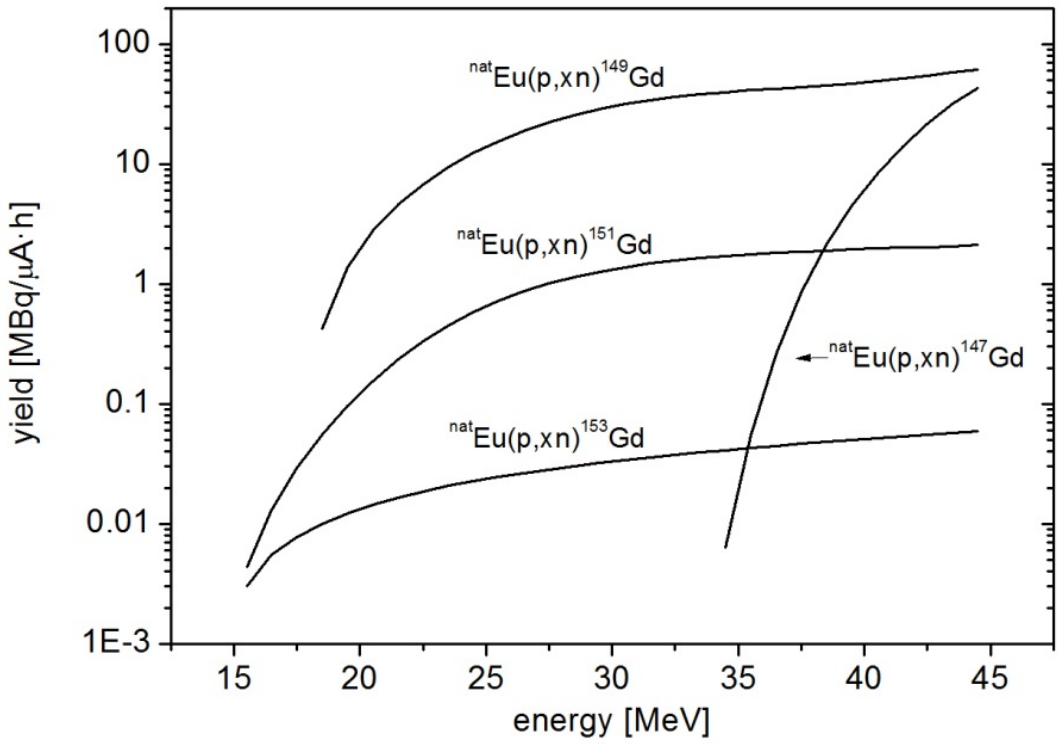

Figure 27: Calculated integral yields of ^{147,149,151,153}Gd based on the experimentally determined excitation functions (eye guides) of proton induced reactions on natural europium.

Table 14: Calculated production rates using elemental europium for thin targets integrated over the measured energy range.
Uncertainties given are calculated according to chapter 4.1.7.

Isotope	$IntY_{prod}$ [a] (deuteron) [MBq/μAh]	$IntY_{prod}$ [b] (proton) [MBq/μAh]
^{146}Gd	1.51 ± 0.27	-
^{147}Gd	177.33 ± 19.71	43.30 ± 4.39
^{149}Gd	81.59 ± 8.51	61.83 ± 4.94
^{151}Gd	3.96 ± 0.42	2.11 ± 0.27
^{153}Gd	0.26 ± 0.04	0.59 ± 0.004

a) Integral production rates calculated for 71 → 22 MeV deuteron energy.

b) Integral production rates calculated for 45 → 15 MeV proton energy.

The thick target yields of proton bombardments were also experimentally determined (see Table 15). These measured values are 20 – 25 % lower than the calculated integral yields. Some deviation of approx. 5-30 % is to be expected due to experimental artefacts, e.g. thermal effects within thick targets during irradiation which influence the actual area weight among others.

Table 15: Comparison of experimentally determined thick target yields and calculated integral yields of proton induced reactions on ^{nat}Eu and percentages of integral yields for corresponding energy ranges.
Uncertainties given are calculated according to 4.1.7.

Isotope	TTY_{prod} [MBq/μAh]	$IntY_{prod}$ [MBq/μAh]	$IntY_{prod}$ fraction [%]
		45 → 31 MeV	
^{147}Gd	27.89 ± 1.53	34.15 ± 3.45	81.7
^{149}Gd	19.63 ± 0.99	23.74 ± 1.89	82.7
^{151}Gd	0.79 ± 0.04	0.96 ± 0.12	82.0
^{153}Gd	0.025 ± 0.003	0.0337 ± 0.0005	75.5
		36 → 18 MeV	
^{147}Gd	-	-	-
^{149}Gd	27.10 ± 1.37	33.43 ± 3.88	81.1
^{151}Gd	1.83 ± 0.07	2.33 ± 0.30	78.6
^{153}Gd	0.037 ± 0.003	0.0494 ± 0.0009	75.9

Proton and deuteron yields of the ^{147}Gd production were found to be considerably higher than for the previously reported ^{3}He- and α-particle reactions with incident energies of 27.1 MeV and 35.8 MeV, respectively.[75] The proton and deuteron induced production of ^{147}Gd show integral yields of (177.33 ± 19.71) MBq/μAh and (43.30± 4.39) MBq/μAh, respectively. In comparison, Denzler et al.[75] reported 9.5 MBq/μAh for ^{3}He and 4.8 MBq/μAh for α-particle induced processes. Those earlier values were also extrapolated to 100 % enrichment of the target material ^{144}Sm (used: 86.6 %, nat.: 3.07 %) and ^{147}Sm (used: 96.5 %, nat.: 14.99 %), while here values are calculated with natural abundances.

These lower production rates are mainly caused by stronger energy degradation of doubly charged particles ($^{4}He^{2+}$, $^{3}He^{2+}$) in matter. Therefore, a lower mass of target material was used by Denzler et al.[75]. However, they achieved a significantly higher isotopic purity employing targets of enriched samarium than obtained here by use of natural europium. In case of natural europium, the formation of the longer lived isotopic impurities ^{146,151,153}Gd is calculated to be rather low (<5 %) and not of primary concern for SPECT measurements. More problematic is the simultaneous production of ^{147}Gd and ^{149}Gd interfering with each other (see Figure 27).

Thus, employing europium, highly enriched targets are required to achieve a high isotopic purity. Albeit, enrichment of either stable europium isotope is much cheaper compared to samarium due to almost equal proportions of ^{151}Eu (47.8 %) and ^{153}Eu (52.2 %) in the natural isotopic composition. Hence, application of enriched europium would not only yield considerable higher amounts of ^{147}Gd or ^{149}Gd but also be more beneficial than application of enriched Sm, considering its high production costs due to the low natural abundances of ^{144,147}Sm (see above).

Another important factor for the application of radiogadolinium in SPECT is the presence of impurities resulting from the decay products of gadolinium like ^{147}Eu ($T_{1/2}$: 24.1 d, γ-rays: 121 keV (23%), 197 keV (27 %)) or ^{149}Eu ($T_{1/2}$: 93.1 d, γ-rays: 277 keV (3.6 %)). While this problem is the same for the production by proton or deuteron bombardment as well as production by α-particles, the direct formation of those isotopes is much higher if europium is applied as target material. In this context, irradiation of samarium would be more favourable due to the more efficient radiochemical separation methods presently available which would be needed to remove those decay products. Rapid separation of gadolinium from bulk europium is possible, but needs excessive effort[78, 108]. Unfortunately, this cannot be easily circumvented, or ignored, due to the similar γ-ray energies of the decay products. Therefore, as part of this study a fast and facile separation of radiogadolinium and europium was developed.

4.1.6 Particle energy uncertainties

Two factors were taken into account for the uncertainty determination of the individual particle energies of cross sections: The degradation in the Eu_2O_3 targets and the energy dependent uncertainty of the incident energy. This uncertainty was calculated by iteration of the foil-stack energy degradation with the maximal and minimal possible incident energy (+/- $\Delta E_{incident}$). Half of these deviations between upper and lower energies were used as dependent uncertainty of the incident energy at the corresponding target energy. The Gaussian propagation (root mean square) of this general uncertainty of the incident projectile energy and the uncertainty of the energy degradation in the specific target yielded the particle energy uncertainty for each individual target in the foil stacks.
This results in an overall uncertainty for deuterons from 0.4 MeV at 75 MeV up to 1.5 MeV at 20 MeV. For proton irradiations it ranges from 0.32 MeV at 45 MeV up to 0.60 MeV at 18 MeV. The overall uncertainties are given together with the experimental cross section data in Tables 12 and 13 above.

4.1.7 Cross section and yield uncertainties

Several further sources of uncertainties besides that of particle energy have to be considered for the measured cross sections and thick target yields and are as follows:

- area weight determination,
- particle flux determination,
- detector efficiency,
- peak fitting,
- counting statistics for γ-ray energy,
- γ-ray intensity.

The individual uncertainties of the area weight determination of foils and sediments derived from weighing and uncertainty of area determination ranged from 1.7 to 4.8 %. The total uncertainty in particle flux determination ranged between 3.5 to 8.8 %, due to uncertainties in activity measurement, particle energy and in monitor reaction cross sections taken from literature[121]. The uncertainty of detector efficiencies lay between 2.8 and 8.6 % depending on γ-ray energy, due to the limited coverage with standard radiation sources over the investigated energy region. The statistical uncertainty ranged from 0.05 up to 12 % in peak areas, due to Gaussian-shaped peak fitting with strongly varying counting statistics dependent on activity, γ-ray intensity and efficiency of detectors for the γ-ray energy. The γ-ray intensity uncertainty of 0.5 to 5 % was taken from literature[60].

Considering additional minor uncertainties, e.g. in molar weight, half-life etc., the individual uncertainties of the final cross section data were calculated according to Gaussian error propagation (root mean square). In total, the resulting absolute uncertainty of cross sections measured in this work ranges between 6.0 and 17.1 %.

4.2 Separation of n.c.a $^{147/149}$Gd from bulk ^{nat}Eu with a Na-Hg amalgam extraction

For the separation of a lanthanide mixture of europium and gadolinium a promising approach was tested based on a liquid sodium-mercury amalgam and a buffered saline solution.[78, 108] After a test run with a minimal target mass of 0.5 mg Eu_2O_3 and the separation conditions determined by Denzler et al.[78], the need for an optimization became clear when dealing with macroscopic europium masses. The parameters with the strongest influence on the reduction and selective extraction of one particular lanthanide are the pH-value as well as the sodium content in the amalgam and the solution, hence, its reductive potential and extraction capacity. There are some restrictions to both parameters and their adjustment. Sodium mercury amalgam gets solid at room temperature above a sodium content of about 0.7 wt%. Therefore, the capacity can only be changed significantly by increase/decrease of the used mass of amalgam. The pH range is limited by the decomposition of sodium mercury amalgam below a pH-value of 1.5 and the precipitation of lanthanide hydroxides above a pH of 8. Unfortunately, the pH-value of the solution increases gradually during the extraction because of the steady production of H_2 and OH^- by the competing reaction 19:

$$\mathrm{Na} + \mathrm{H_2O} \rightarrow \mathrm{Na^+} + \mathrm{OH^-} + \frac{1}{2}\mathrm{H_2}$$

A buffer solution has to be introduced and the starting pH has to be low enough that the pH-value stays below 8 until the end of separation. The already published process of Lebedev et al.[77] mentions the use of a starting pH of 4.5 which makes a strong buffer solution mandatory or it cannot yield satisfying results. With the goal in mind to label an organometallic complex and to inject it into an animal or even human, any additionally introduced ion or compound can lead to complications. Thus, the reported separation was assessed anew and the optimal separation parameters were determined systematically.

At first the capacity of the amalgam separation conditions determined by Denzler et al.[78] was assessed by increasing the europium mass. Other parameters were kept constant at:

- 1 M saline solution buffered with 0.4 M sodium acetate,
- starting pH = 2,
- 5 mL (67.72 g) amalgam,
- 0.4 % sodium content, and
- 5 min reaction time.

The results are shown in Figures 28 and 29 for a first extraction (E1) and a subsequent second extraction (E2) with a new batch of amalgam. Inductively coupled plasma – mass spectrometry (ICP-MS) was necessary beside the γ-spectrometric measurements (γ-spec.) to assess low Eu concentrations with a sufficient accuracy.

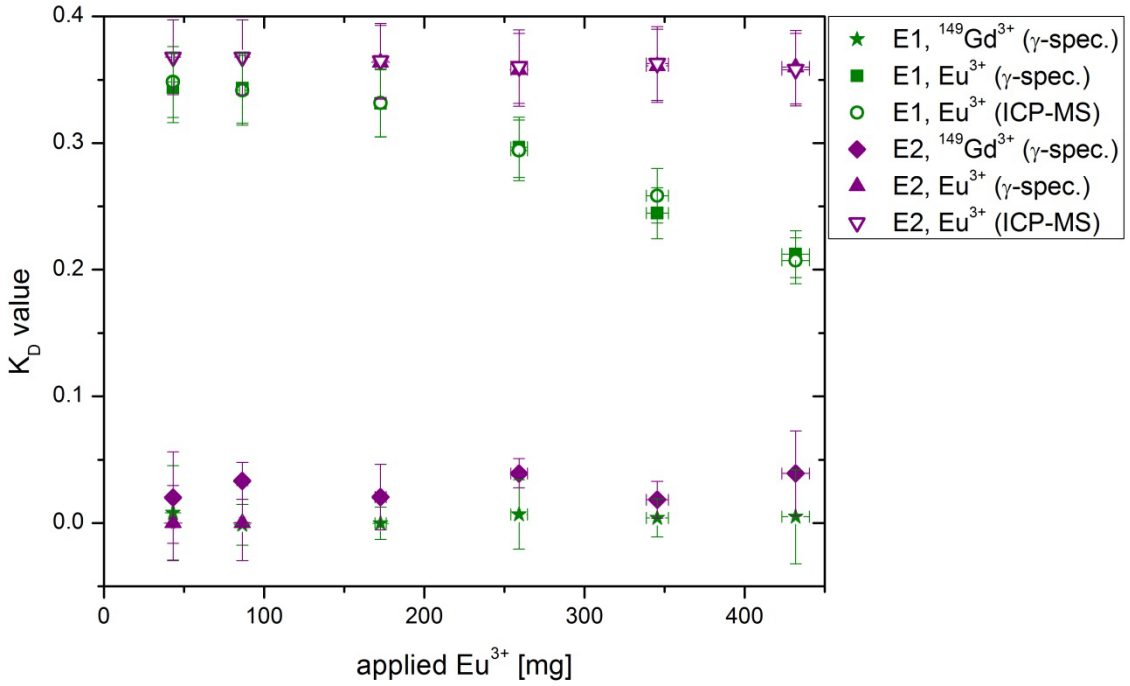

Figure 28: Extraction coefficients of europium of varying amounts.

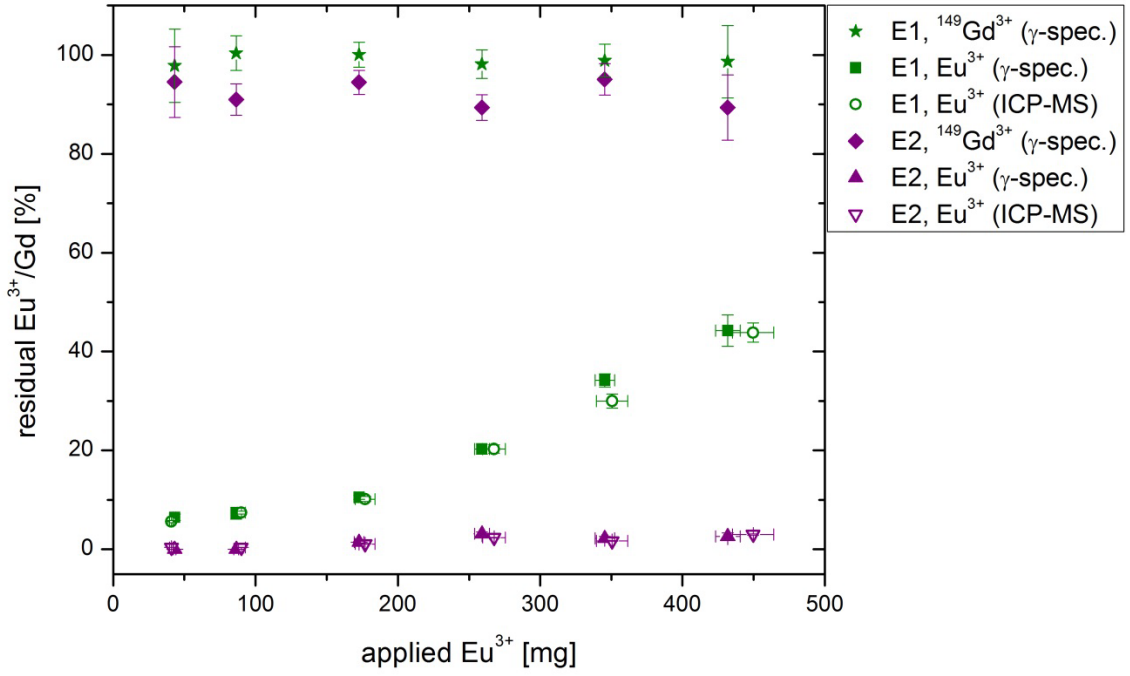

Figure 29: Extraction yield of varying amounts of europium and ^{149}Gd with varying content in percent.

The residual mass of Eu^{3+} in solution increased as expected with the Eu^{3+} mass after the first extraction. A second extraction with a new batch of amalgam was therefore appended directly after the first extraction. This should lead to a suitable Eu reduction as described by Denzler et al.[78]. However, the subsequent second extraction only reduced the amount of residual Eu^{3+} to approx. 14 mg with a 500 mg Eu_2O_3 target. This 97 % reduction could be further improved by more extraction repetitions, but with the disadvantage of decreasing yields of the Gd radioactivity. While no significant extraction of radiogadolinium can be observed into the amalgam, a yield reduction can easily occur due to physical loss of fluids caused by not optimised solution handling.

Next, the volume of used amalgam was increased step-by-step to find the minimal mass of amalgam necessary for the separation of the complete 500 mg Eu_2O_3 within one extraction step. The other parameters were kept constant as described above. The results are depicted in Figures 30 and 31.

The fluctuating results of the radioactivity derived determinations seen in all diagrams are measurement artefacts due to the statistical decay uncertainty. The extraction capacity increases nearly linearly, corresponding to the elemental sodium content present during the extraction. Correspondingly, the distribution coefficients stay nearly the same until a volume of 9 mL amalgam was reached and the capacity of the used amalgam was high enough to extract nearly all Eu from the solution. The constant sodium concentration in the amalgam was 0.4 wt% which corresponds to 542 mg of elemental sodium in 10 mL amalgam.

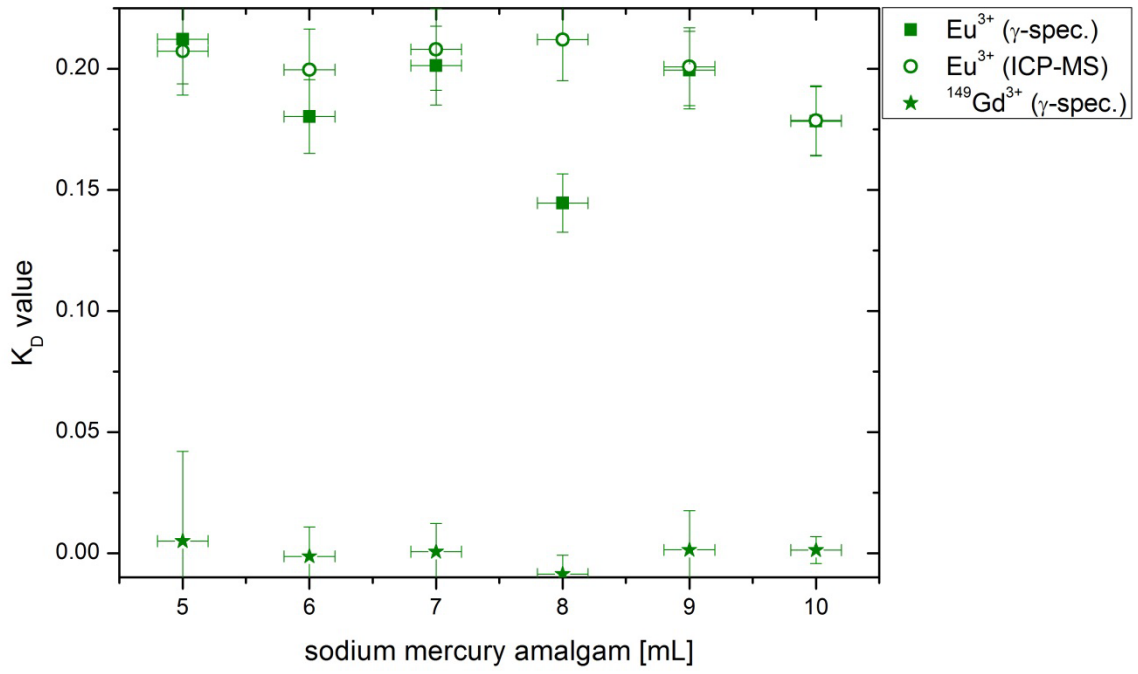

Figure 30: Extraction coefficients of varying amounts of europium and ^{149}Gd with varying sodium mercury amalgam masses.

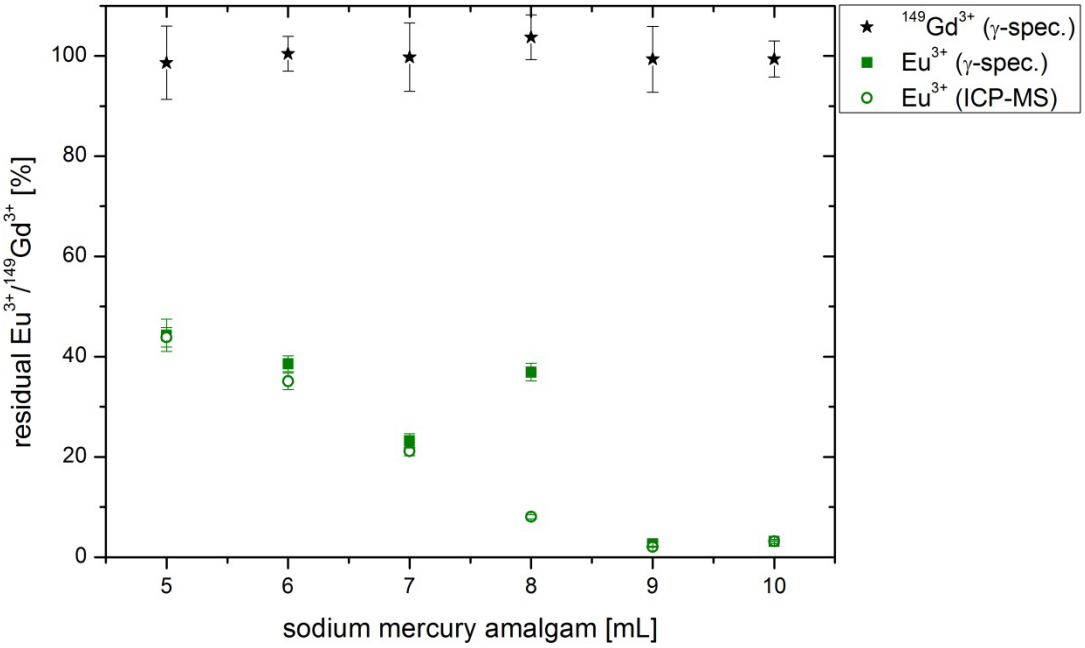

Figure 31: Extraction yield of macroscopic europium and ^{149}Gd in dependence of varying sodium mercury amalgam volumes in percent.

With a europium content of 431 mg Eu^{3+} to be extracted, an excess Eu:Na ratio of 1.25 was achieved. However, only approx. 98 % of europium was extracted into the amalgam with a residual Eu^{3+} content of 9 – 12 mg in the solution.

An extraction dependence on the reaction time was assumed as a possible reason for the incomplete reduction of europium. Hence, the kinetic influence was examined with the optimised parameters of Denzler et al.[78] for a 500 mg Eu_2O_3 pellet.

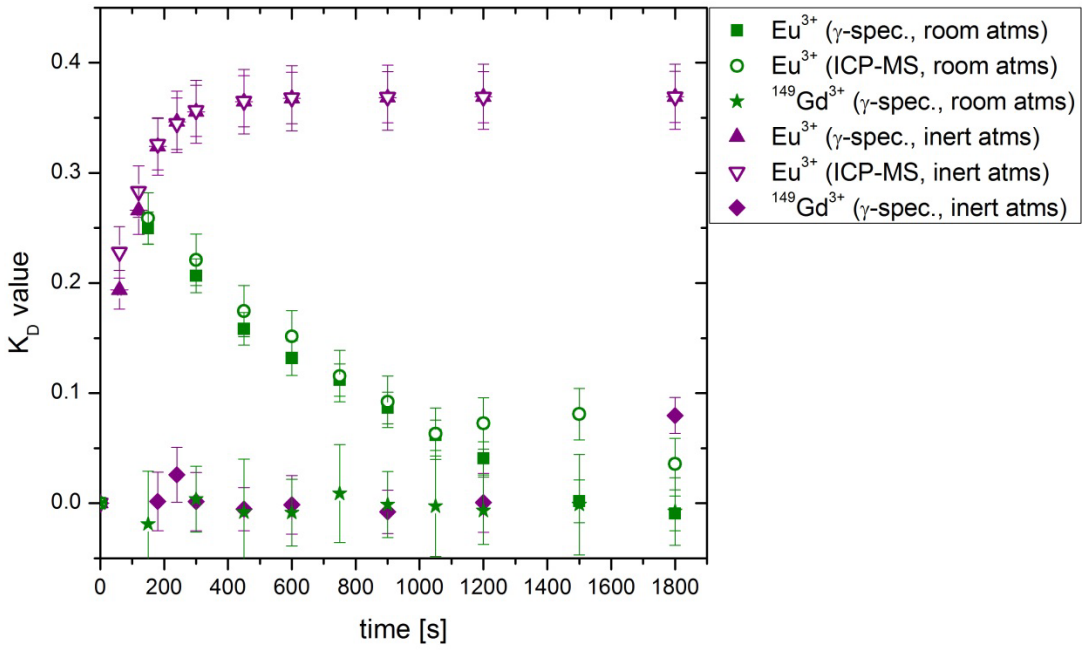

Figure 32: Distribution coefficients of the kinetic extraction behaviour of europium within the course of 30 min with and without the exclusion of air.

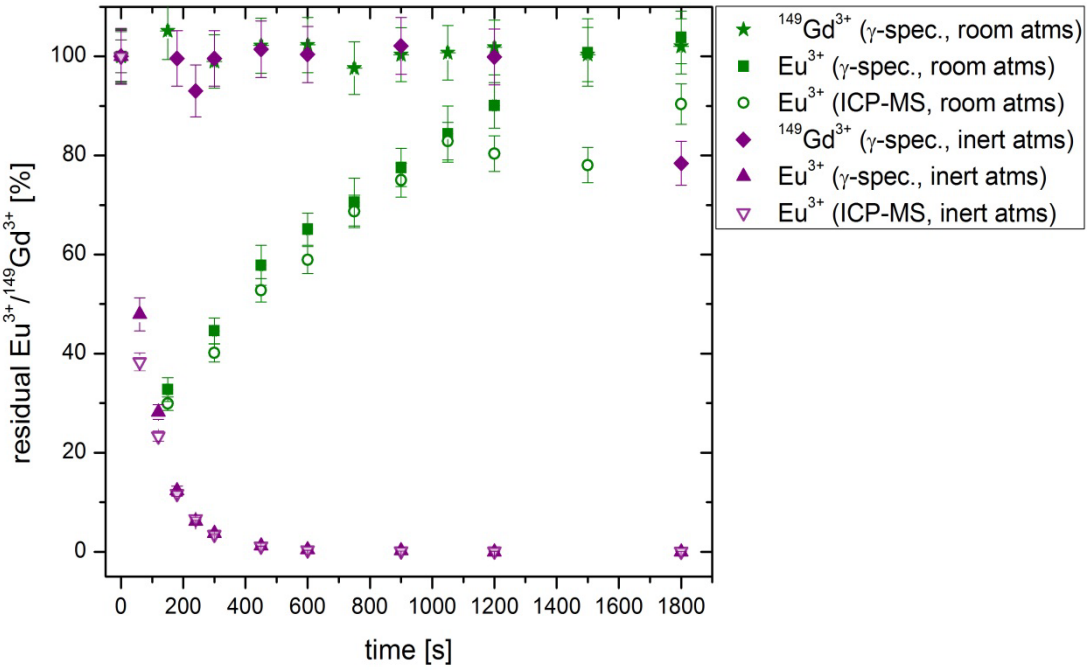

Figure 33: Kinetic extraction yield of macroscopic europium and ^{149}Gd within the course of 30 min with and without exclusion of air given in percent.

The extraction behaviour at different time intervals is depicted in Figures 32 and 33. Within the first few minutes of the extraction under room atmosphere the europium content in solution decreases rapidly to 33 % (141 mg Eu^{3+}), but increases afterwards back up to the starting concentrations. This phenomenon can be clearly attributed to the re-oxidation of elemental europium by oxygen dissolved in the solution. The gadolinium content stays more or less at maximum levels and negative values of the distribution coefficients are caused by measurement uncertainties.

When the kinetic extraction behaviour was investigated employing 10 mL amalgam under inert atmosphere and after 15 min argon purge in an ultrasonic bath to remove oxygen solved in the solution, the re-oxidation was strongly reduced (also see Figures 32 and 33).

This way the europium content in the solution can be reduced to 0.09 % (0.4 mg Eu^{3+}) after 20 min without noticeable reduction of radiogadolinium activity. A further reduction of the europium content down to tracer levels may be possible by use of oxygen scavengers like Cr^{2+}. However, the introduction of additional metal ions would complicate the system immensely and would render it unsuitable for a quick and facile separation of radio-gadolinium.

In summary, this extraction method can be used as an effective way to remove macroscopic amounts of europium in order to prepare a precursor for a quantitative Gd separation, for example with a specialised extraction resin, like TRU[107] (Triskem), with a low capacity. In case of labelling a standard MRT contrast agent in order to show the application of $^{147/149}$Gd, the separation is sufficient, due to the analogous chemical complex behaviour of europium

and gadolinium. The low amounts of inactive europium should not interfere *in vivo*. A more detailed discussion about the *in/ex vivo* behaviour is given in chapter 4.3.3.

4.3 Preparation of $^{147/149}$Gd DOTA and its *in* and *ex vivo* comparison

Gd-DOTA was synthesised with two different methods as assessment for the suitability of the separation and the applicability of $^{147/149}$Gd as a MRT contrast marker. The *in vivo* stability of the complex was tested in PBS and HBS. Also, a distribution comparison of an inactive MR contrast agent and its labelled analogue in the brain of a tumour bearing rat was carried out. The *in vivo* images of the rat brain taken by a 3T MRI scanner were compared to the *ex vivo* images prepared by autoradiography.

4.3.1 Separation of Na and $^{147/149}$Gd

The bulk amount of europium was removed by the amalgam separation procedure described in the previous chapter. Additionally, the sodium, chloride and acetate content in the solution had to be drastically reduced prior to stability tests and an *in vivo* injection. This was necessary to achieve a suitable small volume and to assure an analogous model for the measurements of the commercial and synthesised compound. A chromatographic column extraction with the DGA normal resin was used for the removal of excess sodium, chloride and acetate ions.

The capacity and distribution factors of several elements on the extraction resin DGA normal were measured in different media by Horwitz et al.[107]. They determined a log K_D of >3 and >4 in nitric acid for europium and gadolinium, respectively, while sodium was not adsorbed at all. In 0.1 M hydrochloric acid the log K_D values were approx. 0.5 for both Eu and Gd. Therefore, an elution with 1 M nitric acid should lead to a concentration of the Eu/$^{147/149}$Gd mixture on the column and an elution of sodium, chloride and acetate simultaneously. Horwitz et al.[107] also suggested a simultaneous separation method for 33 elements, however, no separation of europium and gadolinium was observed.

Hence, the separation was simplified and focused on the separation of sodium from both lanthanides using a DGA normal column. After the solvent change from 1 M nitric acid to 0.1 M hydrochloric acid, about 87.4 % of the starting activity of ^{149}Gd was eluted in approx. 17.0 mL of it.

Approx. 12.6 % of the starting Gd radioactivity is lost in solution transfers between different containers or glass ware of the amalgam procedure and the DGA separation. Yet, the yield was still high enough for the subsequent tasks and no transfer optimization was necessary. The fractions containing radioactivity were united and evaporated to dryness. A different

eluent may lead to smaller volumes containing the Gd, but the radioactive fractions evaporated within 1-3 h so that no additional optimization was necessary. Only a slight residue of presumably Eu or Na salt was observed after the evaporation of the solvent. However, the mass of the residue was within the weighing uncertainty of the available balance (± 0.1mg) and the residue used without further purification. It easily resolved in a minimal solvent volume of at least 0.5 mL.

4.3.2 $^{147/149}$Gd DOTA complex synthesis and stability tests

Two previously described synthesis routes[126, 127] for the n.c.a and c.a. $^{147/149}$Gd labelling of DOTA were tested. The conditions and results of the complexing tests performed in this thesis are summarised in Table 16.

Table 16: Reaction conditions, reaction time and yields for Gd-DOTA synthesis

Solution	pH	Carrier	Reaction time [min]	Temperature [°C]	Radio TLC yield [%]
0.1 M NaOAc	5,0	n.c.a.	1440	40	>99
1 M NaOAc	5,6	n.c.a.	5	90	>99
1 M NaOAc	5,6	n.c.a.	20	90	>99
1 M NaOAc	5,6	0.1 eq	5	90	>99
1 M NaOAc	5,6	0.1 eq	20	90	>99

The first tested synthesis route by Vanasschen et al.[126] was chosen for its low reaction temperature and therefore mild reaction conditions. It was confirmed by TLC that the chemical reaction was quantitative. Unfortunately, the reaction time of 24 h was rather long and about 36 % of the starting radioactivity of ^{147}Gd decayed during the DOTA complexation. An alternative synthesis was found in literature[127] with harsher temperature conditions of 90°C but a significantly shorter reaction time of 20 min. The synthesis was originally designed for the DOTA complexation of the $^{44}Sc^{3+}$ ion. The chemistry of Sc(III) and Gd(III) are rather similar, due to the lanthanide contraction. Therefore, it was not farfetched to assume similar complexation behaviour with DOTA. The results of the synthesis confirmed this assumption. A reaction time of 5 min was sufficient to complete the reaction with no precursor present in solution which was confirmed by radio TLC. The temperature test showed that even after 20 min at 90°C the complex was still intact and no precursor or free Gd^{3+} ions were detected by radio TLC. Accordingly, a quantitative reaction was achieved here within 5 min which is considerable shorter than the previously followed concept of Vanasschen et al.[126] The same quantitative reaction within 5 min was observed with 0.1 eq. inactive Gd carrier.

The stability of the synthesised complex was examined to exclude distribution deviations caused by free Gd(III) in the *in vivo* comparison to DOTArem™. The stability was previously tested in a phosphate buffered saline (PBS) to check for possible ion exchange between the solution and the complex. Subsequently, the complex was further tested in human blood serum (HBS) at 37°C to simulate *in vivo* conditions as best as possible. The HBS of four different donors was pooled to exclude possible unique behaviour of a single sample. The results of the stability tests in PBS and HBS are listed in Table 17 and an exemplary TLC instant imager measurement is depicted in Figure 34.

Table 17: Results of the c.a. and n.c.a. stability tests with $^{147/149}$Gd-DOTA in PBS and HBS at 37°C.

Solution	Carrier	Incubation time [h]	Stable complex [%]
HBS	c.a.	56	>99
HBS	c.a.	144	>99
HBS	n.c.a.	56	>99
HBS	n.c.a.	144	>99
PBS	n.c.a.	24	>99

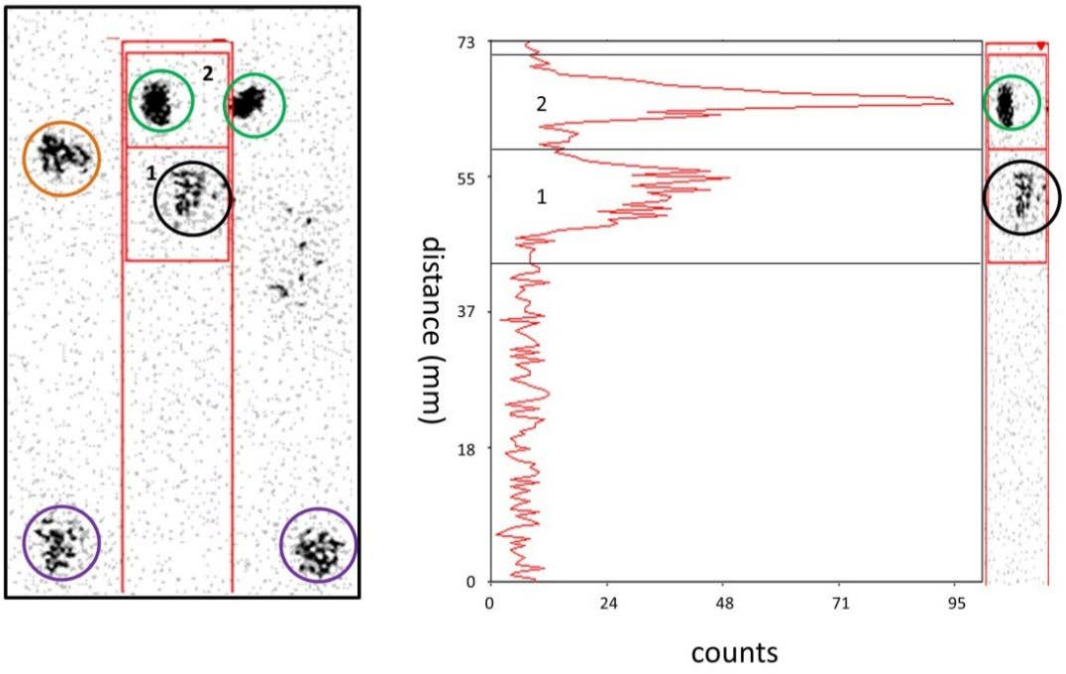

Figure 34: Instant Imager measurement of a TLC plate with Gd-DOTA after a 6 d incubation time in HBS (left) and corresponding radioactivity profile of the red stripe (right). Depicted circles are the reference points (green), the TLC start line ref. point (purple), the TLC end line ref. point (orange), and the ^{147,149}Gd-DOTA complex (black).

The reference spots on the TLC plate (green, orange, purple circles) were marked after the separation and were used for "orientation purposes" in the Instant Imager.

No de-complexation of n.c.a. or c.a. Gd-DOTA was observed with TLC measurements in the PBS solution in a time period of 24 h or in the HBS solution in time periods of 56 h and 144 h. As indicated by its high thermodynamic stability constant ($>10^{24}$) determined from measurements in water by Cacheris et al.[143], the complex shows sufficient chemical inertness in HBS. The radiochemical equivalence of this synthesised $^{147/149}$Gd-DOTA is thereby proven to be the same as the commercially available Gd-DOTA complex DOTArem™. The enzymatic metabolization of the complex is chemically very unlikely because all acetic acid groups of DOTA are bound to the central Gd ion and no vantage point is exposed for enzymatic cleaving.

4.3.3 Comparison of *in* and *ex vivo* imaging of the $^{147/149}$Gd DOTA complex and commercial DOTArem™

For first comparison experiments the *in vivo* distribution of the contrast agent DOTArem™ was measured by MRI in a tumour bearing F98 rat model. One day later the here prepared $^{147/149}$Gd-DOTA was injected, the rat sacrificed, brain sections prepared and measured with autoradiography as described in chapter 3.4.3. A histology of the neighbouring brain sections was done with the dye DAPI (4',6-diamindino-2-phenylindole). Some of these coronal brain sections of the tumour area are depicted in Figures 35 and 36.

In the autoradiographic measurements the radioactivity distribution of $^{147/149}$Gd is shown (left column in Figures 35 and 36). The histological staining with the fluorescence marker DAPI shown in the middle column displays the DNA in cell nuclei and therefore the cell density. Denser tissues, like the implanted tumour cells, appear darker in the staining than normal brain tissue or brain liquor.

The MRI sections are the subtraction of images measured before and after an injection of the contrast agent. The difference in contrast is depicted in white. A perfect mapping of the MRI images onto the brain sections is not possible because the size of the brain is different in each method. While the shape of the brain is fixed by the cranial bone in the MRI *in vivo* measurements, it is strongly deformed after its extraction in the *ex vivo* histology or autoradiography. This distortion is most likely caused by the tumour, leading to a larger right hemisphere. In the comparison of the different imaging techniques, this leads to a problematic localisation of the MR sections in relation to the coronal orientation of the histological and autoradiographical images. An approximate localisation can be done with the help of characteristic anatomical structures. However, in the present case those are mostly not significant enough to achieve a perfect match for each section. The identified details,

however, are sufficient for a close assignment and comparison of most sections. Due to this and the limited number of experiment repetitions all stated interpretations are highly preliminary and still in need of confirmation by further testing.

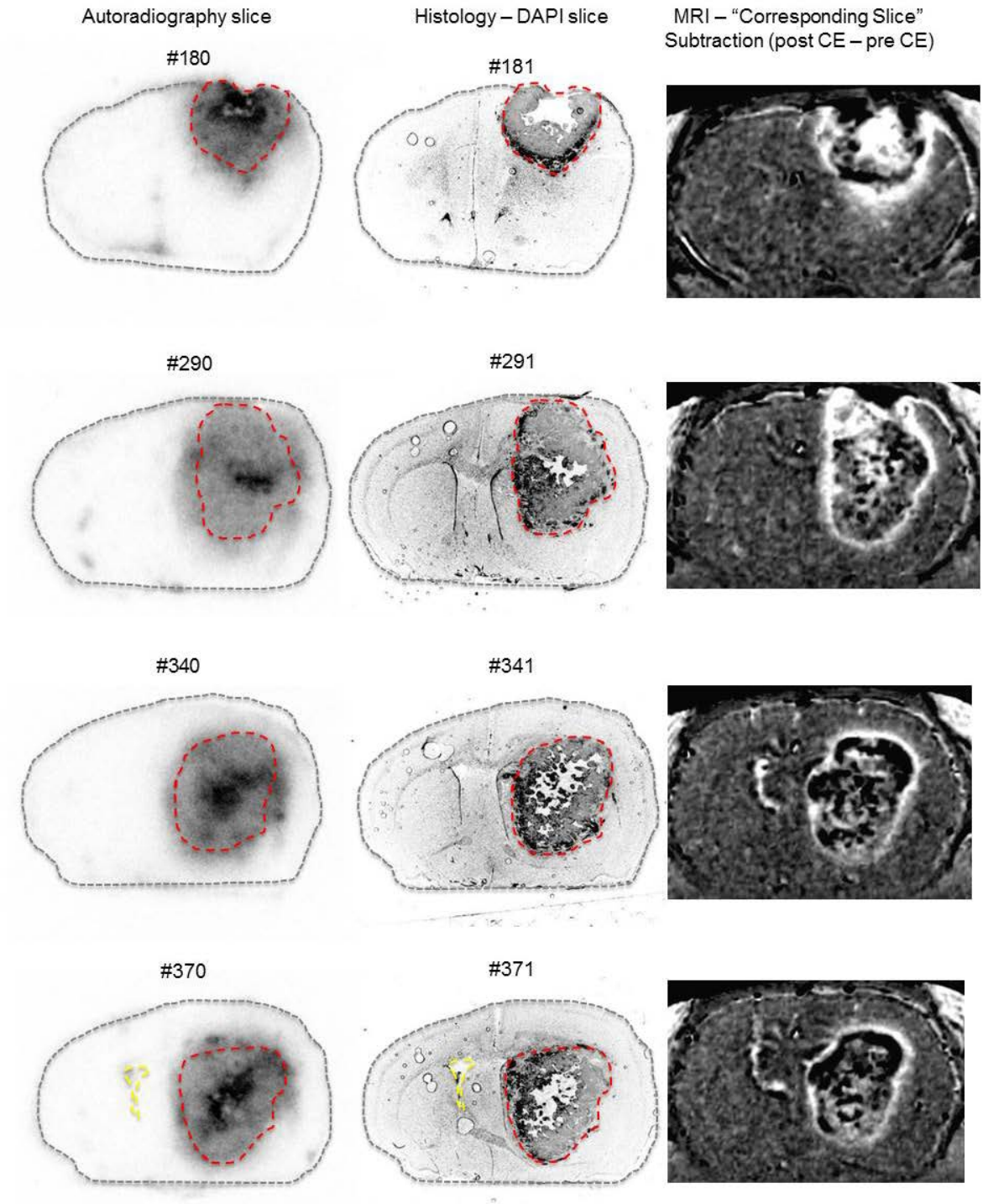

Figure 35: Coronal autoradiographic (left side), histologic (middle) and magnet resonance sections (right side) of the rat brain after the successive administration of n.c.a. $^{147/149}$Gd-DOTA (ARG) and commercial DOTArem™ (MRI) with the tumour tissue marked red and the lateral ventricles marked yellow.

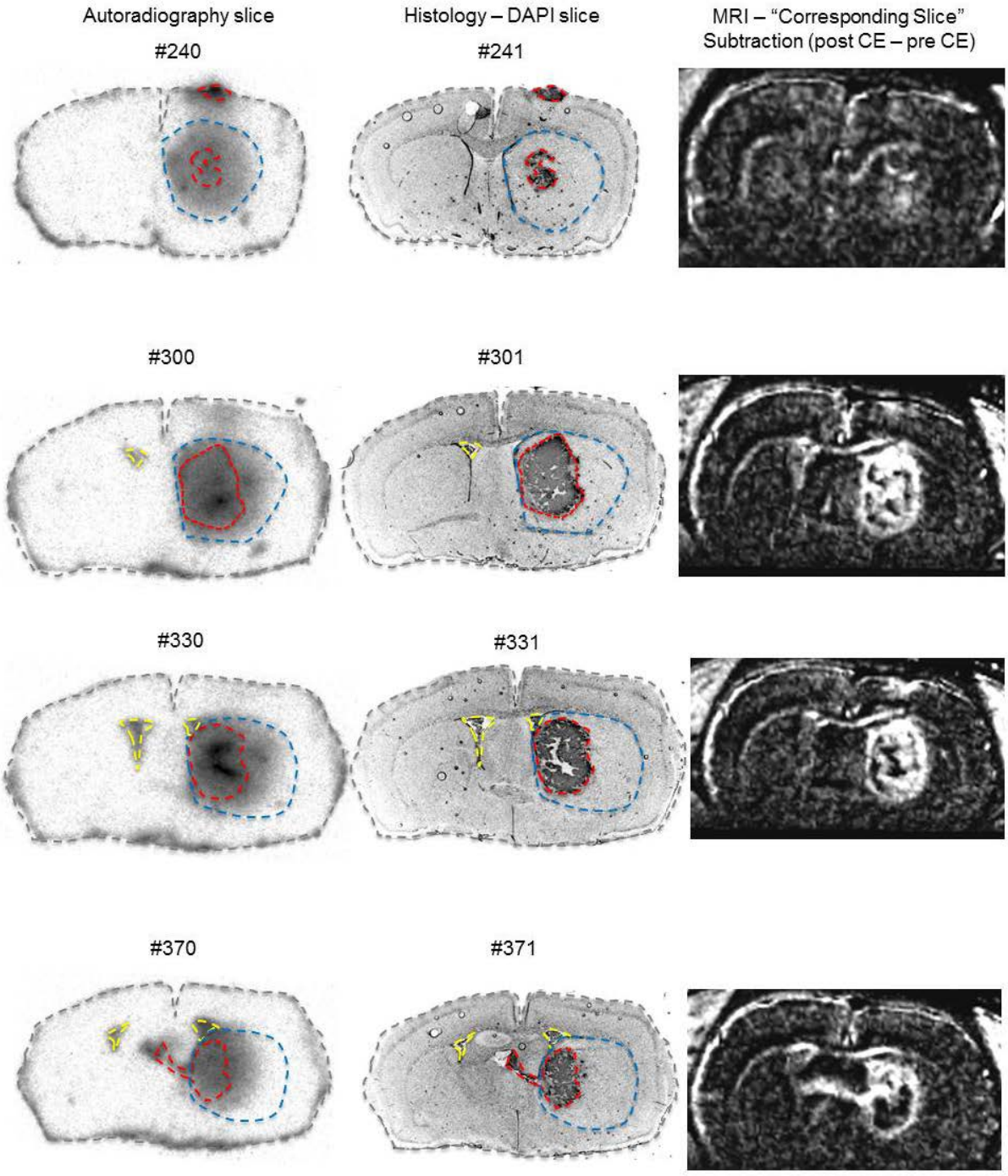

Figure 36: Coronal autoradiographic (left side), histologic (middle) and magnet resonance sections (right side) of the rat brain after the successive administration of c.a. $^{147/149}$Gd-DOTA (ARG) or commercial DOTArem™ (MRI) with the tumour tissue marked red, the lateral ventricles marked yellow and the right hemispheric striatum labelled blue.

The n.c.a. $^{147/149}$Gd-DOTA experiment was done 14 days after the implantation of the F98 tumour cells and the tumour was considerably larger than in the c.a. $^{147/149}$Gd-DOTA experiment which was conducted 8 days after implantation. The tumour dimensions of the

histological staining were marked red in the images and these markings were transferred to the autoradiography sections. The dimensions of the radioactivity distribution, the histological staining as well as the tumour tissue shown by the MR images of the n.c.a. $^{147/149}$Gd-DOTA experiment correspond with each other and only smaller deviations occur which might be explained by freezing and fixating the sections.

But, before any comparison of the non-radioactive and radioactive compounds can be discussed, it has to be stated that the Gd complex with DOTA exhibits a purely unspecific behaviour in the brain and cannot cross the intact blood brain barrier. An accumulation can only occur if the blood brain barrier is disturbed and an enhanced permeability and retention effect is present in the tissue. This is the case for most brain tumours. Another accumulation site beside the brain tissue is the choroid plexus in the ventricle system and every region with a significant high abundance of blood.

This in mind, all three methods were successful in giving an approximate localization of the implanted tumour cells in both experiments. They reveal different fine structures of the brain and the tumour tissue and also show a deviating accumulation of the contrast agent. The differences which will be discussed in more detail are the accumulation in the central tumour regions and the highly metabolically active border regions as well as the difference in the general size of the tumour between the three imaging methods.

At first the fine structures show an interesting difference in the central region of the tumour (see Figure 35). The used F98 glioma cells grow considerably faster than new blood vessels can be constructed from the body to sustain the tumour cells, leading to necrotic tissue. When the tumour grows further, this necrotic tissue is encapsulated preventing any blood supply. Only the outer regions of such fast growing tumours are highly metabolically active and supplied with blood. Thus, the outer regions typically show the highest contrast in MRI which is additionally enhanced in the living animal by the increased amount of blood in the border region of the tumour. This is seen in the histological staining as well, because no living cells with DNA are left in the necrotic regions.

In this study, however, autoradiographic measurements show an accumulation of radioactivity in these necrotic regions in the centre of the tumour. This implicates a high concentration of contrast agent in the necrotic tissue which cannot be seen in the MRI images. The observed deviation between MRI images and autoradiographic measurements may be caused by an increasing magnetic susceptibility in the tissue which is induced by a rising concentration of T_1 contrast agent leading to the annihilating of the positive T_1 contrast by the negative T_2^* contrast above a certain contrast agent concentration.[144]

Even though the cause for the deviation of MRI and autoradiography might thus be understood, the reason for the accumulation of the contrast agent in the necrotic region

cannot be explained yet. A uniform background radiation could be caused by diffusion of the compound, but an accumulation is contrary to the previously observed behaviour of glioma. Also, the accumulation can not be caused by the unlikely decomposition of the Gd-DOTA ligand because free $^{147/149}Gd^{3+}$ ions cannot reach the necrotic regions. Thus, no conclusive explanation can be given thus far, and further studies are needed to explain the mismatch.

Another difference is evident at the highly metabolically active border regions of the glioma. While a strong contrast change is observed in the MR sections, no accumulation can be seen in the autoradiograms. This can be based upon the unspecific nature of Gd-DOTA and the contrast enhancement originating from the blood in the blood vessels. On the one hand, no trapping of the contrast agent occurs in the tumour cells due to the disrupted blood brain barrier. After death of the rat the compound can diffuse into the surrounding tissue over time. The preparation of the sections and the acquisition of the autoradiograms took long enough for this phenomenon to occur. On the other hand, the preparation of the brain slices was done by shock freezing the brain only after its removal from the animal. Therefore, the blood with the excess of contrast agent probably has drained from the brain and the tissue shows a much lower accumulation of $^{147/149}$Gd-DOTA than *in vivo*. It can be assumed that these artefacts are additionally amplified by the considerable higher detection limit of autoradiography in comparison with MRI. This effect can also be seen in the c.a. $^{147/149}$Gd-DOTA experiments.

Completely similar histological and magnetic resonance images are obtained in the brain sections after the administration of c.a. $^{147/149}$Gd-DOTA (see Figure 36). For all three methods the same distribution of contrast agent is seen in the plexus coroideous, lateral ventricles (yellow) as well as at the implantation point of the glioma cells (red). In contrast to this, the radioactivity distribution in the region of the main tumour is considerably larger than the tumour tissue depicted by the histology or MR. The radioactivity is distributed nearly uniformly in the complete striatum which is marked blue for reference in Figure 36. A minor blurring of the autoradiogram is to be expected due to the γ-rays of ^{149}Gd with higher energies. But as mentioned above, the most likely explanation for this is the combination of the different detection limits and the diffusion of contrast agent from the glioma into the striatum after the death of the rat.

The limitation of the radioactivity within the striatum is most probably caused by the detachment of the striatum from the rest of the brain by the corpus callosum and the ventricle system. This explanation might be supported by the structures seen in brain section #370 and #371 in Figure 36. It is possible that a small part of the glioma has grown into the striatum on the left hemisphere of the rat brain. The diffusion of the contrast agent is hindered by the separation of the striatum from the rest of the brain except for the leakage at

the metastasised tumour cells growing to the left hemisphere. In the left hemisphere the start of the diffusion originating from the tumour cells is seen. Another explanation for the observed structure in the brain section #370 and #371 could also be the right interventricular foramen which is displaced in the strong distortion of the brain by the expanding tumour.

Either way the diffusion artefact depicted with the higher detection sensitivity of the autoradiography and the artefact induced by the absence of blood seem to be the basic problems of the measurement arrangement in the *ex vivo* comparison of the commercial DOTArem™ contrast agent and the synthesised $^{147/149}$Gd-DOTA. It is unlikely that other effects exist which would influence the distribution of the applied chemically identical compounds. Hence, the used method seems not to be applicable for a conclusive comparison of the distribution of radioactive and non-radioactive Gd-complexes.

One solution may be shock freezing the whole animal before the brain is removed and therewith preserving the original blood distribution. Another solution of the distribution deviations between *in* and *ex vivo* measurements could be the subsequent *in vivo* imaging with SPECT and MRI with the same contrast agent cocktail. The great disadvantage of this would be the lower spatial resolution achieved with small animal SPECT scanners of 0.5 - 2 mm in comparison to 50 – 100 µm with autoradiography.[37] The advantage is the avoidance of possible artefacts by dissection, freezing and cutting the brain in sections as well as diffusion of the compound until the autoradiogram is performed.

Additionally, while Gd is momentarily the most used element in contrast agents in MRI, the use of the new PET/MRI hybrid scanners may tip the scales towards new bi-modal probes based on the Gd alternate Mn(II). This would allow a simultaneous *in vivo* evaluation with both modalities, if a PET suitable radiomanganese isotope is at disposal.

4.4 Production of n.c.a. ^{52g}Mn

Given the emerging combination of PET and MRI scanners as well as emerging bi-modal probes, the radioisotopes of manganese suitable for PET measurements, namely ^{51,52g}Mn, and their production routes have to be re-evaluated. Cross sections of the promising proton induced reactions on natural chromium leading to ^{52g}Mn have been measured earlier [62-65, 67, 68, 70, 145] and indicate an optimal production energy range at the maximum of the excitation function between 5 and 20 MeV (see Figure 4). While the cross sections of said reaction have been adequately measured, data on the production rates or thick target yields are only scarcely available.[69, 146, 147] In addition, more suitable separation methods have to be developed to establish a reliable supply of highly radionuclidically pure radiomanganese for those purposes.

4.4.1 Integral yields and experimental thick target yields

All production rates (TTY_{prod}), derived saturation thick target yields (TTY_{sat}) and theoretically assessed integral yields ($IntY_{prod/sat}$) covering the maximum of the excitation function of the ^{nat}Cr(p,x)^{52g,m}Mn reaction were measured and calculated as described in chapter 3.2.5 and are shown in Table 18. Additionally, the integral yields of ^{52g,m}Mn are depicted in Figure 37. Some TTYs found in the literature are listed in Table 19. These were arithmetically converted into the TTY_{sat} in GBq/μA for comparison as described by equation 16.

Table 18: Experimental production rates, calculated saturation thick target yields and respective integral yields of main radioisotopes produced.

Isotopes	E_P = 16.9 → 8.2 MeV			
	TTY_{prod} [MBq·μA^{-1}·h^{-1}]	$IntY_{prod}$ [MBq·μA^{-1}·h^{-1}]	TTY_{sat} [GBq·μA^{-1}]	$IntY_{sat}$ [GBq·μA^{-1}]
^{52g}Mn	13.1 ± 1.6	13.7 ± 1.6	2.55 ± 0.31	2.74 ± 0.30
^{52m}Mn	5990 ± 490	6910 ± 760	6.96 ± 0.57	8.03 ± 0.88
^{51}Cr	1.60 ± 0.16	1.73 ± 0.19	1.53 ± 0.15	1.66 ± 0.18

Table 19: Literature thick target yields converted to saturation yields.

Isot.	TTY_{sat} [GBq·μA^{-1}]		
	Muminov[69] (12 MeV → threshold)	Abe[147] (16 MeV → threshold)	Dmitriev[146] (22 MeV → threshold)
^{52g}Mn	-	0.98	4.07 ± 0.47
^{52m}Mn	7.25	-	-
^{51}Cr	-	-	5.66 ± 0.67

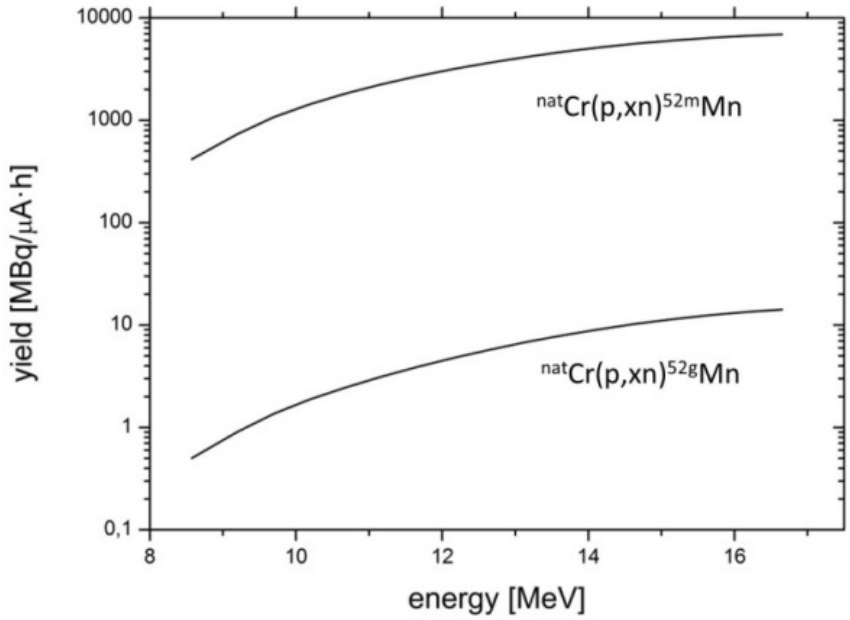

Figure 37: Integral yield curves of ^{52g,m}Mn.

The measured cumulative saturation yields in the proton energy range of 16.9 to 8.2 MeV amount to 2.55 ± 0.31 and 6.96 ± 0.57 GBq/μA for the ground state and the metastable state of ^{52}Mn, respectively. With these new experimental data the activity contribution of the metastable state to the ground state was calculated to approximately 4.7 % in a saturated thick target. The calculated integral saturation yields of ^{52g}Mn and ^{52m}Mn are approx. 0.19 GBq/μA (8 %) and 1.07 GBq/μA (15 %) higher than the experimentally determined yields, representing acceptable variances within one standard deviation for ^{52g}Mn and two standard deviations for ^{52m}Mn. This variance is analogous to the experimental yield diminution in the thick target measurements with radiogadolinium discussed in chapter 4.1.5. Again, in comparison to the integral yields a reduction of 5-30 % for the experimental yields is to be expected due to the earlier mentioned experimental artefacts, e.g. thermal effects, which influence the actual area weight among others.

In the literature, only one determination of the thick target yield for ^{52g}Mn (16 → threshold) exists from Abe et al.[147] for the optimal proton energy production range (0.98 GBq/μA)[147]. This is only 38.5 % of the experimental result and 36.6 % of the theoretical calculation found in this study here. No details about the process of yield calculation, efficiency calibration, γ-rays used for radioactivity calculation or their exact branching ratios are given by Abe et al.[147]. Therefore, no scientifically justified reason for this deviation can be given. Other reported thick target yields are either covering a too narrow (12 MeV → threshold[69]) or a too large energy region (22 MeV → threshold[146]), where more radioactive impurities (e.g.

^{48,49,51}Cr) are produced. Therefore, a comparison of the measured data with those literature values is not seriously possible.

In conclusion, the irradiation of a natural chromium disk is sufficient for laboratory scale separation tests, subsequent synthesis and initial PET studies. The shorter lived isotope ^{52m}Mn decays too quickly into ^{52g}Mn (1.75 %) and ^{52}Cr (98.25 %) before further experiments can be performed. The longer-living chromium impurities will be removed together with the macroscopic amount of target material. However, irradiations for more sophisticated *in vivo* PET studies should be done with enriched ^{52}Cr targets to minimise isotopic impurities by ^{51,54}Mn. The investigation of these co-products was not part of this work, because for the development of a radiochemical separation ^{51}Mn decayed too fast with a half-life of 46.2 min while the production of ^{54}Mn was too low to be detected in presence of ^{52g}Mn and was therefore not interfering.

4.4.2 Optimised radiochemical separation

A number of different methods for the separation of manganese and chromium have been reported in literature so far.[148-150] Unfortunately, none of them is directly suitable for an authentic radiolabelling of MR contrast agents, because of the carrier used, too long separation times, a problematic transfer into an automated system or a chemical form, unfavourable for the subsequent synthesis steps.

As mentioned in chapter 3.5, a separation of Mn from Cr was previously developed[65] which eliminates most of the problematic disadvantages of the available separation procedures. In this separation an irradiated chromium target was dissolved in fuming hydrochloric acid and separated by ion-exchange chromatography, utilizing DOWEX 50WX8 and 0.067 M ammonia citrate solution (pH 7.2) for elution of manganese. Unfortunately, a complete removal of chloride ions is absolutely mandatory for the chromatographic step of the separation. The time consuming removal is quite impractical considering that the chromium is dissolved in hydrochloric acid and the resulting product needs to be converted into $MnCl_2$ for further processing. Additionally, the volume of the eluted radiomanganese is rather large with 10 – 15 mL. Russel et al.[130] suggested a different n.c.a. chromatographic separation method, which uses oxalic acid as eluent for Cr and 1 M HCl for the elution of radiomanganese. The separation was originally designed for the separation of ^{54}Mn from macroscopic amounts of Cr, but should be easily adaptable for ^{52}Mn. Therefore, the separation was carried out according to the described procedure (see chapter 3.5.2) and the separation parameters were optimised aiming at a more suitable separation of ^{52}Mn from Cr. The elution profile of this separation is depicted in Figure 38.

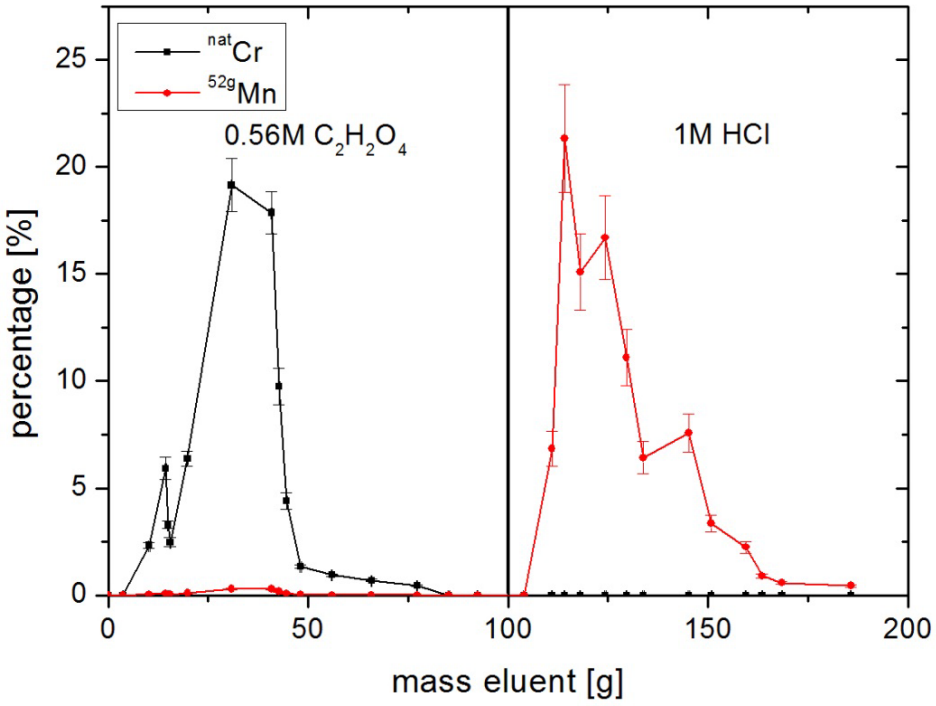

Figure 38: Elution profile of the *Mn separation from Cr taken from Russel et al.[130] (resin: Amberlite IR120, Cr eluent: 0.56M oxalic acid, Mn eluent: 1 M HCl)

The elution profile shows a clearly separated Cr as well as a ^{52}Mn fraction of approx. 75 mL volume with an additional small loss of approx. 1.2 % of starting ^{52}Mn radioactivity in the Cr fractions. A small amount of Cr (<1 %) is absorbed on the column and eluted in the Mn fractions, unless a large amount of oxalic acid is used for the elution of Cr or a successive repetition of the separation procedure is performed. The original separation procedure is not optimal due to the far too large volume of the eluent fractions of both Cr and Mn which is impractical for a subsequent radiolabelling. Therefore, the parameters of the separation were further changed.

The loading solution was reduced from 50 mL 5 % oxalic acid to 5 mL 1 % oxalic acid to achieve smaller chromium fractions for more efficient reprocessing of the target material. The resin was changed from Amberlite IR120 to DOWEX 50WX8, due to availability reasons. The column temperature was increased to 80°C, enhancing the elution, in order to obtain smaller chromium and manganese fractions. The column dimension was increased for reduction of manganese break through. The elution profile of the resulting optimised separation thus developed is depicted in Figure 39.

Even yet, with optimised parameters a small amount of approx. 1.4 % radiomanganese was still lost in the chromium fractions, and it was found that the adsorption of the Cr on the column is strongly dependent on the residual chloride concentration from the solvation of the elemental chromium target. The addition of 0.05 to 0.15 M hydrochloric acid leads to a

complete Cr elution with the necessary concentration depending on the employed Cr mass. However, the concentration window of added hydrochloric acid is rather small, since a concentration above 0.2 M HCl will already lead to a substantial manganese breakthrough. Lower concentrations are leading to Cr impurities within the manganese fractions. Because of this strong dependence on the hydrochloric acid concentration for the complete elution of chromium, a simple translation of the separation procedure for varying chromium masses is not possible. For this, the separation method is too complex and not favourable.

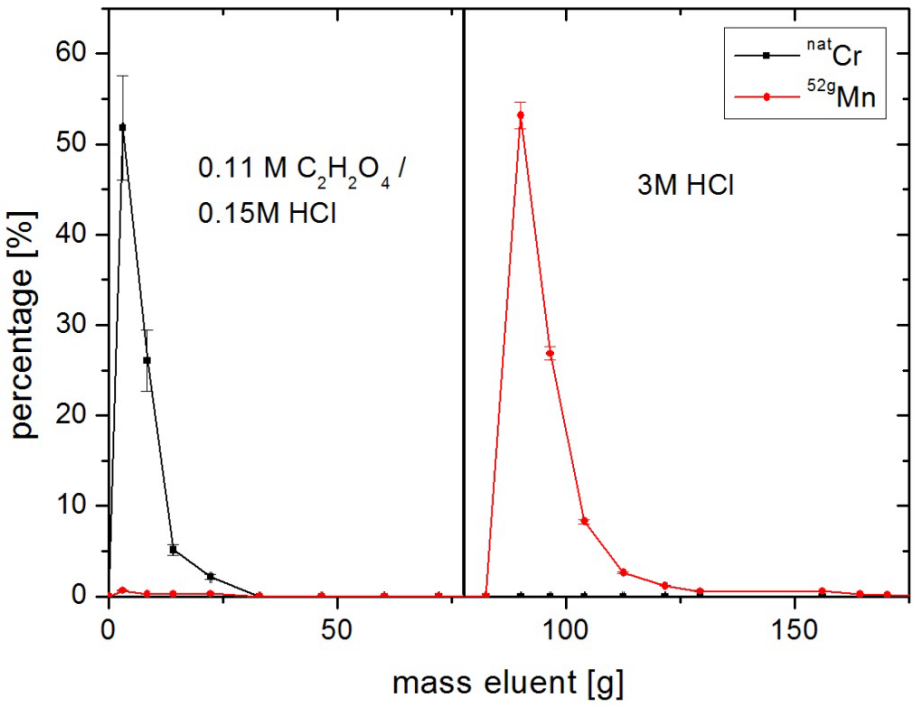

Figure 39: Elution profile of a *Mn separation from Cr with optimised parameters (resin: DOWEX 50WX8, Cr eluent: 0.11M oxalic acid / 0.15 M HCl, Mn eluent: 3M HCl, T=80°C).

Another separation method investigated was based on the selective extraction of chromium from an ion exchange resin by an organic extractant. A suitable one for the selective extraction of trivalent ions is di-(2-ethylhexyl)phosphoric acid (HDEHP) which is also used in the DAPEX[151] procedure for uranium extraction. Distribution coefficients were measured for varying concentrations of HDEHP in EtOH with an anion and cation exchange resin after a 1 h and a 72 h equilibration time period. The resulting K_D-values and separation factors (SF) are summarised in Table 20.

Table 20: K_D and SF values of ^{51}Cr, ^{52}Mn in different solutions. Bold marked solution combinations were used in column separations discussed below.

Resin / incub. time	Solution	K_D ^{51}Cr	K_D ^{52}Mn	SF $^{52}Mn/^{51}Cr$
DOW. 50WX8 / 1 h	2.2 % HDEHP / 97.8 % EtOH	9.0 ± 2.6	1335 ± 138	149 ± 15
DOW. 50WX8 / 1 h	4.4 % HDEHP / 96.6 % EtOH	9.2 ± 2.6	746 ± 77	81 ± 8
DOW. 50WX8 / 1 h	6.6 % HDEHP / 93.4 % EtOH	7.5 ± 2.5	790 ± 82	106 ± 11
DOW. 50WX8 / 1 h	8.8 % HDEHP / 91.2 % EtOH	5.1 ± 2.3	691 ± 72	137 ± 14
DOW. 50WX8 / 72 h	2.2 % HDEHP / 97.8 % EtOH	14.8 ± 2.3	1916 ± 186	129 ± 13
DOW. 50WX8 / 72 h	4.4 % HDEHP / 96.6 % EtOH	11.6 ± 2.1	1541 ± 150	133 ± 13
DOW. 50WX8 / 72 h	6.6 % HDEHP / 93.4 % EtOH	9.7 ± 2.0	1378 ± 134	143 ± 14
DOW. 50WX8 / 72 h	8.8 % HDEHP / 91.2 % EtOH	6.7 ± 1.9	1330 ± 129	197 ± 19
Amb. CG 400 / 1 h	0 % HDEHP / 100 % EtOH	1.1 ± 1.7	506 ± 47	460 ± 43
Amb. CG 400 / 1 h	0.25 % HDEHP / 99.75 % EtOH	2.2 ± 2.2	796 ± 59	358 ± 27
Amb. CG 400 / 1 h	0.5 % HDEHP / 99.5 % EtOH	0.91 ± 1.70	461 ± 43	508 ± 48
Amb. CG 400 / 1 h	1 % HDEHP / 99 % EtOH	2.3 ± 2.1	671 ± 50	291 ± 22
Amb. CG 400 / 1 h	2.2 % HDEHP / 97.8 % EtOH	0.77 ± 1.70	418 ± 55	544 ± 72
Amb. CG 400 / 1 h	4.4 % HDEHP / 96.6 % EtOH	2.5 ± 1.8	577 ± 76	235 ± 31
Amb. CG 400 / 1 h	6.6 % HDEHP / 93.4 % EtOH	2.0 ± 1.8	490 ± 65	242 ± 32
Amb. CG 400 / 1 h	8.8 % HDEHP / 91.2 % EtOH	2.1 ± 1.8	700 ± 92	338 ± 44

Table 20 cont.

Resin / incub. time	Solution	K_D ^{51}Cr	K_D ^{52}Mn	SF $^{52}Mn/^{51}Cr$
Amb. CG400 / 1 h	**MeOH**	**-0.22 ± 0.59**	**154 ± 24**	**1537 ± 244**
Amb. CG400 / 1 h	EtOH	1.4 ± 1.1	329 ± 34	239 ± 25
Amb. CG400 / 1 h	iPrOH	-0.26 ± 1.00	24.3 ± 3.1	243 ± 31
Amb. CG400 / 1 h	BuOH	-0.051 ± 0.601	56.7 ± 9.6	567 ± 96
Amb. CG400 / 1 h	1 % HCl / 99 % MeOH	0.36 ± 0.61	141 ± 23	395 ± 63
Amb. CG400 / 1 h	5 % HCl / 80 % MeOH	2.2 ± 0.7	203 ± 32	93.2 ± 14.7
Amb. CG400 / 1 h	20 % HCl / 80 % MeOH	1.4 ± 0.6	163 ± 26	118 ± 19
Amb. CG400 / 1 h	1 % AcH / 99 % MeOH	-0.19 ± 0.97	93.0 ± 8.6	930 ± 86
Amb. CG400 / 1 h	5 % AcH / 95 % MeOH	-0.41 ± 0.97	106 ± 10	1064 ± 98
Amb. CG400 / 1 h	20 % AcH / 80 % MeOH	-0.29 ± 1.09	211 ± 27	2111 ± 273
Amb. CG400 / 1 h	30 % AcH / 70 % MeOH	-0.65 ± 0.99	292 ± 31	2924 ± 305
Amb. CG400 / 1 h	**50 % AcH / 50 % MeOH**	**-0.43 ± 0.59**	**563 ± 87**	**5632 ± 872**
Amb. CG400 / 1 h	70 % AcH / 30 % MeOH	4.3 ± 0.8	1123 ± 173	261 ± 40
Amb. CG400 / 1 h	90 % AcH / 10 % MeOH	14.5 ± 2.2	836 ± 86	57.5 ± 5.9

In case of K_D-values showing a negative value, what can emerge due to the uncertainties in radioactivity and volume, the separation factors were calculated with a K_D-value of 0.1, taking conservatively a minimal physical absorption into account. The corresponding K_D values and separation factors for varying HDEHP concentrations from Table 20 are graphically depicted in Figures 40 and 41.

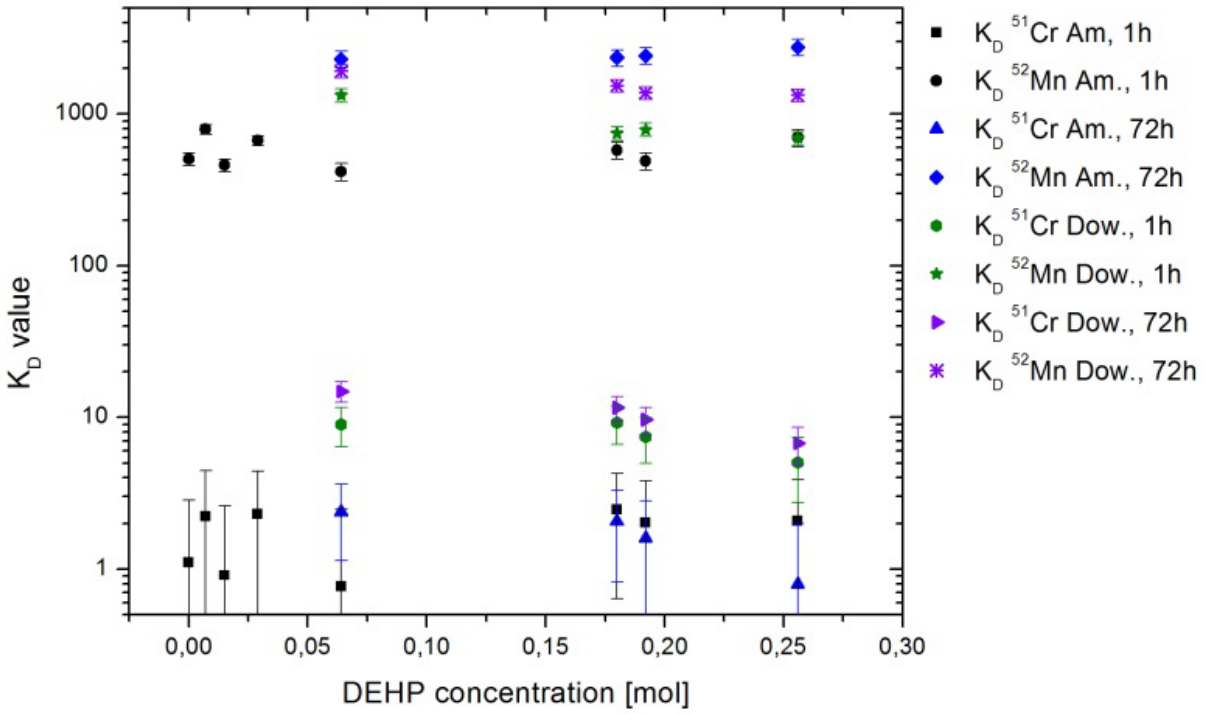

Figure 40: Comparison of K_D values with varying DEHP extractant concentrations on DOWEX 50WX8 and Amberlite CG400 after 1h and 72h equilibration time.

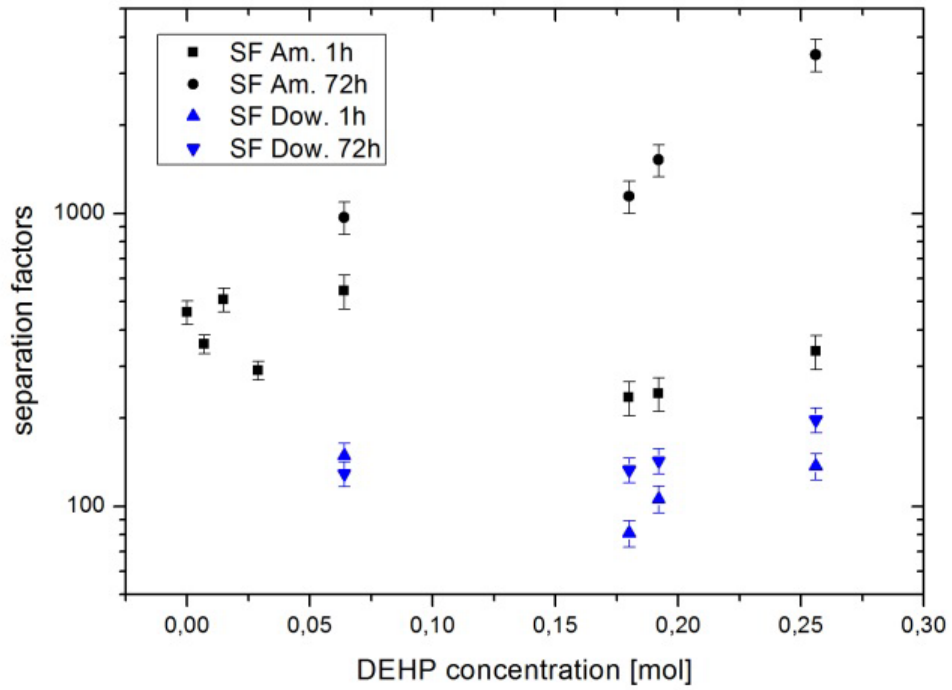

Figure 41: Separation factors of Cr and ^{52g}Mn with varying DEHP concentrations on DOWEX 50WX8 and Amberlite CG400 after 1h and 72h equilibration time.

No conclusive trend leading to an optimal HDEHP concentration was observed with the distribution coefficients. The highest separation factor after a 1h equilibration time was found to be 543 ± 71 for a 0.064 M (2.2 wt%) HDEHP solution on the anion exchange resin Amberlite CG400. Therefore, a proof of principle column separation was conducted using an ethanolic 0.064 M (2.2 wt%) HDEHP solution with the corresponding elution profile as depicted in Figure 42.

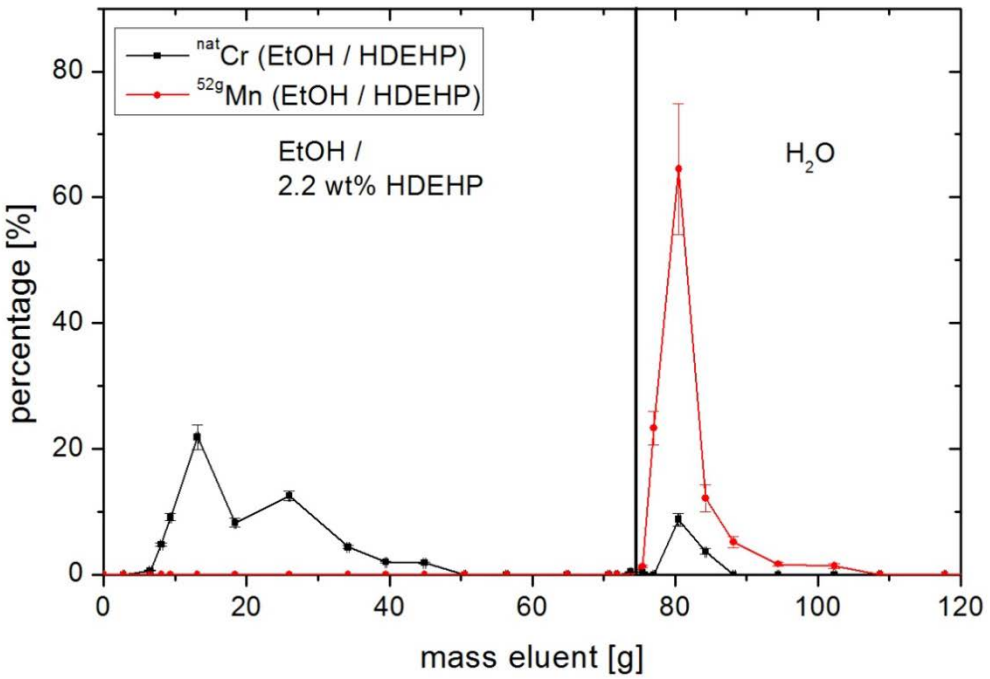

Figure 42: Elution profile of a *Mn separation from Cr on an anion exchange resin (resin: Amberlite CG400, Cr eluent: EtOH with 2.2 wt% HDEHP extractant, Mn eluent: H_2O.

Again, the elution profile shows a broad Cr elution peak as well as chromium impurities in the manganese fractions of approx. 13 % in total. This is not tolerable for a subsequent n.c.a. labelling application. But no manganese breakthrough was detected in the chromium fractions. For quantitative elution of radiomanganese pure water was sufficient which simplifies processing for the subsequently planed radiolabelling.

Due to the inconclusive influence of the HDEHP concentration on distribution coefficients another K_D-value screening was done, testing MeOH, EtOH, 2-PrOH and BuOH as solvents without the addition of any extractant (see Figure 43). Those alcohols were furthermore selected for their varying alkyl chain length, to investigating their possible different complexing behaviour with Cr or Mn.

The distribution coefficients as well as SF are showing that no extractant is needed for the successful absorption of $^{52}Mn^{2+}$ on the anion exchange resin Amberlite CG400 (see Figure 43). Additionally, the binding affinity of Cr^{3+} towards the resin decreases with shorter alkyl

chains, making MeOH the most promising solvent. The elution profile of the *Mn separation from Cr using MeOH as loading and elution solvent for Cr is depicted in Figure 44.

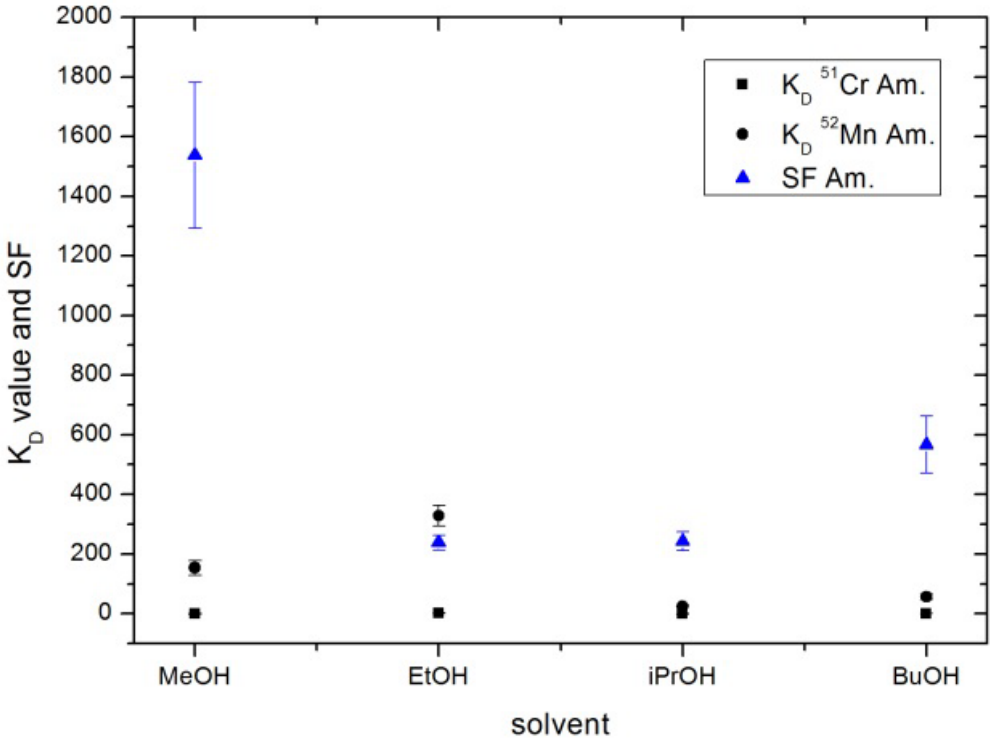

Figure 43: K_D values and separation factors of ^{51}Cr and ^{52}Mn with MeOH, EtOH, 2-PrOH and BuOH on Amberlite CG400.

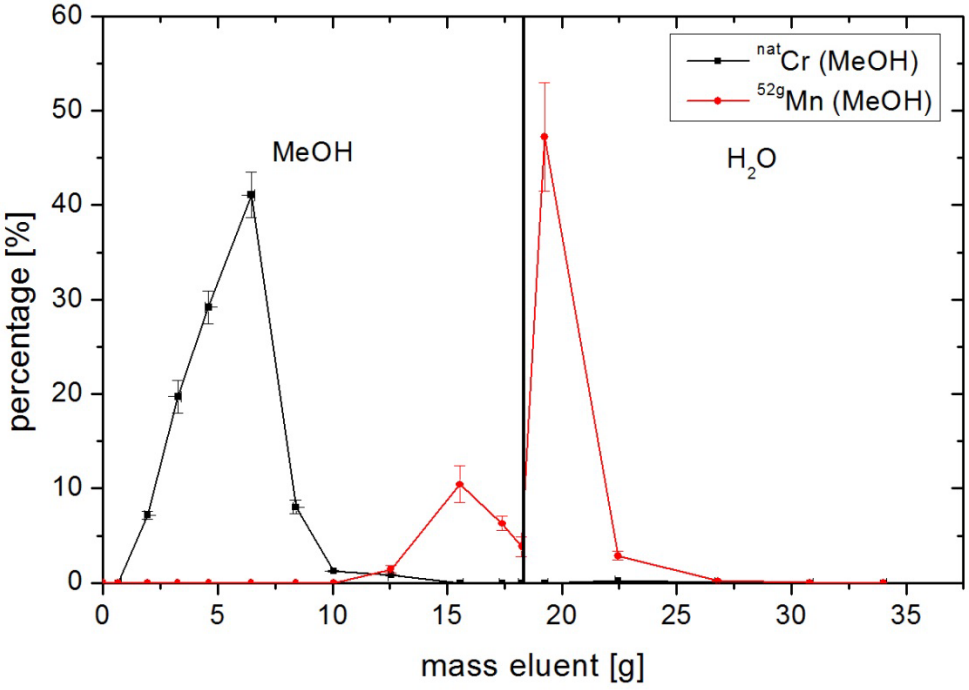

Figure 44: Elution profile of a *Mn separation from Cr with MeOH as eluent (resin Amberlite CG400, Cr eluent: MeOH, Mn eluent: H_2O).

The elution peak of Cr is considerably smaller than for the separation with ethanol, however, as soon as the concentration of Cr in the eluent drops below 1.2 mg/mL, about 18 % of the absorbed Mn activity is slowly eluted before the change to pure H_2O as eluent. As a result only about 1 % of Cr impurity is found within the radiomanganese fractions.

Still, another investigation of K_D-values was done to evaluate the utilisation of an additive to either suppress the manganese leaching or to accelerate the elution of weakly adsorbed Cr. Especially to achieve the latter, acetic acid and hydrochloric acid were tested as additives and the K_D-values and SF were determined and are shown in Figures 45 and 46.

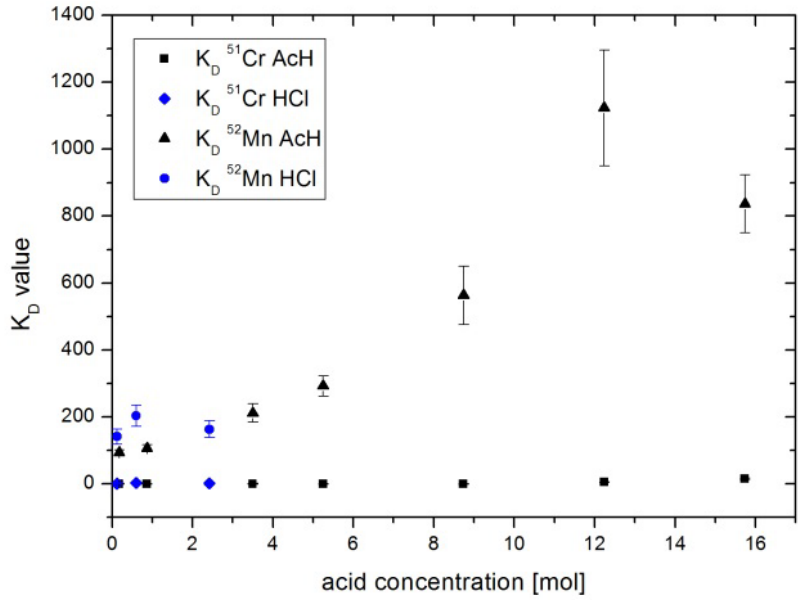

Figure 45: K_D values of the Amberlite:MeOH system with addition of acetic and hydrochloric acid for the suppression of chromium retention.

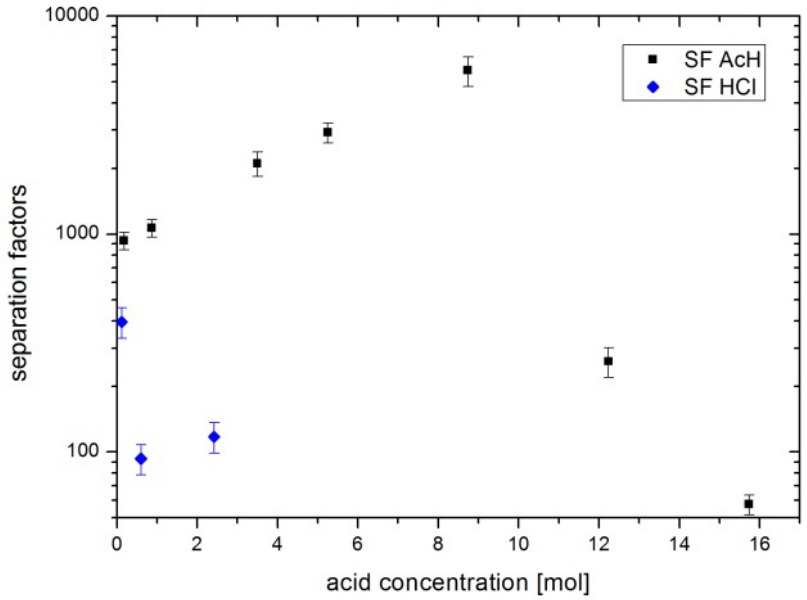

Figure 46: Separation factors of the Amberlite:MeOH system with addition of acetic and hydrochloric acid for the suppression of chromium retention.

The addition of acetic acid shows the greatest effect on the ion exchange behaviour of Cr and Mn. The Mn absorption rises steadily until an acetic acid concentration of 12.24 M is reached. However, at the same concentration a simultaneous absorption of chromium can be observed. Therefore, the optimal acetic acid concentration for a high radiomanganese absorption and low Cr retention is at 8.74 M. The elution profile of a separation executed with 8.74 M acetic acid in MeOH for the elution of Cr is depicted in Figure 47.

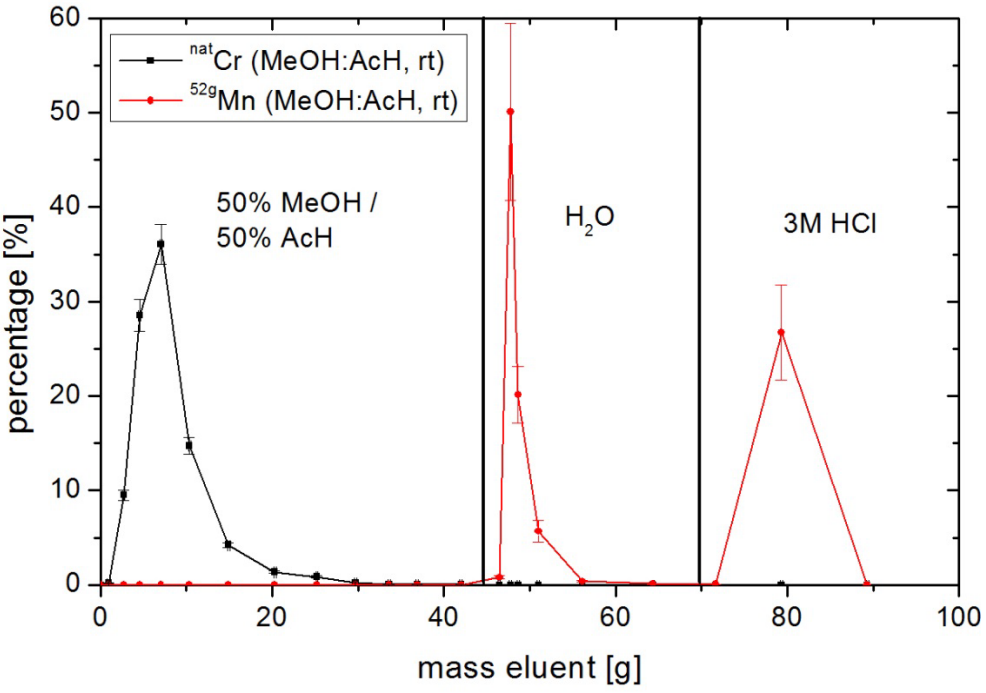

Figure 47: Elution profile of the *Mn separation from Cr with the Amberlite: MeOH:AcH system (resin: Amberlite CG400, Cr eluent: 1:1 MeOH:AcH, Mn eluent: H_2O 1. Mn peak, 3 M HCl 2. Mn peak).

The elution peaks of Cr and Mn are well separated and no radiomanganese breakthrough is detected in the acetic acid eluent. But now, the bound Mn species shows such a high affinity towards the resin that pure water is not enough for a quantitative elution of radiomanganese. Only 77.2 % radiomanganese were eluted with pure water. However, the residual ^{52}Mn can be quantitatively eluted with 3 M HCl; shown in Figure 47 as a second ^{52}Mn elution peak. Therefore, the ^{52}Mn eluent was changed to 3 M HCl in the subsequent separations.

A further optimization was done by increasing the column temperature. The higher temperature accelerates the ion exchange rate between the mobile and stationary phase which influences the eluent volume size necessary for quantitative elution of Cr and Mn. The temperature was increased after the main mass of Cr was passed through the column to minimise a negative effect on the mass of absorbed Cr. The elution profile of a separation of ^{52}Mn conducted at 50°C and 3 M HCl is depicted in Figure 48.

The separation was completed within 3 to 4 h after the disassembly of the target. The elution fraction volume of Cr was reduced by the factor of two while 99.5 % of ^{52}Mn was eluted with 2.1 mL of eluent. No radioactive ^{51}Cr was anymore measured in the ^{52}Mn fractions over a counting period of three days. Should trace amounts of chromium still be present in the resulting ^{52}Mn fraction, the procedure could be repeated within a short period of time because the small elution volume of ^{52}Mn could be evaporated quickly. This volume can be optimised further by use of columns with smaller diameters. However, for the purpose of the present work the elution volume was suitable.

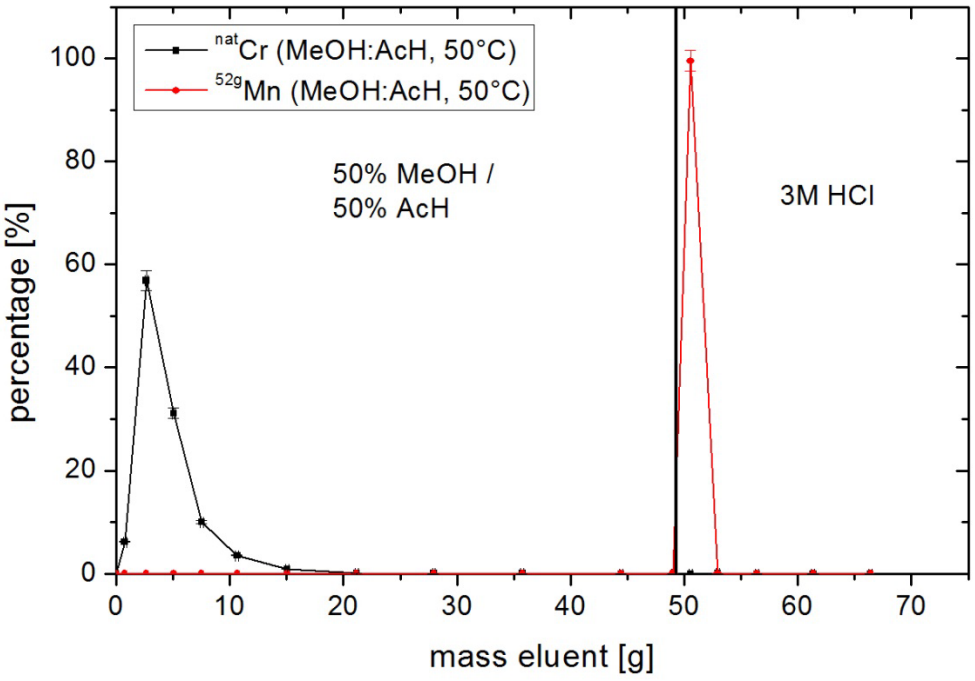

Figure 48: Elution profile of the optimised *Mn separation from Cr (resin: Amberlite CG400, Cr eluent: 1:1 MeOH:AcH, Mn eluent: 3 M HCl).

In conclusion, the optimised procedure seems to be feasible for the separation of ^{52}Mn in a much smaller eluent volume than in the previously developed separation methods. The final procedure can be summarised as follows:

Optimised radiochemical separation procedure for n.c.a. ^{52}Mn

- dissolution of 470-500 mg elemental Cr in 5 mL conc. HCl at 70°C,
- evaporation to dryness and re-solvation in 5 mL of 50 % acetic acid and 50 % MeOH,
- loading of the solution onto a previously conditioned Amberlite CG400 column with a diameter of 1 cm and a height of 2 cm,

- elution of bulk Cr and residual impurities at an elevated temperature of 50°C with 45 mL of 50 % acetic acid and 50 % MeOH,
- elution of n.c.a. radiomanganese in 2-3 mL of a 3 M HCl solution at 50°C.

The final solution can be evaporated to dryness and the residue completely re-dissolved in pure water for further processing. The resulting solution was found to be slightly acidic due to residual hydrochloric acid. The produced n.c.a. ^{52}Mn was used in this form for the radioactive synthesis of the MnO nanoparticle precursor $Mn(acac)_2$ as described below.

4.5 Authentic manganese nanoparticle labelling

In recent years a strong focus in MR contrast agent research was on the development of new nanosized contrast agents. Two main advantages of nanosized contrast agents are postulated in literature.[152] The first is the increased volume concentration of the contrast enhancing element in nanoparticles leading to an even higher contrast enhancement in comparison to single chelates. The second is a possible functionalization of the nanoparticle shell with tumour or disease targeting moieties or groups prolonging blood circulation time of the particles.[153]

Considering this beneficial translation of MR contrast agents into nanosized compounds, divalent manganese is the most promising element besides trivalent gadolinium. Its five unpaired electrons lead to a high T_1 relaxivity change in MRI. Several water-soluble manganese based nanoparticle concepts exist, but none was completely evaluated for a use *in vivo*. Even though the potential of nanosized diagnostic or therapeutic agents is high, a critical assessment of the advantages of nanosized compounds over already existing drugs is essential. The authentic labelling of manganese based nanoparticles might be an excellent *in vivo* analytical means to facilitate another step towards the realisation of nanosized contrast agents with a useful application, because of the low detection limits and precise bio-distribution studies possible with the PET systems.

4.5.1 MnO nanoparticle synthesis

Radioactive precursor synthesis for authentic labelling of MnO-nanoparticles

As described in the introduction (chapter 1.9.1), most synthesis routes of nanoparticles are in need of a suitable precursor. Therefore, efficient authentic labelling of a nanosized compound can only be realised with an authentic labelled precursor as starting material. The isotopic labelling of an already known MnO nanoparticle precursor was performed here as proof of principle. When the separation was done as described by Graddon et al. [131], a dark

brown precipitate was formed as by-product which is most likely MnO_2. This was prevented by performing the separation process in the dark and in an inert atmosphere.

The adapted precursor synthesis (see section 3.6.1) resulted in a radioactively determined yield of 73.9 ± 5 % and a weighing yield of 78.7 ± 5 %; results coinciding within one standard deviation. These deviations mainly originate from the slightly altered detection geometry in the radioactivity measurements compared to the radioactive reference point sources used for the efficiency calibration of the γ-ray detectors. For comparison: Graddon et al.[131] described a yield of 87 % for the crude and not re-crystallised product. The yield found in this work can be optimised by reduction of physical product loss in the washing procedure. Even though the separation from the washing solution was done with utmost care, a portion of yellow precipitate was lost. Reprocessing of the washing solution may reduce this loss of yield. However, it was still high enough for the subsequent synthesis and therefore no further optimisation was undertaken.

The ESI-MS spectra of the synthesised compound and of the purchased reference material are depicted in Figures 49 and 50.

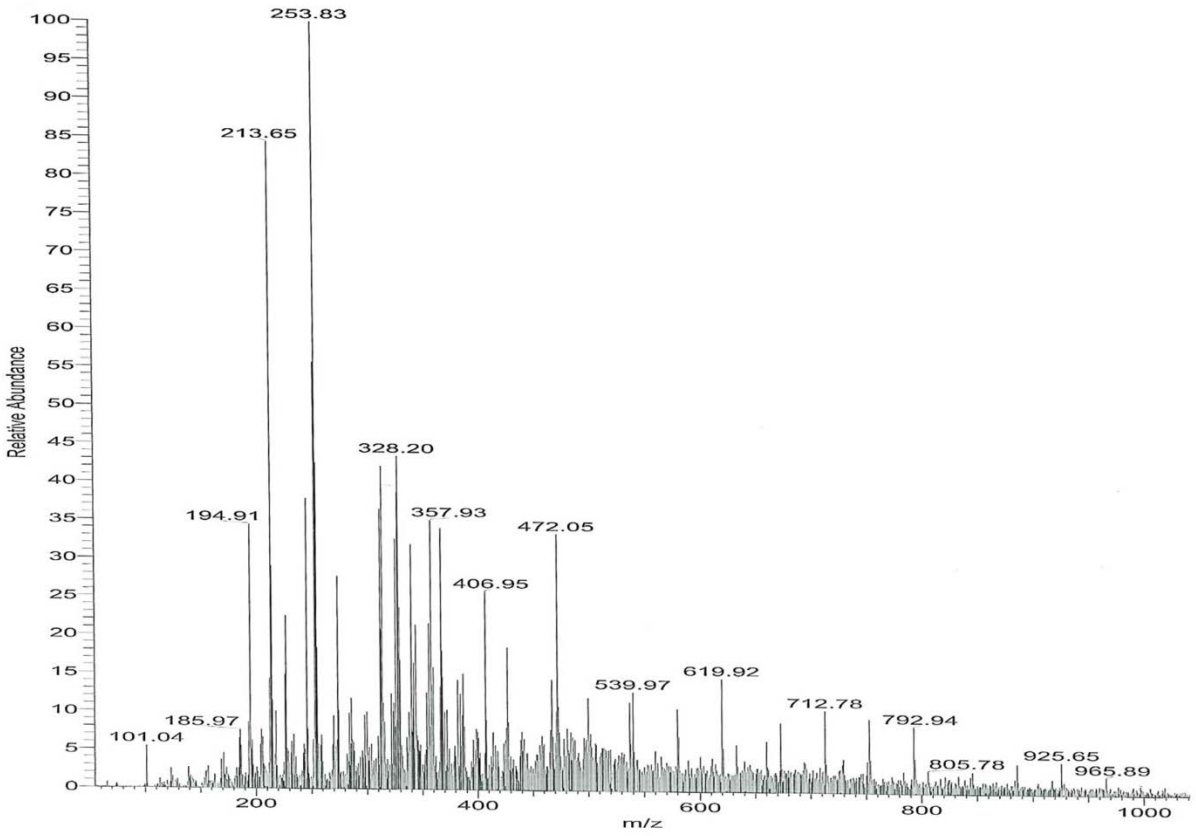

Figure 49: ESI-MS spectrum of synthesised $Mn(acac)_2$ (M = 253.15 g/mol) without further purification.

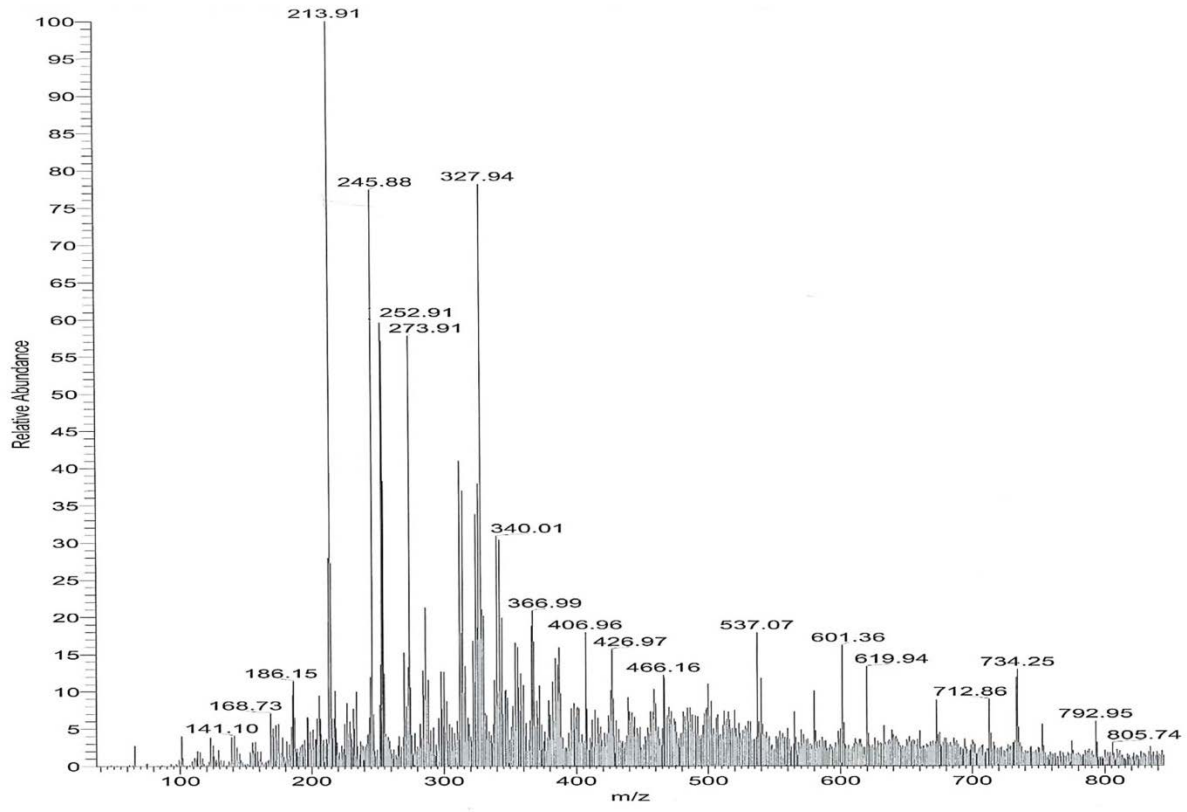

Figure 50: ESI-MS spectrum of $Mn(acac)_2$ (M = 253.15g/mol) reference standard.

The prominent mass peak at 253.83 m/z in Figure 49 is identified as $Mn(acac)_2$ (M = 253.15 g/mol). This peak is also found in the reference spectrum, thus confirming the success of the synthesis. Other depicted peaks are fragments in the unlikely case and in the most likely case adducts of $Mn(acac)_2$ with ions or neutral additives of the analysis solution, like Na^+, CO_3^{2+}, H_2O, MeOH or AcOH. Furthermore, the formation of clusters is possible due to the very low ionisation voltage used. The relative abundances of peaks in these measurements are also not specific for $Mn(acac)_2$, due to the soft ionisation method used.

Inactive microwave assisted MnO-nanoparticle synthesis

For the authentic labelling of nanoparticles a short reaction time is very important if radionuclides with shorter half-lives should be applied. In many organic syntheses the application of microwave heating leads to increased yields in a shorter reaction time and often a higher purity of the desired product. Recent reviews showed the potential of microwave heating in nanoparticle synthesis.[154, 155] Therefore, the translation of several different literature synthesis routes for water-dispersible, nanosized MnO particles to microwave supported synthesis was tested. The tests were performed with inactive precursor material only because the subsequently necessary analytical characterisation methods of the products were not available in a controlled area. None of the tested syntheses yielded water-

dispersible MnO-nanoparticle in a reproducible manner. As the formation of nanoparticles is a very complex process, this lack of repeatability in the results could be caused by, but not exclusively, precursor structure, heating time, nucleation temperature, growth temperature, coating agent, washing solution, centrifugation speed and more.

All assessed synthesis routes were based on the controlled decomposition of a manganese precursor (Mn(II)acetate; Mn(II)acetylacetonate) in a non-aqueous medium (triethylene glycol, trioctylamine, benzyl alcohol) and a combined or subsequent coating step with an amphiphilic coating agent, for example polyvinylpyrrolidone (PVP, avg. mol. weight: 40,000) or polyethylene glycol (PEG, avg. mol. weight: 200 – 6,000). As described by Bilecka et al.[132], the decomposition of the manganese precursor occurred under inert conditions excluding oxygen with utmost care, as its presence led to the direct aggregation of the nanoparticles with or without coating agent.

The following coating step was necessary to achieve water solubility and dispersion stability. Every nanoparticle solution without an extra coating agent aggregated or oxidised in a period of minutes to hours after the synthesis. Even with a suitable polymer coating, the nanoparticles synthesised in this work did not form aqueous dispersion that were stable over a longer time period.

The reaction parameter of the most successful nanoparticle preparation with synthesised $Mn(acac)_2$ as precursor and PVP 40,000 as coating agent is described in chapter 3.6.1. The DLS measurement of the unprocessed nanoparticle dispersion directly after the synthesis showed a mean radius of approx. 31 nm in triethylene glycol. After the separation of residual precursor and coating agent and re-dispergation in 2-propanol the DLS measurement showed an increased mean radius of 65 nm. The comparison of the size distribution curves is presented in Figure 51.

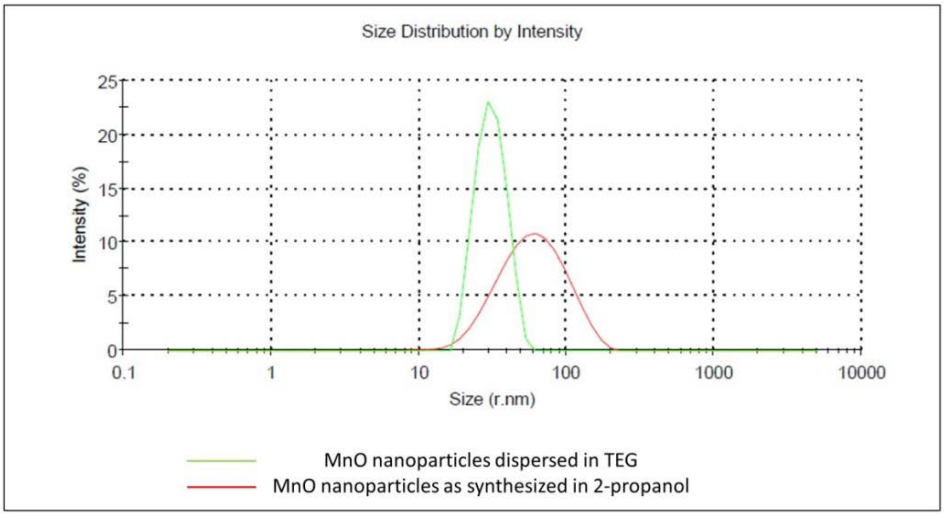

Figure 51: DLS measurement of self-synthesised MnO nanoparticles in the initial solvent triethylene glycol and isolated in 2-propanol.

In addition to the higher radius, a broadening of the size distribution can be observed which could be the beginning aggregation of the particles. TEM measurements were conducted with the re-dispersed nanoparticles in search of an explanation for the broadened size distribution. The images of the TEM and the SAED measurements are depicted in Figure 52.

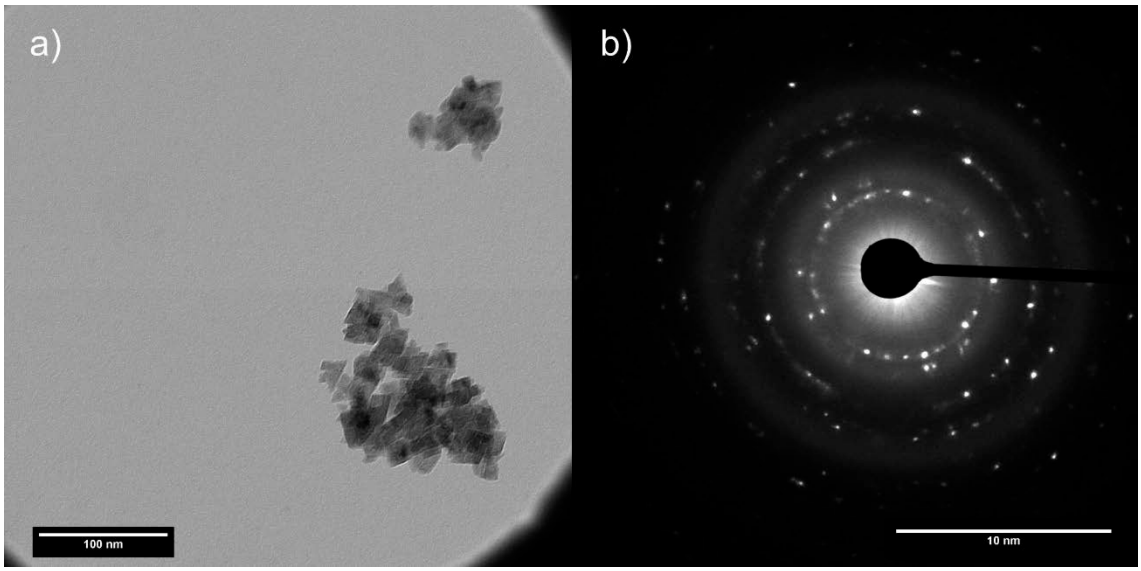

Figure 52: TEM images of a) synthesised MnO nanoparticles in 2-propanol and b) an electron diffraction pattern thereof.

The TEM images clearly show nanocrystals aggregated into larger clusters. The nanocrystals and aggregates possess an average geometric diameter of approx. 22.2 ± 5.5 nm and 70.1 ± 25.4 nm, respectively. This agrees well with the increasing radius of nanoparticles seen in the DLS measurements in triethylene glycol and 2-propanol. Some of the smaller particles are still left in the dispersion while the majority has aggregated to larger clusters. This means that the polymer coating with PVP is at least imperfect and cannot prevent the formation of larger aggregates. Still, the presented method shows another possibility to synthesise a crystalline product with particle sizes below 100 nm by microwave heating in a short time. Similar cubic and triangular shaped nanocrystals with a slightly larger edge length of 30 – 50 nm were found in another microwave assisted synthesis reported by Bilecka et al.[132]. The observed reduction of size in this work can be caused by the separation of the nucleation and growth period by explicit temperature control adapted from literature[156]. The uniform heating and cooling of the sample in the microwave oven is a clear advantage for such a controlled synthesis.

An authentic core labelling is only reasonable with water-dispersible particles which are stable for several days. Otherwise, *in vivo* stability tests cannot be conducted, and the particles are just not suitable for PET/MR measurements. Therefore, further optimization work has to be invested regarding the polymer coating leading to the production of a water-

dispersible manganese nanosized compound. In context with the recent concern regarding the usefulness of nanosized diagnostics and therapeutics[157] the question has to be asked if further efforts are indeed worthwhile.

4.5.2 Irradiation of water-dispersible Mn_3O_4-nanoparticles

An alternative to the challenging complete synthesis of an authentically core labelled nanoparticle is the direct irradiation of commercially available nanosized compounds with charged particles or neutrons. Therefore, water-dispersible Mn_3O_4 nanoparticles were activated here with isotopic and non-isotopic radionuclides to investigate their integrity and dispersion stability after an irradiation as described in chapter 3.6.2. Additionally, the release of manganese ions from neutron irradiated nanoparticles was examined. The size distribution results of all conducted activation studies are summarised in Table 21.

Table 21: TEM- and DLS-determined sizes of Mn_3O_4 nanoparticles after the activation studies.

Material	Diameter TEM [nm]	Diameter DLS [nm]
Mn_3O_4 (purchased)	15.6 ± 5.1	68.6 ± 1
Mn_3O_4 (proton activated)	-	100 ± 8
Mn_3O_4 (neutron activated)	11.7 ± 4.2	74 ± 2
Mn_3O_4 (neutron activated, leeched in H_2O)	13.8 ± 3.7	87 ± 1
Mn_3O_4 (neutron activated, leeched in PBS solution)	-	227 ± 4

Irradiation of Mn_3O_4-nanoparticles with charged particles

The nuclear reaction $^{16}O(p,\alpha)^{13}N$ is of interest regarding the activation of nanoparticles because of the high abundance of oxygen in many nanosized materials and the favourable decay characteristics of ^{13}N for PET (half-life: 10 min, avg. β^+-energy: 491.82 keV, β^+-emission: 99.8%). In an initial test, Mn_3O_4 nanoparticles were irradiated with 8.5 MeV protons to allow a subsequent characterisation and to assess the change induced by the charged particle irradiation. The proton energy was kept below the threshold of other nuclear reactions (<10.4 MeV) which would lead to longer-living radionuclides, e. g. the $^{55}Mn(p,pn)^{54}Mn$ process. TEM images prepared from the irradiated and partial dispersed nanoparticles are depicted in Figure 53.

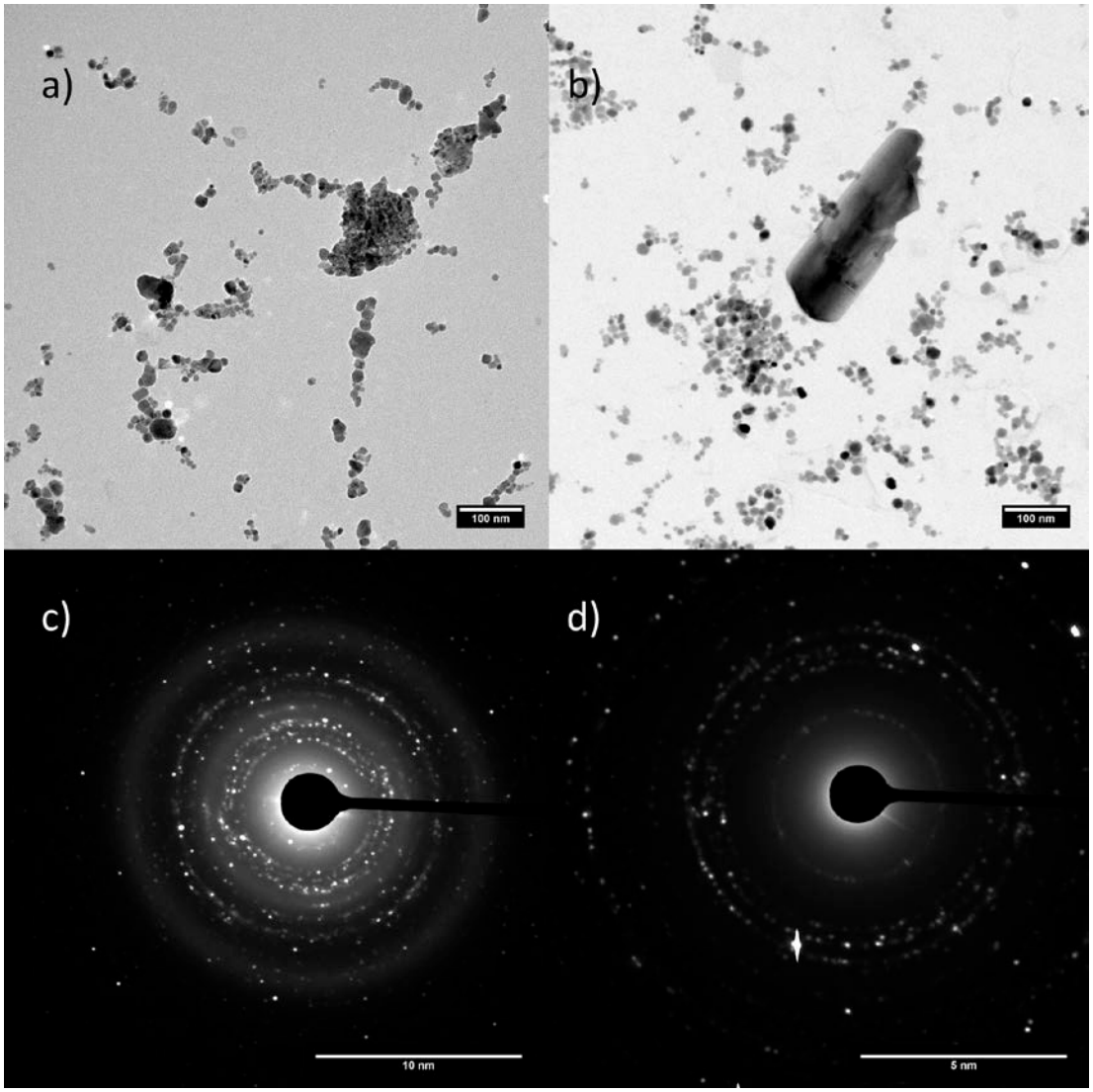

Figure 53: TEM images of a) purchased Mn_3O_4 nanoparticles, b) proton irradiated Mn_3O_4 nanoparticles, c) electron diffraction pattern of inactive Mn_3O_4 nanoparticles, and of d) proton activated Mn_3O_4 nanoparticles.

Directly after the irradiation and the disassembly of the sediment target a different physical behaviour was observed. Unlike before, only a fraction of the nanoparticles were dispersible in pure H_2O by treatment with an ultrasonic bath. An influence of the target preparation on the dispersion behaviour was excluded by testing non-irradiated sediments beforehand which exhibited normal water-dispersibility.

The radioactive decay of the resulting supernatant was analysed after the partial dispersion of the targets. The graphical extrapolation of the decay curve showed a half-life of 10.03 ± 0.32 min which agrees well with the half-life of ^{13}N. No radioactive impurities with longer half-lives were detected in long time γ-spectrometric measurements. The activation of Mn_3O_4 nanoparticles with ^{13}N was thus successful. The DLS measurements, however, showed a diameter of 100 ± 8 nm which is 31 % larger than the original particles' size

distribution. A considerable alteration of the nano-material can be observed in the TEM images showing larger crystals beside the original Mn_3O_4 nanoparticles due to the proton bombardment (see Figure 53 b).

These larger crystals must have formed during the irradiation. The heat of a focused particle beam cannot be distributed fast enough throughout the complete sample leading to a partial melting and re-crystallisation within the sediment. Another side effect may also be the partial destruction of the polymer coating and, hence, a loss of water-dispersibility of the particles.

The use of higher particle energies might principally be interesting considering the $^{55}Mn(p,p3n)^{52g}Mn$ reaction with a threshold of 31.7 MeV. But, no further activation studies were conducted due to the disintegration of the nanoparticles in the lower energy range. A possible solution to minimise the induced damage is the direct irradiation already in solution or the “softer” activation with neutrons.

Irradiation of Mn_3O_4-nanoparticles with neutrons

For the activation of Mn_3O_4-nanoparticles the neutron induced $^{55}Mn(n,\gamma)^{56}Mn$ reaction was used, due to its relatively high cross section of approx. 13.2 b for thermal neutrons[142, 158] and a high intensity γ-ray favourable for γ-spectrometry (see Table 1). The irradiation was explicitly done with thermal neutrons which do not deposit a significant energy within the target material. Thus, no change of the nano-structures is to be expected on the large scale except for the damage of the crystal structure due to the direct impact of neutrons and the subsequent emission of β-particles caused by the radioactive decay of the activated target.

As expected, no macroscopic difference between untreated and activated Mn_3O_4 particles was observed before and after irradiation with neutrons. No aggregation was visible in a time interval of several weeks after irradiation in the clear darkish brown solution. This was confirmed by TEM measurements of the particles after the complete decay of ^{56}Mn. No relevant changes were observed in the relatively broad spread size distribution of the primal particles depicted Figure 54 a) and their neutron irradiated counterparts in Figure 54 b).

The analysis of 194 not activated nanoparticles yielded a poly-disperse size distribution of crystalline nanoparticles ranging from 4.8 nm up to 46.3 nm. The diameters of the 57 analysed activated nanoparticles ranged from 3.6 nm to 25.8 nm. These minor size differences between both probes can be accounted to the poly-disperse nature of the samples, the limited amount of analysed particles, and their non-spherical shape, which broadened the size distribution even further. Therefore, the TEM analyses provided the first evidence for a successful authentic radiolabelling of manganese oxide nanoparticles without significant change in size or shape.

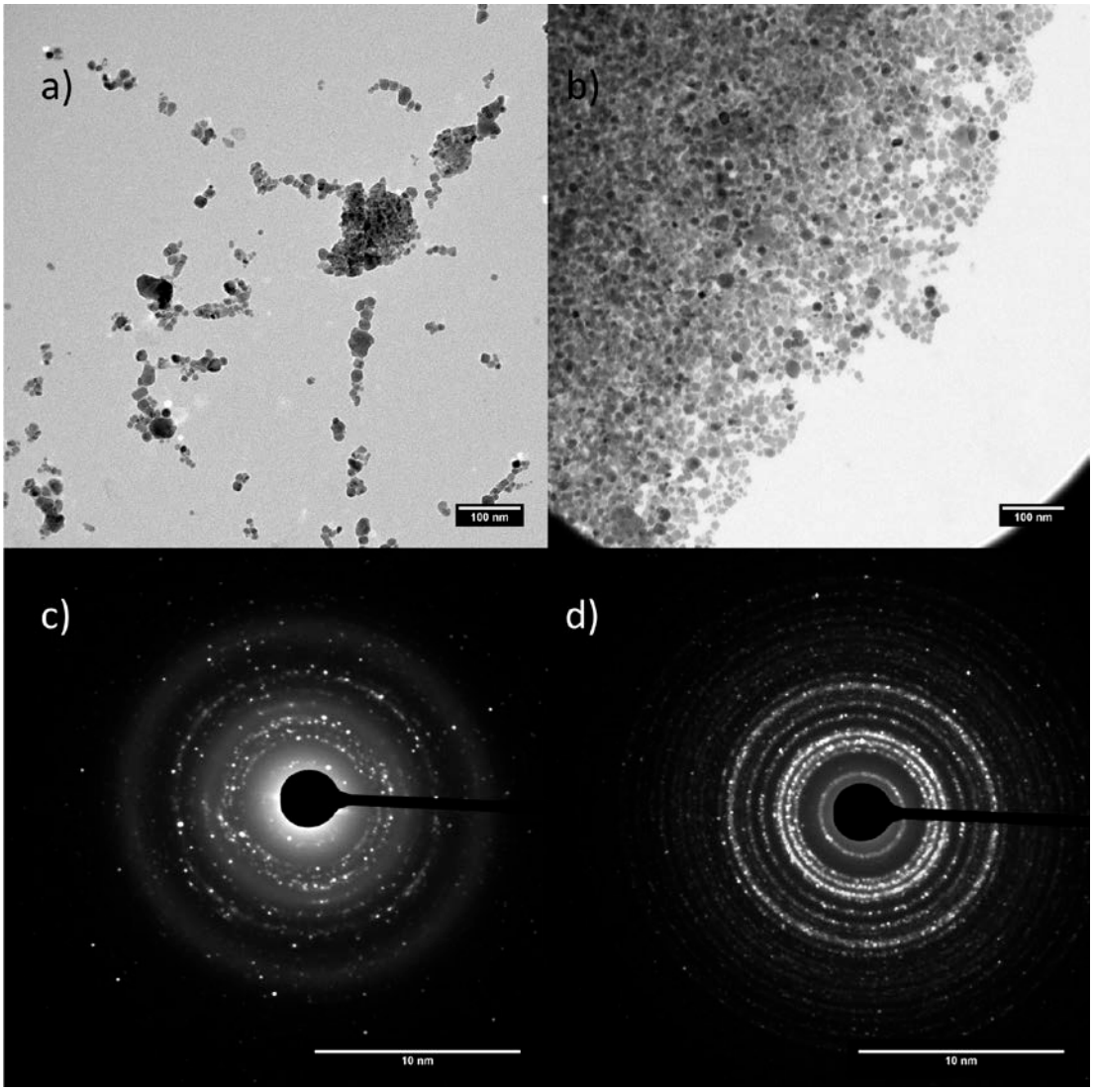

Figure 54: TEM images of a) purchased Mn_3O_4 nanoparticles, b) neutron irradiated Mn_3O_4 nanoparticles, c) electron diffraction pattern of inactive Mn_3O_4 nanoparticles, and d) of neutron activated Mn_3O_4 nanoparticles.

Further evidence of a successful radiolabelling without destruction of the target matrix can be obtained from the electron diffraction pattern comparison of the primary and the irradiated nanoparticles. While the direct determination of the crystal lattice is very elaborate with SAED, diameters of the occurring diffraction circles are conclusive in case of a direct probe comparison. The first and second diffraction circles of the primal and activated nanoparticles were $4.05 \pm 0.05\ nm^{-1}$ and $6.41 \pm 0.07\ nm^{-1}$ in diameter and $4.05 \pm 0.01\ nm^{-1}$ and $6.38 \pm 0.02\ nm^{-1}$, respectivly. They are congruent within their uncertainty limits with a deviation below 1 %. Therefore, it can be concluded that no macroscopic crystallographic change occurred during the irradiation and decay. For further stability assessment of the introduced label ^{56}Mn, leaching experiments were conducted subsequently.

Stability and leaching experiments with activated Mn_3O_4-nanoparticles

Complementary to the nanoparticle size and crystal structure characterisation the performed irradiation allowed the investigation of their dispersion stability and the examination of a possible Mn ion release. While decomposition over time is highly desirable for *in vivo* contrast agents based on iron oxide for their excretion, manganese ions are toxic and thus the release has to be kept at trace levels.

In the characterisation of neutron irradiated nanoparticles (see chapter 3.6.3) leached with pure water, no aggregation was visible in the clear darkish brown solution over a time interval of several weeks after irradiation. Incubation in phosphate buffered saline (PBS) led to an aggregation of the particles in course of the experiments and no TEM analysis was anymore possible afterwards.

However, the leaching experiments allowed the investigation of the Mn ion release in H_2O and PBS for a time interval of approx. 15 h after the initial irradiation. After these 6 half-lives of ^{56}Mn the radioactivity was too low for further γ-ray measurements. The results of the potential leaching in PBS and HPLC-grade water are depicted in Figure 55 while the respective TEM images are depicted in Figure 56.

A steady increase of manganese concentration was observed with up to (2.1 ± 0.3) µg Mn in solution after 15 h of leaching, which corresponds to a very low fraction of (0.033 ± 0.005) % of the complete manganese inventory of 8.8 ± 0.7 mg Mn_3O_4.

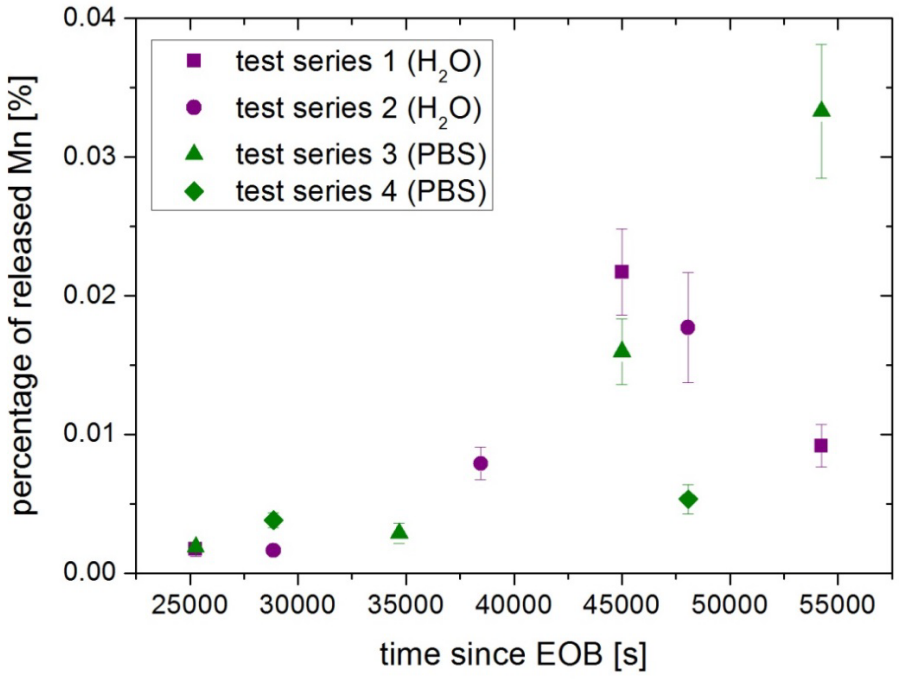

Figure 55: Percentage of released Mn ions from a sample of 8.8 mg Mn_3O_4-nanoparticles within 15 h after irradiation with neutrons.

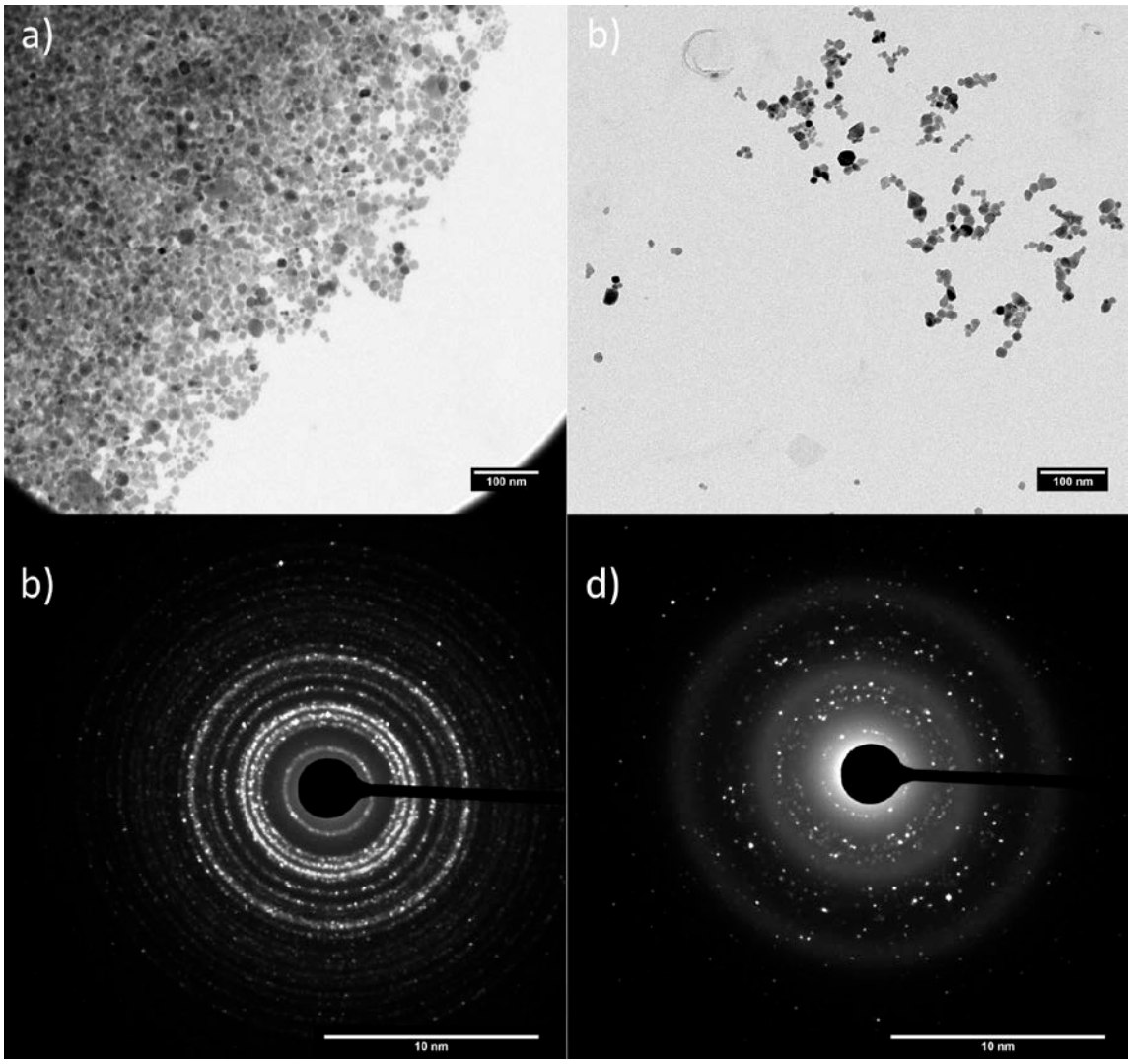

Figure 56: TEM images of a) neutron irradiated Mn_3O_4 nanoparticles before leaching, and b) after leaching, c) electron diffraction pattern of irradiated Mn_3O_4 nanoparticles before leaching, and d) after leaching.

For comparison, the known acute oral toxicity of $MnCl_2 \cdot 4\ H_2O$ in Sprague-Dawley rats is relatively low with a LD_{50} value of 1484 mg/kg.[159] The toxicity by intraperitoneal injections in rats on the other hand is LD_{50} = 138 mg/kg and therefore one order of magnitude higher.[160] While the released amount of free manganese is low in comparison, a meaningful and precise discussion, if this amount is high enough to induce a toxic effect, can only be done with a known biological half-life of the nanoparticles. The authentic activation of Mn_3O_4-nanoparticles by neutrons, as shown here, could deliver the precise answer for the first 15 h after exposure, without the introduction of any additional analysing agents.

5. Summary

In this work, some of the nuclear chemical aspects of the production of suitable radionuclides for authentic labelling of current or experimental MR contrast enhancing agents based on gadolinium (III) and manganese (II) were studied. This includes the identification of suitable radioisotopes of gadolinium and manganese for application in nuclear imaging methods (SPECT/PET), the measurement of nuclear data important for their production, their actual production, radiochemical separation from the target material, and a proof of principle application. In addition, the concept of activation with charged particles and neutrons was assessed with commercial manganese oxide nanoparticles in order to examine their applicability for *in vivo* application in MRI.

The radioisotopes ^{147,149}Gd were chosen for application with SPECT and autoradiographic studies because of their favourable γ-ray energies. The shorter half-life of ^{147}Gd (38.06 h) benefits an application *in vivo* while the longer half-life of ^{149}Gd (9.28 d) is ideal for laboratory studies. The cross sections of the nuclear reactions induced by deuterons and protons on $^{nat}Eu_2O_3$ leading to both radionuclides as well as the relevant by-products were measured up to 70.9 MeV and 44.8 MeV, respectively. A maximum of the ^{147}Gd excitation functions for deuteron induced reactions was found at 56.3 ± 0.5 MeV with 190 ± 19 mb while no clear maximum can be observed in the examined energy region of proton induced reactions. The ^{149}Gd excitation function for deuteron induced reactions showed two maxima at 56.3 ± 0.5 MeV (327 ± 32 mb) and 32.6 ± 0.8 MeV (327 ± 34 mb). The proton excitation function exhibited one clear maximum at 25.3 ± 0.7 MeV (432 ± 26 mb) while the second was only indicated at 44.8 ± 0.4 MeV (332 ± 36 mb), respectively. The excitation functions of the ^{151}Gd impurity showed nearly the same trend in comparison to ^{149}Gd making a radionuclidically pure production with natural europium impossible.

Integral yields were calculated with the measured excitation functions of ^{147}Gd and ^{149}Gd over the complete examined energy range to 177.3 ± 19.7 and 81.6 ± 8.5 MBq/μAh for deuteron induced reactions and to 43.3 ± 4.4 and 61.8 ± 4.9 MBq/μAh for proton induced reactions, respectively. Experimental thick target yields were determined for proton induced reactions on $^{nat}Eu_2O_3$ in the energy region from 45 to 31 MeV and from 36 to 18 MeV. The results in the upper energy region for ^{147}Gd and ^{149}Gd were 27.9 ± 1.5 MBq/μAh and 19.6 ± 1.0 MBq/μAh in the lower energy region. This corresponds to 81.7 % and 82.7 % of the theoretically calculated yields integrated over the same energy region. In the lower energy region ^{149}Gd was produced with a thick target yield of 27.1 ± 1.4 MBq/μAh which corresponds to 81.1 % of its theoretically calculated integral yield.

5. Summary

A small amount of longer lived isotopic impurities of ^{151}Gd and ^{153}Gd was measured as 0.79 ± 0.04 and 0.025 ± 0.003 MBq/μAh in the higher energy region and to be 1.8 ± 0.1 and 0.037 ± 0.003 MBq/μAh in the lower energy region, respectively. This amounted to a maximum of produced isotopic impurities of 7 % in the examined energy regions. Therefore, the cross section determinations as well as the thick target yield measurements indicated the need of enriched Eu target material for the isotopically pure production of either ^{147}Gd or ^{149}Gd due to overlapping excitation functions. However, the use of enriched Eu target material could be still more cost efficient than the previously proposed irradiation of highly enriched ^{144,147}Sm with α- or ^{3}He-particles due to the low availability of accelerators with exotic particles like ^{3}He, the significantly lower natural abundance of Sm (^{144}Sm nat. ab.: 3.07 %; ^{147}Sm nat. ab.: 14.99 %) and the 3 to 6 times higher production of ^{147}Gd in an actual proton irradiation of natural europium.

A coarse separation of Gd from the macroscopic Eu target material was adapted from a previously developed Na-Hg amalgam extraction for the separation of Sm and Gd. The extraction time period, the europium mass and the amalgam mass of the available separation were optimised. The use of inert atmosphere was tested and proved to be beneficial for an optimised Eu extraction. The best extraction parameters for a 500 mg Eu_2O_3 target pellet were found to be 10 mL of 0.4 wt% Na-Hg amalgam and an extraction time of 20 min. The other parameters, namely the starting pH value of 2 and the buffer solution concentration of 0.4 M NaOAc and 1 M NaCl, were kept constant. A 99.92 % reduction of the Eu contamination down to 0.4 mg was achieved without loss of $^{147/149}$Gd. The necessary removal of excess sodium, chloride and acetate was easily achieved by extraction chromatography on DGA normal resin. The final product was a 0.5 mL aqueous solution of Gd ready for further processing.

As proof of principle, the commercially available contrast agent DOTArem™ was radiolabelled with the prepared ^{147,149}Gd, and its stability in water, phosphate buffered saline and human blood serum was assessed. A 5 min synthesis at 90°C was sufficient for complete labelling. In the stability tests, no ion leaching was observed with the n.c.a. or c.a. Gd-DOTA complexes over a time period of 6 d. Furthermore, the physiological distribution after injection of the complex into rats was compared with that of the commercial complex by respective *in* and *ex vivo* measurements of the tumour implanted brain with MRI and autoradiography. A similar distribution of both compounds in the brain of the rat was observed in the experiments. Different accumulations, however, were noticed in the necrotic regions of the tumour with the autoradiograms and the histologic images. Additionally, carrier-added administration of Gd-DOTA led to a nearly uniform distribution of radioactivity within the striatum in the tumour bearing hemisphere of the brain. The uniform distribution

may be explained by diffusion of the compound after sacrificing the animal and a lower detection limit of radioactivity in autoradiography. An extended animal study would be necessary to ascertain these artefacts.

For manganese, the focus was on the β^+-emitting radioisotope ^{52g}Mn. Integral and experimental thick target yields of this PET-suitable radioisotope were determined to be 13.7 ± 1.6 and 13.1 ± 1.6 MBq/μAh, respectively, for the proton irradiation of natural chromium. A new chromatographic separation based on the elution of chromium with an 1:1 acetic acid:methanol mixture from the anion exchange resin Amberlite CG400 was developed. The separation led to the elution of ^{52g}Mn in 2.1 mL of 3M hydrochloric acid. A feasible production route with an inexpensive, sturdy target material and a facile separation is thereby available, providing ^{52g}Mn more easily for experimental and PET studies.

The resulting ^{52g}Mn was also successfully applied for a radioactive synthesis of the MnO nanoparticle precursor $Mn(acac)_2$ with a radiochemical yield of 74 ± 5 % and a chemical yield of 79 ± 5 %. To develop a direct authentic labelling of water-dispersible MnO nanoparticles, literature synthesis routes of MnO nanoparticles were investigated. However, the available synthesis routes were far too time consuming, ranging from several hours to days, considering radiolabelling of MnO nanoparticles with the more PET-suitable, but shorter lived, ^{51}Mn isotope. Thus, the use of a microwave supported system seemed promising. However, no successful synthesis for water-dispersible MnO nanoparticles with a microwave supported system was found. Results obtained were not reproducible, and the resulting dispersions were unstable.

An activation of commercial, water-dispersible Mn_3O_4 nanoparticles with protons led to the production of ^{13}N, the formation of larger structures (some of them crystalline), and the partial loss of water-dispersibility. On the other hand, neutron activation left the particles unaffected, and the successful determination of trace amounts of free Mn, using ^{56}Mn, was shown in leaching studies. A maximal release of 2.1 ± 0.3 μg (0.033 ± 0.005 %) Mn after an incubation time period of 15 h in PBS was observed in a sample with 8.8 ± 0.7 mg of dispersed Mn_3O_4. In comparison to the toxicity of $MnCl_2 \cdot H_2O$ by intraperitoneal injections in rats of LD_{50} = 138 mg/kg, the release of Mn from this nanoparticle dispersion is rather low which proves its leaching stability in solution. This shows the suitability of the neutron activation of water-dispersible nanoparticles for first stability tests over a time period of at least 15 h. This is a first indication that the leaching stability of Mn from Mn_3O_4-nanoparticles could by high enough to avoid the toxic effects of Mn when used as contrast agent.

In conclusion, the presented investigations led to a facile and more efficient production of ^{147,149}Gd and also of ^{52g}Mn due to the enhancement of existing nuclear data and the development of optimised separation procedures. The radioisotopes are now available in a

suitable chemical form for their subsequent use in isotopic labelling of MR contrast agents. The proof of principle application of a bimodal probe for *in vivo* distribution studies in rats showed the high potential of this isotopic labelling. Additionally, the radiochemical studies of manganese oxide nanoparticles provided a method to assess the ion leaching of nanoparticles with a low detection limit which is of high importance for future applications *in vivo*.

References

1. Kratz, J.-V., Lieser, K. H., *Nuclear and Radiochemistry: Fundamentals and Applications, Vol. 1,* Wiley-VCH, Weinheim, Germany (2013).
2. Kratz, J.-V., Lieser, K. H., *Nuclear and Radiochemistry: Fundamentals and Applications, Vol. 2,* Wiley-VCH, Weinheim, Germany (2013).
3. Hevesy, G., *The Absorption and Translocation of Lead by Plants: A Contribution to the Application of Method of Radioactive Indicators in the Investigation of the Change of Substance in Plants*, The Biochemical Journal, **17**, 4-5, 439-445 (1923).
4. US patent: 1948384, Lawrence, E. O., Method and apparatus for the acceleration of ions, issued: (02/20/1934).
5. Brown, M. A., Semelka, R. C., *MRI: Basic Principles and Applications,* 2nd, Wiley-Liss, Inc., New York, USA (1999).
6. Brownell, G. L., Budinger, T. F., Lauterbur, P. C., McGeer, P. L., *Positron tomography and nuclear magnetic-resonance imaging*, Science, **215**, 4533, 619-626 (1982).
7. Gronenborn, A. M., Roth, K., *NMR-spectroscopy in vivo*, Chemie in Unserer Zeit, **16**, 1, 1-31 (1982).
8. Lufkin, R., Davis, W. L., Osborn, A. G., *Overview of MR-Imaging modalities*, Journal of Computer Assisted Tomography, **17**, 24-29 (1993).
9. Robb, R. A., *Three-Dimensional Biomedical Imaging,* VCH, New York, USA (1995).
10. Dössel, O., *Bildgebende Verfahren in der Medizin: von der Technik zur medizinischen Anwendung,* Springer, Berlin, Germany (2000).
11. Lauterbur, P. C., *Image formation by induced local interactions - examples employing nuclear magnetic-resonance*, Nature, **242**, 5394, 190-191 (1973).
12. Kanal, E., Shellock, F. G., Talagala, L., *Safety considerations in MR imaging*, Radiology, **176**, 3, 593-606 (1990).
13. Knuuti, J., Saraste, A., Kallio, M., Minn, H., *Is cardiac magnetic resonance imaging causing DNA damage?*, European Heart Journal, **34**, 30, 2337-2339 (2013).
14. Szerencsi, A., Kubinyi, G., Valiczko, E., Juhasz, P., Rudas, G., Mester, A., Janossy, G., Bakos, J., Thuroczy, G., *DNA integrity of human leukocytes after magnetic resonance imaging*, International Journal of Radiation Biology, **89**, 10, 870-876 (2013).
15. Budinger, T. F., *Nuclear magnetic-resonance (NMR) in vivo studies - known thresholds for health-effects*, Journal of Computer Assisted Tomography, **5**, 6, 800-811 (1981).

16. Le-Bihan, D., *Diffusion and Perfusion Magnetic Resonance Imaging: Applications to Funtioncal MRI,* Raven Press, New York, USA (1995).
17. Buxton, R. B., *Introduction to Functional Magnetic Resonance Imaging: Princples & Techniques,* Cambridge University Press, Cambridge, England (2002).
18. Zeeman, P., *The Effect of Magnetisation on the Nature of Light Emitted by a Substance*, Nature, **55**, 1424, 347 (1897).
19. Lerner, R. G., Trigg, G. L., *Encyclopaedia of Physics,* 2nd ed., VCH, New York (1991).
20. Glover, P., Mansfield, P., *Limits to magnetic resonance microscopy*, Reports on Progress in Physics, **65**, 10, 1489-1511 (2002).
21. Bloch, F., *Nuclear Induction*, Physical Review, **70**, 7-8, 460-474 (1946).
22. Geraldes, C. F. G. C., Laurent, S., *Classification and basic properties of contrast agents for magnetic resonance imaging*, Contrast Media & Molecular Imaging, **4**, 1, 1-23 (2009).
23. Marckmann, P., Skov, L., Rossen, K., Dupont, A., Damholt, M. B., Heaf, J. G., Thomsen, H. S., *Nephrogenic systemic fibrosis: Suspected causative role of gadodiamide used for contrast-enhanced magnetic resonance imaging*, Journal of the American Society of Nephrology, **17**, 9, 2359-2362 (2006).
24. Bennett, C. L., Qureshi, Z. P., Sartor, A. O., Norris, L. B., Murday, A., Xirasagar, S., Thomsen, H. S., *Gadolinium-induced nephrogenic systemic fibrosis: the rise and fall of an iatrogenic disease*, Clincal Kidney Journal, **5**, 1, 82-88 (2012).
25. Silva, A. C., Lee, J. H., Aoki, L., Koretsky, A. R., *Manganese-enhanced magnetic resonance imaging (MEMRI): methodological and practical considerations*, Nmr in Biomedicine, **17**, 8, 532-543 (2004).
26. Lin, Y.-J., Koretsky, A. P., *Manganese ion enhances T1-weighted MRI during brain activation: An approach to direct imaging of brain function*, Magnetic Resonance in Medicine, **38**, 3, 378-388 (1997).
27. Wiener, E. C., Brechbiel, M. W., Brothers, H., Magin, R. L., Gansow, O. A., Tomalia, D. A., Lauterbur, P. C., *Dendrimer-based metal-chelates - a new class of magnetic-resonance-imaging contrast agents*, Magnetic Resonance in Medicine, **31**, 1, 1-8 (1994).
28. Caravan, P., Ellison, J. J., McMurry, T. J., Lauffer, R. B., *Gadolinium(III) chelates as MRI contrast agents: Structure, dynamics, and applications*, Chemical Reviews, **99**, 9, 2293-2352 (1999).
29. Reynolds, C. H., Annan, N., Beshah, K., Huber, J. H., Shaber, S. H., Lenkinski, R. E., Wortman, J. A., *Gadolinium-loaded nanoparticles: New contrast agents for magnetic*

resonance imaging, Journal of the American Chemical Society, **122**, 37, 8940-8945 (2000).

30. Herman, D. A. J., Ferguson, P., Cheong, S., Hermans, I. F., Ruck, B. J., Allan, K. M., Prabakar, S., Spencer, J. L., Lendrum, C. D., Tilley, R. D., *Hot-injection synthesis of iron/iron oxide core/shell nanoparticles for T-2 contrast enhancement in magnetic resonance imaging*, Chemical Communications, **47**, 32, 9221-9223 (2011).
31. Pan, D. P. J., Schmieder, A. H., Wickline, S. A., Lanza, G. M., *Manganese-based MRI contrast agents: past, present, and future*, Tetrahedron, **67**, 44, 8431-8444 (2011).
32. Xiao, L., Li, J., Brougham, D. F., Fox, E. K., Feliu, N., Bushmelev, A., Schmidt, A., Mertens, N., Kiessling, F., Valldor, M., Fadeel, B., Mathur, S., *Water-Soluble Superparamagnetic Magnetite Nanoparticles with Biocompatible Coating for Enhanced Magnetic Resonance Imaging*, Acs Nano, **5**, 8, 6315-6324 (2011).
33. Loving, G. S., Mukherjee, S., Caravan, P., *Redox-Activated Manganese-Based MR Contrast Agent*, Journal of the American Chemical Society, **135**, 12, 4620-4623 (2013).
34. Coenen, H. H., *Radiopharmazeutische Chemie: Grundlagen zur in vivo Untersuchung molekularer Vorgänge mit PET*, Der Nuklearmediziner, **17**, 203-214 (1994).
35. Ache, H. J., *Chemistry of positron and of positronium*, Angewandte Chemie - International Edition, **11**, 3, 179-199 (1972).
36. Karshenboim, S. G., *Precision study of positronium: Testing bound state QED theory*, International Journal of Modern Physics A, **19**, 23, 3879-3896 (2004).
37. Vallabhajosula, S., *Molecular Imaging: Radiopharmaceuticals for PET and SPECT,* Springer-Verlag Berlin, Germany (2009).
38. Henkin, R. E., Bova, D., Dillehay, G. L., Karesh, S. M., Halama, J. R., Wagner, R. H., *Nuclear Medicine: 2-Volume Set, 2nd edition,* Mosby (imprint), Maryland Heights, USA, (2006).
39. Maus, J., *Development of a Parallel Computing Optimized Head Movement Correction Method in Positron Emission Tomography*, M.Sc. thesis, University of Applied Sciences Dresden and Research Center Dresden-Rossendorf, Germany (2003).
40. Jansen, F. P., Vanderheyden, J. L., *The future of SPECT in a time of PET*, Nuclear Medicine and Biology, **34**, 7, 733-735 (2007).
41. Watabe, H., Ikoma, Y., Kimura, Y., Naganawa, M., Shidahara, M., *PET kinetic analysis - compartmental model*, Annals of Nuclear Medicine, **20**, 9, 583-588 (2006).

42. Bailey, D. L., Willowson, K. P., *An Evidence-Based Review of Quantitative SPECT Imaging and Potential Clinical Applications*, Journal of Nuclear Medicine, **54**, 1, 83-89 (2013).
43. Townsend, D. W., Beyer, T., Kinahan, P., Meltzer, C. C., Brun, T., Nutt, R., *The SMART scanner: A combined PET/CT tomograph for clinical oncology*, Radiology, **209P**, 169-170 (1998).
44. Bailey, D. L., Barthel, H., Beuthin-Baumann, B., Beyer, T., Bisdas, S., Boellaard, R., Czernin, J., Drzezga, A., Ernemann, U., Franzius, C., Guckel, B., Handgretinger, R., Hartenbach, M., Hellwig, D., Nadel, H., Nekolla, S. G., Pfluger, T., Pichler, B. J., Quick, H. H., Sabri, O., Sattler, B., Schafer, J., Schick, F., Siegel, B. A., Schlemmer, H. P., Schwenzer, N. F., van den Hoff, J., Veit-Haibach, P., Wehrl, H. F., *Combined PET/MR: Where Are We Now? Summary Report of the Second International Workshop on PET/MR Imaging April 8-12, 2013, Tubingen, Germany*, Molecular Imaging and Biology, **16**, 3, 295-310 (2014).
45. Schmand, M., Burbar, Z., Corbeil, J., Zhang, N., Michael, C., Byars, L., Eriksson, L., Grazioso, R., Martin, M., Moor, A., Camp, J., Matschl, V., Ladebeck, R., Renz, W., Fischer, H., Jattke, K., Schnur, G., Rietsch, N., Bendriem, B., Heiss, W.-D., *BrainPET: First human tomograph for simultaneous (functional) PET and MR imaging*, Journal of Nuclear Medicine Meeting Abstracts, **48**, MeetingAbstracts_2, 45P- (2007).
46. Zaidi, H., Ojha, N., Morich, M., Griesmer, J., Hu, Z., Maniawski, P., Ratib, O., Izquierdo-Garcia, D., Fayad, Z. A., Shao, L., *Design and performance evaluation of a whole-body Ingenuity TF PET-MRI system*, Physics in Medicine and Biology, **56**, 10, 3091-3106 (2011).
47. Wehrl, H. F., Judenhofer, M. S., Wiehr, S., Pichler, B. J., *Pre-clinical PET/MR: technological advances and new perspectives in biomedical research*, European Journal of Nuclear Medicine and Molecular Imaging, **36**, 56-68 (2009).
48. Kolb, A., Wehrl, H. F., Hofmann, M., Judenhofer, M. S., Eriksson, L., Ladebeck, R., Lichy, M. P., Byars, L., Michel, C., Schlemmer, H. P., Schmand, M., Claussen, C. D., Sossi, V., Pichler, B. J., *Technical performance evaluation of a human brain PET/MRI system*, European Radiology, **22**, 8, 1776-1788 (2012).
49. Singh, H., *Photodetectors and Fiber Optics,* 1st ed., Academic Press, Waltham, USA (2001).
50. Herzog, H., Langen, K. J., Weirich, C., Kops, E. R., Kaffanke, J., Tellmann, L., Scheins, J., Neuner, I., Stoffels, G., Fischer, K., Caldeira, L., Coenen, H. H., Shah, N. J., *High resolution BrainPET combined with simultaneous MRI*, Nuklearmedizin-Nuclear Medicine, **50**, 2, 74-82 (2011).

51. Jadvar, H., Colletti, P. M., *Competitive advantage of PET/MRI*, European Journal of Radiology, **83**, 1, 84-94 (2014).
52. de Rosales, R. T. M., *Potential clinical applications of bimodal PET-MRI or SPECT-MRI agents*, Journal of Labelled Compounds & Radiopharmaceuticals, **57**, 4, 298-303 (2014).
53. Merbach, A., Helm, L, Tóth, É., *The Chemistry of Contrast Agents in Medical Magnetic Resonance Imaging, 2nd edition,* Wiley, Chichester, UK (2013).
54. Michalke, B., Halbach, S., Nischwitz, V., *Speciation and toxicological relevance of manganese in humans*, Journal of Environmental Monitoring, **9**, 7, 650-656 (2007).
55. Silva, A. C., Bock, N. A., *Manganese-enhanced MRI: An exceptional tool in translational neuroimaging*, Schizophrenia Bulletin, **34**, 4, 595-604 (2008).
56. Boretius, S., Frahm, J., *Manganese-Enhanced Magnetic Resonance Imaging*, in: Schroder, L. and Faber, C. (Eds.), *In vivo* NMR Imaging: Methods and Protocols. Humana Press Inc, Totowa, USA, pp. 531-568 (2011).
57. Massaad, C. A., Pautler, R. G., *Manganese-Enhanced Magnetic Resonance Imaging (MEMRI),* Humana Press Inc, Totowa, USA, (2011).
58. Cacace, A. T., Brozoski, T., Berkowitz, B., Bauer, C., Odintsov, B., Bergkvist, M., Castracane, J., Zhang, J. S., Holt, A. G., *Manganese enhanced magnetic resonance imaging (MEMRI): A powerful new imaging method to study tinnitus*, Hearing Research, **311**, 49-62 (2014).
59. Kueny-Stotz, M., Garofalo, A., Felder-Flesch, D., *Manganese-Enhanced MRI Contrast Agents: From Small Chelates to Nanosized Hybrids*, European Journal of Inorganic Chemistry, 12, 1987-2005 (2012).
60. Evaluated Nuclear Structure Data File (ENSDF), Available at: http://www.nndc.bnl.gov/ensdf, IAEA-NDS, (last accessed: 29/9/2014).
61. Lederer, C. M., Shirley, V. S., *Table of Isotopes,* 7th, John Wiley & Sons Inc., New York, USA (1978).
62. Klein, A. T. J., Rosch, F., Qaim, S. M., *Investigation of Cr-50(d,n)Mn-51 and Cr-nat(p,x)Mn-51 processes with respect to the production of the positron emitter Mn-51*, Radiochimica Acta, **88**, 5, 253-264 (2000).
63. Wing, J., Huizenga, J. R., *(p,n) cross sections of V51, Cr52, Cu63, Cu65, Ag107, Ag109, Cd111, and La139 from 5 to 10.5 MeV*, Physical Review, **128**, 1, 280-290 (1962).
64. West, H. I., Lanier, R. G., Mustafa, M. G., *(Cr-52(p,n)Mn-g,m)-Mn-52 and (Cr-52(d,2n)Mn-g,m)-Mn-52 excitation-functions*, Physical Review C, **35**, 6, 2067-2076 (1987).

65. Buchholz, M., Spahn, I., Scholten, B., Coenen, H. H., *Cross-section measurements for the formation of manganese-52 and its isolation with a non-hazardous eluent*, Radiochimica Acta, **101**, 491-499 (2013).
66. Von Halban, H., Kowarski, L., *Capture cross-sections for 220 Kev. Neutrons*, Nature, **142**, 392-393 (1938).
67. Levkovskij, V. N., *Activation Cross Sections for the Nuclides of Medium Mass Region (A=40-100) with Medium Energy (E=10-50 MeV) Protons and Alpha Particles (Experiment and Systematics),* Inter-Vesi, Moscow, Russia (1991).
68. Skakun, E. A., Batii, V. G., Rakivnenko, Y. N., Rastrepin, O. A., *Investigation of Cr-52(pn)Mn-52m,g and Cr-54(pn)Mn-54 reaction cross sections in the 5-9 MeV energy range*, Izvestiya Akademii Nauk Sssr Seriya Fizicheskaya, **50**, 10, 2043-2045 (1986).
69. Muminov, V. A., Mukhammedov, S., Vasidov, A., *Possibilities of proton-activation analysis for determining the content of elements from short-lived radionuclides*, Soviet Atomic Energy, **49**, 2, 540-544 (1980).
70. Barrandon, J. N., Debrun, J. L., Kohn, A., Spear, R. H., *Study of level of Ti, V, Cr, Fe, Ni, Cu and Zn by activation with protons whose energy is limited to 20 MeV*, Nuclear Instruments & Methods, **127**, 2, 269-278 (1975).
71. Topping, G. J., Schaffer, P., Hoehr, C., Ruth, T. J., Sossi, V., *Manganese-52 positron emission tomography tracer characterization and initial results in phantoms and in vivo*, Medical Physics, **40**, 4, (2013).
72. Denzler, F.-O., *Produktion und radiochemische Abtrennung von ^{147}Gd zur Markierung und in vivo SPET-Evaluation von Magnetopharmaka*, PhD Thesis, Universität zu Köln (1997).
73. Archenti, A., Ozafran, M. J., Nassiff, S. J., *(α,xn) reactions on natural samarium*, Journal of Radioanalysis and Nuclear Chemistry, **132**, 139-151 (1989).
74. West, H. I., Lanier, R. G., Mustafa, M. G., Nuckolls, R. N., Frehaut, J., Adam, A., Philis, C. A., *Proton and deuteron excitation functions for Eu-151 and Eu-153*, Rept: Brookhaven National Laboratory Reports, No.42382, 87-96 (1989).
75. Denzler, F.-O., Rösch, F., Qaim, S. M., *Excitation functions of alpha-and ^{3}He-particle induced nuclear reactions on highly enriched ^{144}Sm and ^{147}Sm: comparative evaluation of production routes for ^{147}Gd*, Radiochimica Acta, **69**, 4, 209-213 (1995).
76. Takács, S., Tárkányi, F., Hermanne, A., Adam-Rebeles, R., Takács, M. P., *Excitation functions for the formation of longer lived isotopes by deuteron irradiation of europium*, Nuclear Instruments & Methods in Physics Research Section B-Beam Interactions with Materials and Atoms, **310**, 54-66 (2013).

77. Lebedev, N. A., Novgorordov, A. F., Slovak, J., Khalkin, V. A., Ekhu, L., *^{146,147,149}Gd preparations prepared from europium irradiated by 100 MeV protons*, Radioisotopy, **29**, 240-247 (1988).

78. Denzler, F.-O., Lebedev, N. A., Novgorodov, A. F., Rösch, F., Qaim, S. M., *Production and radiochemical separation of ^{147}Gd*, Applied Radiation and Isotopes, **48**, 3, 319-326 (1997).

79. Nayak, D., Lahiri, S., Ramaswami, A., Manohor, S. B., *Separation of no-carrier added Gd-147,Gd-149 and Eu-147 produced in 70 MeV B-11 irradiated praseodymium foil target*, Radiochimica Acta, **87**, 3-4, 93-96 (1999).

80. Loveland, W., Morrissey, D. J., Seaborg, G. T., *Modern Nuclear Chemistry,* John Wiley & Sons Inc., New Jersey, USA (2006).

81. Mason, T. E., Abernathy, D., Anderson, I., Ankner, J., Egami, T., Ehlers, G., Ekkebus, A., Granroth, G., Hagen, M., Herwig, K., Hodges, J., Hoffmann, C., Horak, C., Horton, L., Klose, F., Larese, J., Mesecar, A., Myles, D., Neuefeind, J., Ohl, M., Tulk, C., Wang, X. L., Zhao, J., *The Spallation Neutron Source in Oak Ridge: A powerful tool for materials research*, Physica B-Condensed Matter, **385-86**, 955-960 (2006).

82. Anonymous, *ISIS, The spallation neutron source at RAL* Journal of the Institution of Electronic and Radio Engineers, **55**, 11-1, 371-371 (1985).

83. Wideröe, R., *Über ein neues Prinzip zur Herstellung hoher Spannungen*, Archiv für Elektrotechnik, **21**, 4, 387-406 (1928).

84. Thomas, L. H., *The paths of ions in the cyclotron I. Orbits in the magnetic field*, Physical Review, **54**, 8, 580-588 (1938).

85. Thomas, L. H., *The Paths of Ions in the Cyclotron II. Paths in the Combined Electric and Magnetic Fields*, Physical Review, **54**, 8, 588-598 (1938).

86. Blaser, J. P., *SIN ring cyclotron project*, Nuclear Engineering International, **15**, 168, 428-& (1970).

87. Brianti, G., *The large hadron collider (LHC) in the LEP tunnel,* C E R N, Geneva (1989).

88. Weinreich.R, Schult, O., Stöcklin, G., *Production of I-123 via I-127(d,6n) Xe-123(β+,EC)I-123 process*, International Journal of Applied Radiation and Isotopes, **25**, 11-1, 535-543 (1974).

89. Qaim, S. M., Stöcklin, G., Weinreich, R., *Excitation functions for formation of neutron deficient isotopes of bromine and krypton via high-energy deuteron induced reactions on bromine - production of Br-77, Br-76 and Kr-79*, International Journal of Applied Radiation and Isotopes, **28**, 12, 947-953 (1977).

90. Weiß, J., *Ionenchromatographie,* 3rd edition, Wiley-VCH, Weinheim, Germany (2001).

91. Helfferich, F., *Ion Exchange,* McGraw-Hill Book Company, New York, USA (1962).
92. Braun T., Ghersini, G., *Journal of Chromatography Library - Volume 2: Extraction Chromatography,* Elsvier Scientific Publishing Company, Amsterdam, Netherlands (1975).
93. Dietz, M. L., Horwitz, E. P., *Applications of extraction chromatography in the development of radionuclide generator systems for nuclear medicine*, Industrial & Engineering Chemistry Research, **39**, 9, 3181-3188 (2000).
94. Ojala, F., Max-Hansen, M., Kifle, D., Borg, N., Nilsson, B., *Modelling and optimisation of preparative chromatographic purification of europium*, Journal of Chromatography A, **1220**, 21-25 (2012).
95. Faris, J. P., Warton, J. W., *Anion exchange resin separation of rare earths, yttrium, and scandium in nitric acid-methanol mixtures*, Analytical Chemistry, **34**, 9, 1077-1080 (1962).
96. Powell, J. E., Burkholder, H. R., *Augmenting separation of gadolinium and europium and europium and samarium mixtures in ion exchange elutions with EDTA*, Journal of Chromatography, **29**, 1, 210-217 (1967).
97. Herrmann, E., *A contribution to separation of rare earths by extraction chromatography with di(2-ethylhexyl)phosphoric acid (HDEHP) .I. silica gel as support material for stationary phase*, Journal of Chromatography, **38**, 4, 498-& (1968).
98. Kobisk, E. H., Grisham, W. B., *Application of reduction-distillation method for preparing high-purity rare-earth isotope metals*, Materials Research Bulletin, **4**, 9, 651-662 (1969).
99. Robards, K., Clarke, S., Patsalides, E., *Advances in the analytical chromatography of the lanthanides - a review*, Analyst, **113**, 12, 1757-1779 (1988).
100. Preston, J. S., duPreez, A. C., *The separation of europium from a middle rare earth concentrate by combined chemical reduction, precipitation and solvent-extraction methods*, Journal of Chemical Technology and Biotechnology, **65**, 1, 93-101 (1996).
101. Jelinek, L., Wei, Y. Z., Arai, T., Kumagai, M., *Selective Eu(III) electro-reduction and subsequent separation of Eu(II) from rare earths(III) via HDEHP impregnated resin*, Solvent Extraction and Ion Exchange, **25**, 4, 503-513 (2007).
102. Peppard, D. F., Horwitz, E. P., Mason, G. W., *Comparative liquid-liquid extraction behaviour of europium (II) and europium (III)*, Journal of Inorganic and Nuclear Chemistry, **24**, 4, 429-439 (1962).
103. Sochacka, R. J., Siekierski, S., *Reversed-phase partition chromatography with di-(2ethylhexyl)orthophosphoric acid as stationary phase .I. separation of rare earths*, Journal of Chromatography, **16**, 2, 376-384 (1964).

104. Campbell, D. O., *Rapid rare-earth separation by pressurized ion-exchange chromatography*, Journal of Inorganic & Nuclear Chemistry, **35**, 11, 3911-3919 (1973).

105. Qaim, S. M., Ollig, H., Blessing, G., *Separation of lanthanides by preparative high-pressure liquid-chromatography*, Radiochimica Acta, **26**, 1, 59-62 (1979).

106. Johnsen, A. M., Soderquist, C. Z., McNamara, B. K., Fisher, D. R., *A non-aqueous reduction process for purifying ^{153}Gd produced in natural europium targets*, Applied Radiation and Isotopes, **82**, 0, 158-165 (2013).

107. Horwitz, E. P., McAlister, D. R., Bond, A. H., Barrans, R. E., *Novel extraction of chromatographic resins based on tetraalkyldiglycolamides: Characterization and potential applications*, Solvent Extraction and Ion Exchange, **23**, 3, 319-344 (2005).

108. Malan, H. P., Munzel, H., *Rapid radiochemical separations .2. separation of europium from other lanthanides*, Radiochimica Acta, **5**, 1, 20-23 (1966).

109. H. B. Herman, Rairden, J. R., *Encyclopedia of electrochemistry of the elements,* 35-36, Marcel Dekker, INC., New York, USA (1976).

110. Taniguchi, N., *On he Basic Concept of 'Nano-Technology'*, Proc. Intl. Conf. Prod. Eng. Tokyo, Part II, (1974).

111. Drexler, K. E., *Engines of Creation: The Coming Era of Nanotechnology,* Anchor Books, New York (1986).

112. Feynman, R. P., *There´s plenty of room at the bottom [data storage]*, Journal of Microelectromechanical Systems, **1**, 1, 60-66 (1992).

113. National Nanotechnology Initiative, Available at: www.nano.gov, (last accessed: 10.10.2014).

114. Cao, G., *Nanostructures & Nanomaterials: Synthesis, Properties & Applications,* Imperial College Press, London, England (2004).

115. Ostwald, W., *On the assumed isomerism of red and yellow mercury oxide and the surface-tension of solid bodies*, Zeitschrift Für Physikalische Chemie - Stöchiometrie Und Verwandtschaftslehre, **34**, 4, 495-503 (1900).

116. Lamer, V. K., Dinegar, R. H., *Theory, production and mechanism of formation of monodispersed hydrosols*, Journal of the American Chemical Society, **72**, 11, 4847-4854 (1950).

117. Murray, C. B., Kagan, C. R., Bawendi, M. G., *Synthesis and characterization of monodisperse nanocrystals and close-packed nanocrystal assemblies*, Annual Review of Materials Science, **30**, 545-610 (2000).

118. Ozin, G. A., André, A. C., *Nanochemistry: A chemical approach to nanomaterials,* The Royal Society of Chemistry, Cambridge, England (2005).

119. Wagner, J., *Particle-sizing by dynamic light scattering*, Chemie Ingenieur Technik, **58**, 7, 578-583 (1986).

120. Rösch, F., Qaim, S. M., Stöcklin, G., *Nuclear data relevant to the production of the positron emitting radioisotope Y-86 via the Sr-86(p,n)- and Rb-nat(He-3,xn)-processes*, Radiochimica Acta, **61**, 1, 1-8 (1993).

121. Tárkányi, F. T., Takács, S., Gul, K., Hermanne, A., Mustafa, M. G., Nortier, M., Obložinský, P., Qaim, S. M., Scholten, B., Shubin, Yu, N., Zhuang, Y., *Monitor reactions, in charged particle cross section database for medical radioisotope production, IAEA-TECDOC-1211*. International Atomic Energy Agency, Vienna, pp. 49-152 (2001).

122. Livingston, M. S., Bethe, H. A., *Nuclear physics - C. nuclear dynamics, experimental*, Reviews of Modern Physics, **9**, 3, 0245-0390 (1937).

123. Williamson, C. F., Boujot, J.-B., Picard, J., *Tables of range and stopping power of chemical elements for charged particles of energy 0.05 to 500 MeV,* Department de Physique Nucleaire Rapport CEA-R 3042, (1966).

124. Piel, H., Qaim, S. M., Stöcklin, G., *Excitation-functions of (p,xn)-reactions on Ni-nat and highly enriched Ni-62 - possibility of production of medically important radioisotope Cu-62 at a small cyclotron*, Radiochimica Acta, **57**, 1, 1-5 (1992).

125. *IEEE Standard American National Standard for Calibration and Use of Germanium Spectrometers for the Measurement of Gamma-Ray Emission Rates of Radionuclides,* IEEE, New York, USA (1999).

126. Vanasschen, C., Bouslimani, N., Thonon, D., Desreux, J. F., *Gadolinium DOTA Chelates Featuring Alkyne Groups Directly Grafted on the Tetraaza Macrocyclic Ring: Synthesis, Relaxation Properties, "Click" Reaction, and High-Relaxivity Micelles*, Inorganic Chemistry, **50**, 18, 8946-8958 (2011).

127. Huclier-Markai, S., Alliot, C., Rousseau, J., Chouin, N., Fani, M., Bouziotis, P., Maina, T., Cutler, C. S., Barbet, J., *Promising prospects of Sc-44m/Sc-44 as an in vivo generator: Biological evaluation and PET images*, Nuclear Medicine and Biology, **41**, 7, 631-631 (2014).

128. McRobbie, D. W., Moore, E. A., Graves, M. J., Prince, M. R., *MRI From Picture to Proton,* 2nd ed., Cambridge University Press, Cambridge (2006).

129. Buchholz, M., *Kernchemische Studien zur Produktion des Positronenstrahlers ^{52}Mn an einem Zyklotron*, diploma thesis, University of Cologne (2011).

130. Russell, H. T., *Isolation of carrier-free Mn-54 and I-125 from cyclotron targets*, Nuclear Science and Engineering, **7**, 4, 323-324 (1960).

131. Graddon, D. P., Mockler, G. M., *Some 5- + 6-coordinate base adducts of bis(acetylacetonato)-manganese)2)*, Australian Journal of Chemistry, **17**, 10, 1119-1127 (1964).

132. Bilecka, I., Djerdj, I., Niederberger, M., *One-minute synthesis of crystalline binary and ternary metal oxide nanoparticles*, Chemical Communications, 7, 886-888 (2008).

133. Park, J. Y., Choi, E. S., Baek, M. J., Lee, G. H., Woo, S., Chang, Y., *Water-Soluble Ultra Small Paramagnetic or Superparamagnetic Metal Oxide Nanoparticles for Molecular MR Imaging*, European Journal of Inorganic Chemistry, 17, 2477-2481 (2009).

134. Na, H. B., Lee, J. H., An, K. J., Park, Y. I., Park, M., Lee, I. S., Nam, D. H., Kim, S. T., Kim, S. H., Kim, S. W., Lim, K. H., Kim, K. S., Kim, S. O., Hyeon, T., *Development of a T-1 contrast agent for magnetic resonance imaging using MnO nanoparticles*, Angewandte Chemie-International Edition, **46**, 28, 5397-5401 (2007).

135. Baek, M. J., Park, J. Y., Xu, W. L., Kattel, K., Kim, H. G., Lee, E. J., Patel, A. K., Lee, J. J., Chang, Y. M., Kim, T. J., Bae, J. E., Chae, K. S., Lee, G. H., *Water-Soluble MnO Nanocolloid for a Molecular T-1 MR Imaging: A Facile One-Pot Synthesis, In vivo T-1 MR Images, and Account for Relaxivities*, Acs Applied Materials & Interfaces, **2**, 10, 2949-2955 (2010).

136. Nichols, A. L., *A study of the chemical effects of the electron capture decay process by means of Mössbauer Spectroscopy*, University of Leeds, Leeds, United Kingdom (1972).

137. Rosman, K. J. R., Taylor, P. D. P., *Isotopic compositions of the elements 1997*, Pure and Applied Chemistry, **70**, 1, 217-235 (1998).

138. Koning, A. J., Rochman, D., *Modern Nuclear Data Evaluation With The TALYS Code System*, Nuclear Data Sheets, **113**, 12, 2841-2934 (2012).

139. TENDL-2013: TALYS-based evaluated nuclear data library, Available at: www.talys.eu/tendl-2013.html (last accessed: 01/21/2014).

140. Koning, A. J., Hilaire, S., Duijvestijn, M. C., *TALYS-1.0,* E D P Sciences, Cedex A (2008).

141. Bailey, D. L., Willowson, K. P., *An evidence-based review of quantitative SPECT imaging and potential clinical applications*, J. Nucl. Med., **54**, 83-89 (2013).

142. Experimental Nuclear Reaction Data (EXFOR), Available at: http://www.nndc.bnl.gov/exfor/exfor00.htm, IAEA-NDS, (last accessed: 11/27/2013).

143. Cacheris, W. P., Nickle, S. K., Sherry, A. D., *Thermodynamic study of lanthanide complexes of 1,4,7-triazacyclononane-N,N',N''-triacetic acid and 1,4,7,10-*

tetraazacyclododecane-N,N',N'',N'''-tetraacetic acid, Inorganic Chemistry, **26**, 6, 958-960 (1987).

144. Heilmann, M., Kiessling, F., Enderlin, M., Schad, L. R., *Determination of pharmacokinetic parameters in DCE MRI - Consequence of nonlinearity between contrast agent concentration and signal intensity*, Investigative Radiology, **41**, 6, 536-543 (2006).
145. Fessler, A., Alfassi, Z. B., Qaim, S. M., *Excitation function of ^{3}He-particle induced nuclear reactions on natural chromium: possibilities of production of ^{52}Fe, ^{53}Fe and ^{52}Mn for medical use*, Radiochimica Acta, **65**, 207-213 (1994).
146. Dmitriev, P. P., *Systematics of nuclear reaction yields for thick target at 22 MeV proton energy*, Vop. At. Nauki i Tekhn., Ser. Yadernye Konstanty, **2**, 57 (1983).
147. Abe, K., Iizuka, A., Hasegawa, A., Morozumi, S., *Induced radioactivity of component materials by 16-MeV protons and 30-MeV alpha-particles*, Journal of Nuclear Materials, **123**, 1-3, 972-976 (1984).
148. Klein, A. T. J., Rosch, F., Coenen, H. H., Qaim, S. M., *Production of the positron emitter Mn-51 via the Cr-50(d, n) reaction: targetry and separation of no-carrier-added radiomanganese*, Radiochimica Acta, **90**, 3, 167-177 (2002).
149. Kukula, F., Mudrova, B., Krivanek, M., *Use of thenoyltrifluoroacetone for determination of manganese by activation analysis*, Talanta, **14**, 2, 233-237 (1967).
150. Lahiri, S., Nayak, D., Korschinek, G., *Separation of no-carrier-added Mn-52 from bulk chromium: A simulation study for accelerator mass spectrometry measurement of Mn-53*, Analytical Chemistry, **78**, 21, 7517-7521 (2006).
151. Wilkinson, W. D., *Uranium Metallurgy, 1st Ed.,* Interscience Publishers, New York (1962).
152. Mornet, S., Vasseur, S., Grasset, F., Duguet, E., *Magnetic nanoparticle design for medical diagnosis and therapy*, Journal of Materials Chemistry, **14**, 14, 2161-2175 (2004).
153. Katz, E., Willner, I., *Integrated nanoparticle-biomolecule hybrid systems: Synthesis, properties, and applications*, Angewandte Chemie - International Edition, **43**, 45, 6042-6108 (2004).
154. Bilecka, I., Niederberger, M., *Microwave chemistry for inorganic nanomaterials synthesis*, Nanoscale, **2**, 8, 1358-1374 (2010).
155. Patzke, G. R., Zhou, Y., Kontic, R., Conrad, F., *Oxide Nanomaterials: Synthetic Developments, Mechanistic Studies, and Technological Innovations*, Angewandte Chemie-International Edition, **50**, 4, 826-859 (2011).

156. Si, H. L., Wang, H. Z., Shen, H. B., Zhou, C. H., Li, S., Lou, S. Y., Xu, W. W., Du, Z. L., Li, L. S., *Controlled synthesis of monodisperse manganese oxide nanocrystals*, Crystengcomm, **11**, 6, 1128-1132 (2009).

157. Mier, W., Babich, J., Haberkorn, U., *Is nano too big?*, European Journal of Nuclear Medicine and Molecular Imaging, **41**, 1, 4-6 (2014).

158. Otuka, N., Dupont, E., Semkova, V., Pritychenko, B., Blokhin, A. I., Aikawa, M., Babykina, S., Bossant, M., Chen, G., Dunaeva, S., Forrest, R. A., Fukahori, T., Furutachi, N., Ganesan, S., Ge, Z., Gritzay, O. O., Herman, M., Hlavač, S., Katō, K., Lalremruata, B., Lee, Y. O., Makinaga, A., Matsumoto, K., Mikhaylyukova, M., Pikulina, G., Pronyaev, V. G., Saxena, A., Schwerer, O., Simakov, S. P., Soppera, N., Suzuki, R., Takács, S., Tao, X., Taova, S., Tárkányi, F., Varlamov, V. V., Wang, J., Yang, S. C., Zerkin, V., Zhuang, Y., *Towards a More Complete and Accurate Experimental Nuclear Reaction Data Library (EXFOR): International Collaboration Between Nuclear Reaction Data Centres (NRDC)*, Nuclear Data Sheets, **120**, 272-276 (2014).

159. Holbrook, D. J., Washington, M. E., Leake, H. B., Brubaker, P. E., *Studies on the Evaluation of the Toxicity of various Salts of Lead, Manganese, Platinum, and Palladium*, Environmental Health Perspectives, **10**, 95-101 (1975).

160. Lewis, R. J., Sweet, D. V., *Registry of Toxic Effects of Chemical Substances,* Department of Health and Human Services, Public Health Service, Centers for Disease Control, National Institute for Occupational Safety and Health, Cincinnati, USA (1984).

Acknowledgements

My first and foremost gratitude for the support and guidance of my thesis belongs to my doctorate supervisor Prof. Dr. H. H. Coenen. In addition, I would like to express my thanks to him for the interesting topic of my work, his continuous scientific input and for the provision of the excellent working conditions found at the INM-5.

I would also like to take the opportunity to express my thanks to Dr. I. Spahn for the extensive discussions about my topic, his direct supervision of my thesis and constant support

Furthermore, I would like to thank Dr. B. Scholten for his support in technical questions and sharing his deep knowledge of γ-spectroscopy.

In addition, I thank Prof. Dr. S. M. Qaim for his scientific and linguistic help in the publications I have been involved in.

I am indebted to my valued colleges of the radionuclide development group Dr. S. Kuhn, Dr. K. Breunig and Mr. T. Wels for the long discussions, brainstorming about our common problems and the good collaboration over the years.

I sincerely thank my colleagues M. Brandt and Dr. C. Vanaschen for their help with the Gd-DOTA complex synthesis and stability tests. I also thank the HBS donors M. Brandt, Dr. A. Mainusch, D. Modemann and Dr. O. Petina. In addition, I thank Mrs. A. Schulze for the separation and handling of the blood serum.

Mr. P. Lohmann I owe my thanks for the execution of the *in vivo* MR as well *as the ex vivo* autoradiographic measurements of the rat brains used in this work. Prof. Dr. Langen I would like to thank for the opportunity to use the MR and autoradiographic facilities of the INM-4.

I am also grateful for the introduction to the practical aspects of TEM measurements by Dr. J. Buitenhuis and his assistance with the captured TEM images. Furthermore, I would like to express thanks to Dr. J. Dornseiffer and Mr. J. Borchardt for their support with my DLS measurements.

My warm thanks also go to the technical staff of the JULIC of IKP-4 and the BC1710 of INM-5 for their long working hours and their steady support with my irradiations. Concerning the radiation protection and the occupational safety work I thank Mr. S. Spellerberg, Mr. O. Felden, Mr. U. Otto and Mr. F. Mergner for their meaningful work.

Acknowledgements

My gratitude also belongs to the technical staff of the glass blower workshop of the ZEA led by Mr. A. Schwaitzer for their great work realizing my ideas of specialised glass equipment.

I thank Dr. E. Strub for the overnight support in the labs of the Nuclear Chemistry Department of the University Cologne.

Furthermore, I wish to give thanks to my sister Dr. A. Buchholz for her linguistic support of my PhD thesis.

I thank every colleague of the INM-4, INM-5 and IKP-4 who participated in my three year long voyage named PhD-thesis for the good collaboration and work conditions.

Last, but absolutely not least I would like to express my gratitude to Dr. A. Mainusch, my parents and siblings for their continuous support throughout the rough parts of the last years.

Ich versichere, dass ich die von mir vorgelegte Dissertation selbständig angefertigt, die benutzten Quellen und Hilfsmittel vollständig angegeben und die Stellen der Arbeit - einschließlich Tabellen, Karten und Abbildungen -, die anderen Werken im Wortlaut oder dem Sinn nach entnommen sind, in jedem Einzelfall als Entlehnung kenntlich gemacht habe; dass diese Dissertation noch keiner anderen Fakultät oder Universität zur Prüfung vorgelegen hat; dass sie - abgesehen von unten angegeben Teilpublikationen - noch nicht veröffentlicht worden ist, sowie, dass ich eine solche Veröffentlichung vor Abschluss des Promotionsverfahrens nicht vornehmen werde. Die Bestimmungen der Promotionsordnung sind mir bekannt. Die von mir vorgelegte Dissertation ist von Prof. Dr. H. H. Coenen betreut worden.

Jülich, im Februar 2015

Teilveroffentlichungen

Buchholz, M., Spahn, I., Scholten, B.,Coenen, H. H., Radiochimica Acta, **101**, 491 (2013).

Buchholz, M., Spahn, I.,Coenen, H. H., Applied Radiation and Isotopes, **91**, 8 (2014).

Jül-4387
Juni 2015
ISSN 0944-2952